Winter 2006

LINKING MULTIVARIATE OBSERVATIONS OF THE LAND SURFACE TO VEGETATION PROPERTIES AND ECOSYSTEM PROCESSES

Stephen C. Hagen
University of New Hampshire

LINKING MULTIVARIATE OBSERVATIONS OF THE LAND SURFACE TO VEGETATION PROPERTIES AND ECOSYSTEM PROCESSES

BY

STEPHEN C. HAGEN

BS, University of Virginia, 1997

MS, University of Virginia, 1999

DISSERTATION

Submitted to the University of New Hampshire

in Partial Fulfillment of

the Requirements for the Degree of

Doctor of Philosophy

in

Earth and Environmental Science

December, 2006

This dissertation has been examined and approved.

Stephen E Frolking

Dissertation Director, Stephen E. Frolking, Research Associate Professor of Earth Sciences and Earth, Oceans, and Space

John D. Aber

John D. Aber, Vice President for Research and Public Service and Professor of Natural Resources and Earth, Oceans, and Space

Bobby H. Braswell, Research Assistant Professor of Earth, Oceans, and Space

Ernst Linder

Ernst Linder, Professor of Mathematics and Statistics

Xiangming Xiao

Xiangming Xiao, Research Associate Professor of Earth, Oceans, and Space

14 Nov, 2006

Date

ACKNOWLEDGEMENTS

The research conducted herein was funded through the NASA Large Scale Biosphere Atmosphere Experiment in Amazonia (LBA; NNG05GE28A), NASA Interdisciplinary Sciences (IDS; NNG04GH75G), and US Department of Energy's Northeast Regional Center of the National Institute for Global Environmental Change (NIGEC). Permission for the use of published materials herein was granted by *Remote Sensing of Environment* and *Journal of Geophysical Research-Atmospheres*. Special thanks to Dr. Bobby H. Braswell and Dr. Steve Frolking for their time, consideration, guidance, and advice. Thanks also to Dr. John Aber, Dr. Xiangming Xiao, and Dr. Ernst Linder for their counsel; the Complex Systems Research Center and all those who make it function (Karen Bushold, Faith Sheridan, Gary DesJardins, Linda Tibbets, Bindy Camire, Jennifer Parsons, and others); and the Institute for the Study of Earth, Oceans, and Space for encouraging innovative research. Field research and support was provided by Lucas Fortini, Joanna Tucker, and Flavio Fendt. Advice and support from Dr. William Salas, Dr. Michael Keller, Dr. Mark Ducey, Dr. George Hurtt, Denise Blaha, Michael Palace, Dr. Evilene (Lopes) Bowley, Lorena Brewster, Steve Boles, Michael Routhier, and Andy Mosedale were indispensable. For everything that is really important, thanks most of all to my family: Margaret Hagen, Charles Hagen, Henry Hagen, Baby Hagen, and Shelley Girdner.

TABLE OF CONTENTS

LIST OF TABLES

LIST OF FIGURES

ABSTRACT

LINKING MULTIVARIATE OBSERVATIONS OF THE LAND SURFACE TO VEGETATION PROPERTIES AND ECOSYSTEM PROCESSES

by

Stephen C. Hagen

University of New Hampshire, December, 2006

Remotely sensed images from satellites and aircrafts, as well as regional networks and monitoring stations such as eddy flux towers, are collecting large volumes of multivariate data that contain information about the land surface and ecosystem processes. To derive from these systems information and knowledge relevant to how the Earth system functions and how it is changing, we need tools that to filter and mine the large data streams currently being acquired at different spatial and temporal scales. A challenge for Earth System Science lies in accurately identifying and portraying the relationships between the measurements at the sensor and quantity of interest (i.e. ecosystem process or land surface property).

In this document, topics in the modeling of multivariate data sets are explored in four independent studies. These studies use a range of process-based and statistical modeling techniques to relate remote observations to ecologically relevant attributes. Each study also includes an analysis of factors contributing to uncertainty. The first three studies

examine issues related to the remote sensing of land surface properties in the Brazilian Amazon, including the effect of phenology and seasonality on the monitoring of regenerating vegetation (Chapter 2), mapping large-scale human land cover change (Chapter 3), and coarse resolution sub-pixel unmixing of land cover types (Chapter 4). The fourth study proposes a broadly applicable technique for quantifying the statistical uncertainty involved in estimating gross ecosystem exchange from an eddy flux tower (Chapter 5).

CHAPTER 1

INTRODUCTION

Remotely sensed images from satellites and aircrafts, as well as regional networks and monitoring stations such as eddy flux towers, are collecting large volumes of multivariate data that contain information about the land surface and ecosystem processes. To derive from these systems information and knowledge relevant to how the Earth system functions and how it is changing, we need tools that to filter and mine the large data streams currently being acquired at different spatial and temporal scales.

Observation systems often measure proxies. For instance, expensive satellites are in orbit overhead not because the spectral radiance of the land surface as seen through a variable atmosphere is of particular interest, in itself. Instead, of interest to us is what we can derive from those raw measurements. For earth scientists, these derivatives include the presence or absence of a geological formation or vegetation type; a quantitative estimate of an ecosystem process like photosynthesis; or, with multiple images in time, the rate of change of a land surface property. The challenge lies in accurately identifying and portraying the relationships between the measurements at the sensor and quantity of interest (i.e. ecosystem process or land surface property).

The relation of indirect measurements to ecosystem attributes is most often accomplished with models. These models can be process-based or statistical. Process-based models rely on known physical, biological, chemical, or mechanical interactions occurring within a system. Statistical models are a mathematical framework consisting of a set of parameters, usually lacking an interpretable meaning, that are adjusted to best relate independent observations to dependent observations.

Whether one employs process-based or statistical models or a combination of the two to connect independent measurements to ecologically meaningful estimates, uncertainty will be a by-product of the modeling process and estimates of this uncertainty are valuable. Most statistical models, such as linear regression, have simple mathematical techniques for estimating uncertainty in parameters and predictions. Most process-based modeling techniques require more creative methods of estimating uncertainty, such as Monte Carlo techniques. A Bayesian modeling framework is useful for incorporating many different sources of uncertainty.

In this document, topics in the modeling of multivariate data sets are explored in four independent studies. These studies use a range of process-based and statistical modeling techniques to relate remote observations to ecologically relevant attributes. Each study also includes an analysis of factors contributing to uncertainty. The first three studies examine issues related to the remote sensing of land surface properties in the Brazilian Amazon, including the effect of phenology and seasonality on the monitoring of regenerating vegetation (Chapter 2), mapping large-scale human land cover change

(Chapter 3), and coarse resolution sub-pixel unmixing of land cover types (Chapter 4). The fourth study proposes a broadly applicable technique for quantifying the statistical uncertainty involved in estimating gross ecosystem exchange from an eddy flux tower (Chapter 5). Each chapter begins with a review of relevant literature.

CHAPTER 2

THE EFFECT OF SEASONALITY AND TIMING OF IMAGE ACQUISITION ON THE REMOTE SENSING OF REGENERATING VEGETATION IN THE SEASONALLY-DRY TROPICAL RAINFORESTS OF BRAZIL[1]

2.1 Introduction

Forests in the tropics continue to be cut at a rapid rate, primarily for use in agriculture, releasing carbon into the atmosphere in the form of CO_2. On a global scale, land cover change, primarily conversion of tropical forest, accounts for approximately 25% of all anthropogenic carbon release, with fossil fuel emissions and cement manufacturing making up the remaining 75% (Houghton, 2003). Often, these tropical agricultural areas are abandoned after a short duration due to poor soils or shifts in economic conditions, and forests regenerate on this land. Depending on the amount of time these forests are allowed to regenerate, as well as the rate at which they assimilate carbon, secondary forests can act as a carbon sink that offsets some deforestation carbon emissions.

[1] This chapter is based on and contains material from a manuscript submitted for publication in 2006: S.C. Hagen, W.A. Salas, S. Frolking, M.J. Ducey, and B.H.. Braswell (submitted). Effects of seasonality and timing of Landsat image acquisition on remote observation of tropical regenerating vegetation in Rondonia, Brazil. Submitted to *Remote Sensing of Environment*.

As the conversion of primary forest to agriculture continues, regenerating forests will likely represent a larger portion of the tropical landscape (Fearnside, 1996; Laurance et al. 2001). Therefore, understanding the biophysical properties of secondary vegetation has been an issue of growing interest. Field research has focused on identifying successional changes in species composition (e.g. Mesquita et al., 2001), rates of biomass accumulation (e.g. Uhl, 1987, Nepstad et al. 1991), and other structural changes in regenerating forests (e.g. Feldpausch et al., 2005).

Remote sensing imagery allows scientists and policy makers to evaluate this important dynamic process at regional to continental scales. Many studies have been devoted to mapping the presence and rate of clearing primary forest (Skole and Tucker, 1993). The importance of monitoring this rapidly changing landscape is clear and the process is straightforward because cleared land, as viewed from satellite sensors, is spectrally distinct from primary forest.

Other remote sensing studies have focused on the more nuanced task of mapping the extent, as well as the structural properties of regenerating forests. Moderate to high resolution (~30 m) optical data, such as the data provided through the Landsat program, are well suited for mapping the extent of young regenerating vegetation in the tropics. As confirmed by ground observations, high accuracies in mapping the extent of secondary vegetation have been reported (e.g. Mausel et al., 1993; Lucas et al., 1993; Nelson et al., 2000). However, regenerating forests eventually become spectrally indistinguishable from mature forest. The age at which this convergence occurs is reported to be between

15 years (Steininger, 1996; Moran et al., 1994a) and 30 years (Lucas et al. 1996) for single image multispectral remote sensing data, depending on environmental factors as well as analytical methodology.

Frequently cloudy conditions and the optically thick atmosphere in the tropics, combined with constraints from the satellite sensor, severely limit the number of clear images available (Asner, 2001), which complicates the process of monitoring land cover. In many areas of tropical South America, acquiring even a single cloud-free Landsat image in a year is not guaranteed. When assembling images from multiple years for analysis, one cannot expect to acquire imagery from the same time of year each year, and often one has to accept a clear image from any time of the year (e.g. Alves & Skole, 1996; Roberts et al., 2002). For monitoring and research projects such as mapping the changing extent of regenerating vegetation or the biophysical properties of regenerating vegetation, the effects of comparing images acquired at different times of the year are unclear. There have been only a few studies that examine seasonal reflectance differences in tropical ecosystems, such as those by Frietas et al. (2003), which examined the relationship between reflectances derived from two Landsat scenes and vegetation structure in Rio de Janeiro State, Brazil, Bohlman et al. (1998), which identified seasonal foliage changes in tropical vegetation using Landsat, and Kalacska et al (2005), which relates vegetation indices to forest structure in the wet and dry seasons. The effects of image timing on rainforest vegetation spectral reflectances from high to moderate (~30 m) resolution data has not been fully explored.

Over the course of a year, the biophysical properties of the vegetation and, correspondingly, the spectral signature of the vegetation can change for many reasons; e.g. human directed land use change, as well as seasonal phenology, growth, mortality, and stress of vegetation. Studies conducted on the ground, and more recently with high temporal resolution (e.g. MODIS) data, have documented phenological changes in tropical vegetation from the wet to dry season. Aide (1993) conducted a leaf census at a tropical site, measuring seasonality of leaf flush and leaf fall of understory vegetation, and noted two peaks of leaf production. Xiao et al. (2006), in a broad study of tropical South America using MODIS data, identified evidence of significant phenological patterns.

In this paper, we examine how the timing of the remote sensing observations affects the resultant land cover characterizations. Specifically, we document the spectral properties of the land surface in a dynamic area of the Brazilian tropical rainforest at the beginning and end of the dry season. The analysis is separated into two parts. In the first part, using atmospherically corrected Landsat reflectance data acquired over Rondonia, Brazil in May and August 2003, we analyze the spectral dynamics of several land cover features, with a focus on regenerating vegetation. In the second part, we extend this analysis by exploring the consequences that seasonal differences in spectral signatures have on thematic land cover mapping.

2.2 Study area and data

The area of study is approximately 19 km x 13 km centered around the coordinates 9.80° S, 63.37° W, west and slightly north of the city of Ariquemes in Rondonia, Brazil (Figure 1). The region has experienced rapid expansion in human settlement since the late 1960s when highway BR364 was paved (Dale et al. 1994). The cleared area in this region is primarily used as cattle pasture (Browder, 1994). There are also areas of annual (e.g. upland rice, beans) and perennial (e.g. coffee, bananas) crops, as well as areas of mining and logging (Browder, 1994, Dale et al., 1994, Alves et al., 2003).

In Rondonia, Brazil, the dry season (defined here as sequential months with < 100 mm $month^{-1}$ of precipitation) generally begins in May and ends in September (Figure 2). Cloud-free Landsat images are therefore most frequently available in these dry season months. Station precipitation data acquired for 2003 for the city of Ariquemes (approximately 25 km east-southeast of the study area) show that 2003 was a typical year (i.e. heavy rains ended in May and began again by October).

We geo-referenced and atmospherically corrected two Landsat ETM+ images acquired over this area in 2003. One image was acquired during the transition from wet season to dry season (20 May) while the other was acquired well into the dry season (24 August). To atmospherically correct these images, we used 6S software (Vermote et al., 1997) with estimates of the atmospheric optical depth derived from Aeronet data (http://aeronet.gsfc.nasa.gov/) acquired on the ground (Rio Bronco station). To validate the estimate of atmospheric optical depth, we examined MODIS (MYD08) estimates acquired daily at a one degree resolution. These estimates from the independent sources were similar, which increased our confidence in the atmospheric corrections.

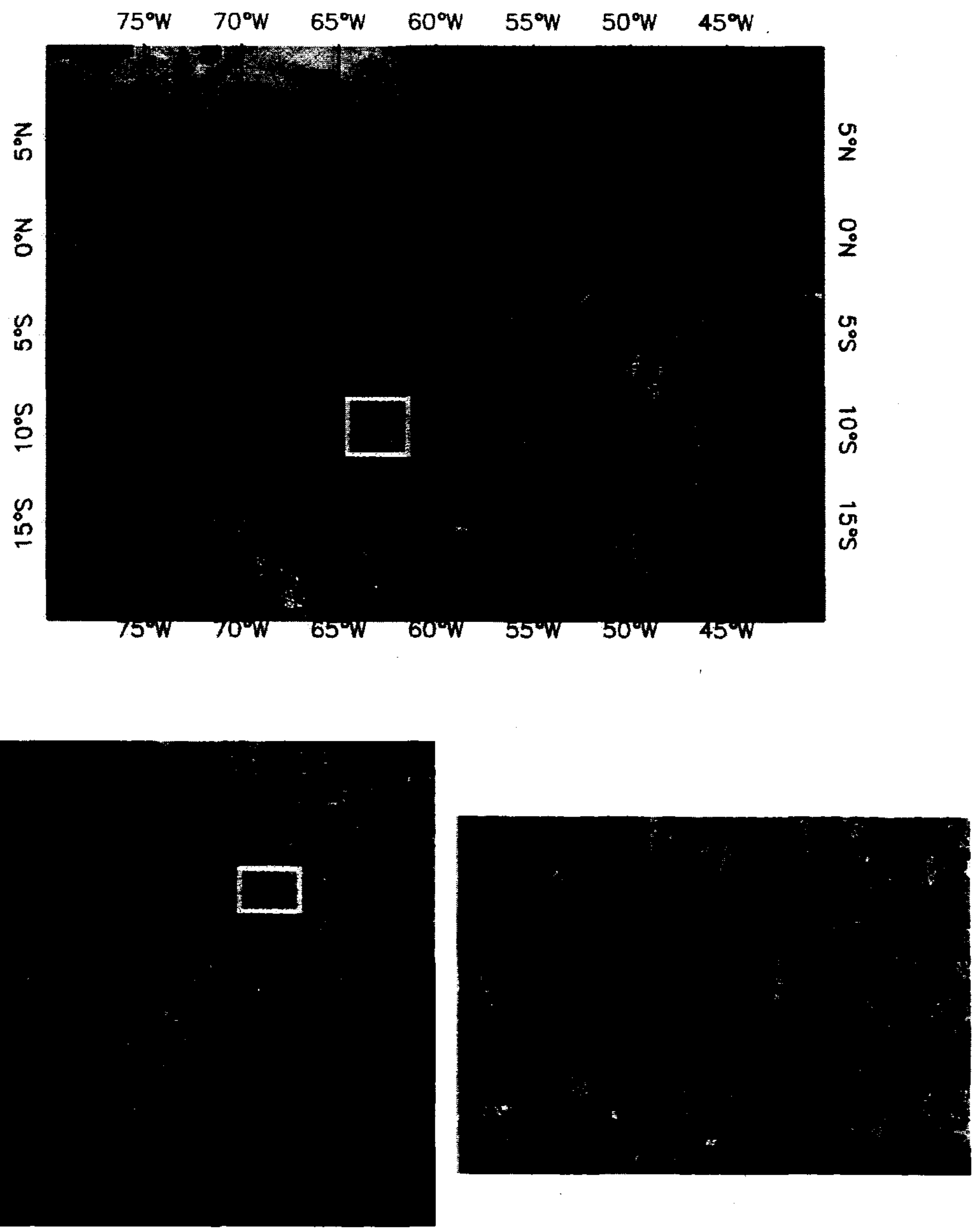

Figure 2.1. The area of study lies in the south western Amazonian state of Rondonia. The 19 x 13 km area is about 25 km west northwest of the city of Ariquemes.

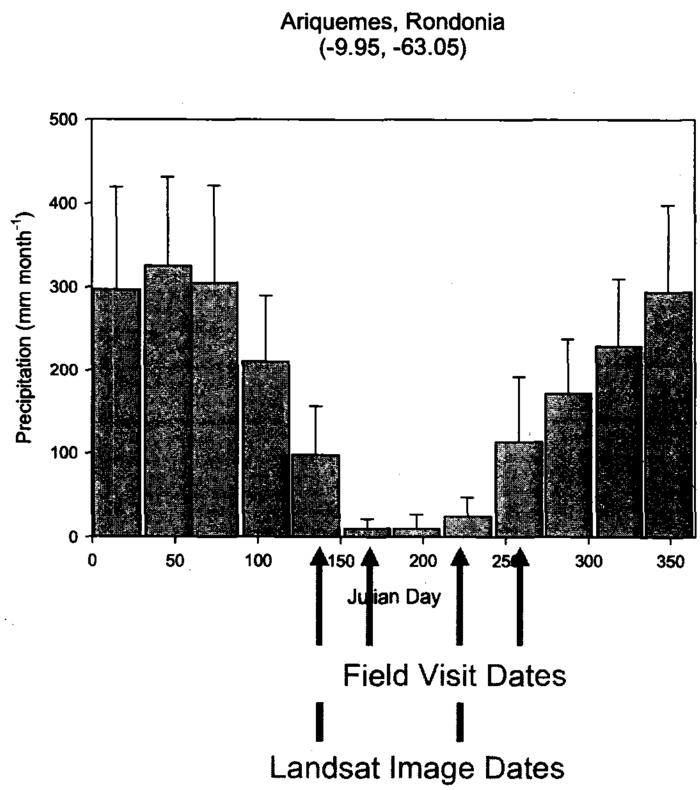

Figure 2.2. Long term average monthly precipitation (1960-1990; ± one standard deviation) for Ariquemes, Rondonia from a climate reconstruction (Willmott and Webber, 2003). The 2003 image acquisitions occurred at the beginning of the dry season (20 May) and at the end of the dry season (24 August). We visited the area and photographed the land cover about 30 days after each image was acquired (~20 June and ~25 September).

Additionally, we acquired and geo-referenced one Landsat image of this area for each year between 1989 to 2002 (Table 1). Each image was screened for cloud, cloud shadow, and water and the remaining pixels were classified, using an unsupervised classification technique (ISODATA), into three broad land cover types of interest: *mature forest*, *cleared area*, and *regenerating vegetation* (Figure 3). By stacking these fourteen images, we assembled a land cover transition matrix that contained a detailed land cover transition sequence for each 30 x 30m pixel (Skole et al. 1994; Kimes et al., 1999). We used this land cover transition sequence to identify forest stands for further study. Because the classified images are subject to the biases of seasonality studied in this manuscript, we selected regenerating vegetation stands for study only if a manual re-inspection of the time series of radiances yielded high confidence in the land cover transition sequence.

While the 1989-2001 imagery are used only for identifying areas for further examination, we used the two 2003 images to conduct the first part of our analysis (spectral) and added the classified 2002 image (05August) for the second part of our analysis (thematic). The 220 km^2 study area is effectively reduced to 154 km^2 because of missing data due to Landsat 7 scan line corrector problems (SLC-off) in the August 2003 image and clouds in the August 2002 image.

Year	Satellite
08 Jul 1989	TM
02 Dec 1990	TM
12 Jun 1991	TM
22 Jun 1992	TM
10 Jul 1993	TM
04 Jun 1994	TM
25 Jul 1995	TM
25 Jun 1996	TM
28 Jun 1997	TM
17 Jul 1998	TM
20 Jul 1999	ETM+
28 Jun 2000	ETM+
02 Aug 2001	ETM+
05 Aug 2002	ETM+
20 May 2003	ETM+
24 Aug 2003	ETM+

Table 2.1. List of Landsat imagery

We made two field trips to the region in 2003, once in mid-June and once in late-September. During the initial visit, we identified the land cover type and photographed with a digital camera over two-hundred randomly chosen points, each identified with a GPS. On the return visit in September, we re-photographed each random point and identified any change in the land cover.

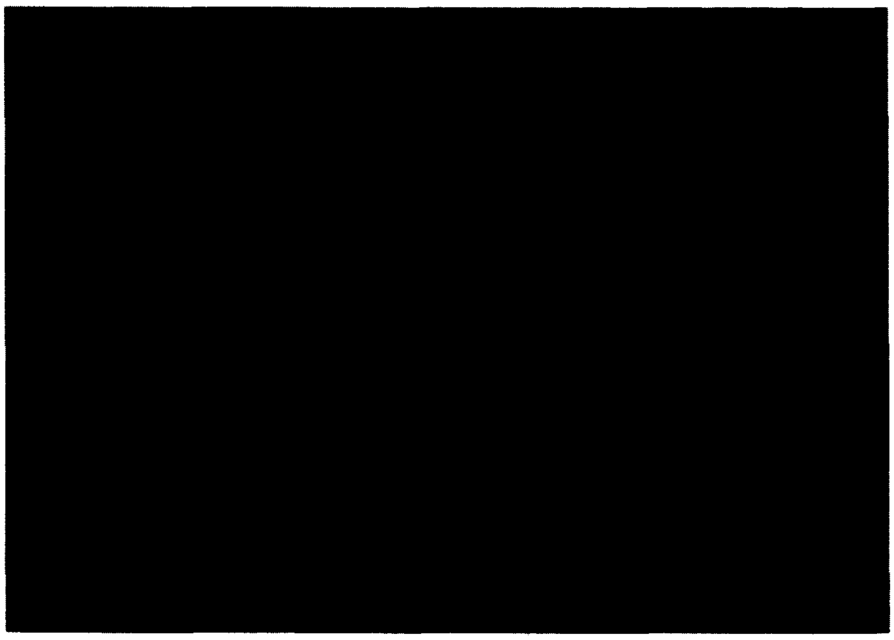

Figure 2.3. A three-class land cover map for the study area in the beginning of the dry season (20 May 2003) shows this area of the Amazonian rainforest has experience extensive conversion. Brown is *cleared area*, dark green is *mature forest*, and green is *regenerating vegetation*.

2.3 Methods

2.3.1 Spectral analysis of seasonal timing effect

To gain an understanding of how the spectral properties of tropical vegetation change over the course of the dry season, we extracted reflectance data for 83 areas of one hectare or more. These areas include 67 stands of *regenerating vegetation* comprised of contiguous pixels with identical land cover histories, ten contiguous *cleared areas*, and six contiguous *mature forest* areas. These areas were identified using the historical land cover transition matrix. We extracted six reflectance bands and four vegetation indices (Table 2) for all 83 stands and the stand mean and the stand variance for all reflectances and indices.

Band (*Index*)	**Wavelegth (*Index Formula*)**
BLU	0.45-0.52 μm
GRN	0.53-0.61 μm
RED	0.63-0.69 μm
NIR	0.78-0.90 μm
SWIR1	1.55-1.75 μm
SWIR2	2.09-2.35 μm
NDVI	(NIR-RED)/(NIR+RED)
EVI	2.5 * (NIR-RED) / (NIR + 6*RED - 7.5*BLU + 1)
LSWI	(SWIR1-NIR)/(SWIR1+NIR)
NIR:RED	NIR/RED

Table 2.2. List of bands and indices

We used these aggregated stand reflectance data to explore three issues related to land cover discrimination and seasonality. First, we examined the separability in spectral space of the three main land cover classes within a single time period (for both the May 2003 and the August 2003 image) using linear discriminant analysis. Then, we identified the change in the spectral signature of the three main land cover classes from the beginning of the dry season to the end of the dry season (May to August 2003). We also looked closely at the effect of two factors on the spectral signatures of regenerating vegetation: the time since abandonment (in years) for the stands of regenerating vegetation in the study area and the amount of time (in years) these abandoned areas stayed in the cleared class before they were abandoned (i.e. duration of use), using the fifteen-year land cover transition matrix. Duration of use may correlate with total intensity of use.

2.3.2 Thematic analysis of seasonal timing affect

The thematic land cover change analysis is intended to identify the effects of timing of imagery on classification of the land surface. Many monitoring studies and programs, such as Roberts et al. (2002), Ferraz et al. (2005), and PRODES, the Brazilian government's program for monitoring land cover change in the tropics, involve classifying Landsat images in areas known to be experiencing transition. These studies are limited by the availability of cloud-free images. Often, the option of examining images from the same week, month, or even quarter in two consecutive years does not exist, due to cloudiness. So, when assessing land cover and land cover change from one year to the next, it is common to have the time elapsed between image acquisitions range from 6 months to over two years. In this part of the analysis, we quantify the effect of the non-uniform intervals on estimates of land cover change.

The land cover change analysis involves looking at three land cover classifications of the study area: August 2002, May 2003, and August 2003. For the purposes of this analysis, we define the standard year for land cover change as beginning in August (end of dry season) and ending the following August. We define baseline changes as those occurring between August 2002 and August 2003. To quantify the effect of cutting the year short (i.e. the second image is acquired earlier in the dry season), we looked at the changes occurring between August 2002 and May 2003 (beginning of the dry season). Specifically, we are interested in the dynamic areas (e.g. areas that change from *mature forest*/*regenerating vegetation* to *cleared area* or from *cleared area* to *regenerating vegetation*).

2.4 Results and discussion

2.4.1 Spectral analysis

The three main land cover classes, *primary forest*, *regenerating vegetation*, and *cleared area* were most spectrally distinct in the NIR and SWIR1 bands (Table 2.3 and Figure 2.4). As other studies have shown (e.g. Steininger, 1996), primary forest and cleared area are spectrally distinct in most bands and indices. Using a combination of NIR and SWIR1, a linear discriminant analysis successfully classified 98% of the stands in the May 2003 image and 92% of the stands in the August 2003 image. These accuracies are similar to those reported in other similar studies (e.g. Roberts et al. 2002; Mausel et al. 1993). The separation in spectral space between regenerating vegetation and primary forest is clearer in the early dry season, while the separation between regenerating vegetation and cleared area is clearer in the late dry season (Figure 2.5). One potential explanation for the late dry season separation between cleared area and regenerating vegetation could be that secondary vegetation quickly establishes a deep enough rooting system to protect them from water stress during the dry season, while vegetation in pastures do not (Nepstad et al. 1994; Jipp et al. 1998). The different responses to reduced rainfall are most apparent in the SWIR band, which is known to be sensitive to leaf water content.

	NIR	SWIR1	EVI	RATIO	stdRATIO
Mature Forest	0.272 ± 0.013	0.120 ± 0.002	0.509 ± 0.023	13.9 ± 1.0	2.13 ± 0.17
Regen. Veg.	0.367 ± 0.030	0.154 ± 0.012	0.641 ± 0.040	16.5 ± 2.2	2.42 ± 0.65
Cleared Area	0.318 ± 0.046	0.202 ± 0.030	0.476 ± 0.076	6.0 ± 1.6	0.67 ± 0.50

Table 2.3. Class means and standard deviations of most distinct bands and indices

The spectral signatures of most cleared areas change drastically over the course of the dry season (Figure 5). At the beginning of the dry season (May-June in the study area), grasses tend to be lush and thick, often completely covering the soil. These cleared areas have spectral signatures closer to regenerating forests, with high NIR reflectance (around 30%) and moderate SWIR reflectance (around 20%). As the dry season progresses and the grasses dry out and are eaten by cows, revealing more soil, the NIR reflectance decreases to 25% and the SWIR reflectance increases to around 25%. NIR reflectance decreases for regenerating vegetation (from about 37% to about 32% on average), but the SWIR reflectance changes very little. The late dry season reflectances observed in this study are similar to the late dry season reflectances observed in another study (Steineger, 2000). The mature forests change very little from the beginning of the dry season to the end of the dry season. The only significant change is an increase in EVI. A study by Xiao et al. (2006) show maximum EVI levels occur in the dry season across much of the Amazon River basin, including Rondonia, and hypothesized that this peak is caused by leaf flush. Other studies also have shown that tropical primary forests often produce new leaves in the dry season (Aide, 1993; Haugaasen and Peres, 2005).

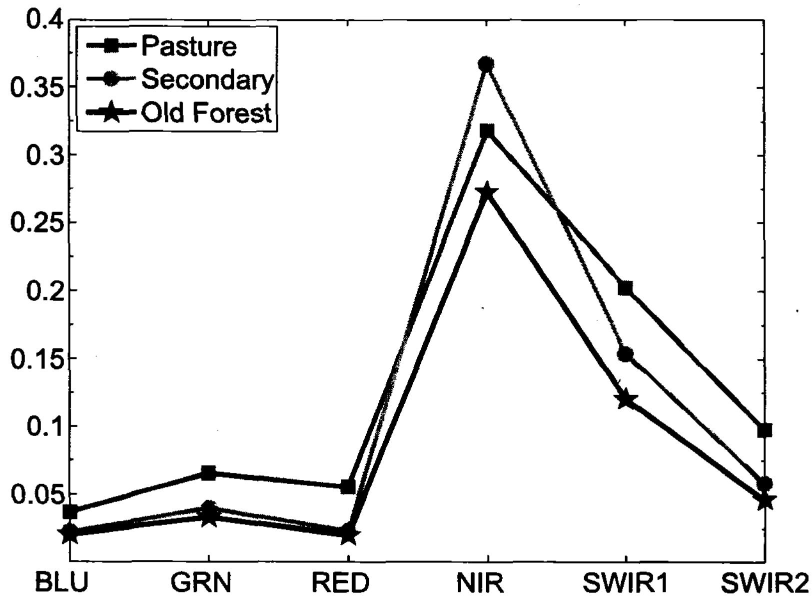

Figure 2.4. The mean spectral signals for the three vegetation classes are most distinct in the NIR and SWIR wavelengths.

We examined regenerating vegetation of different ages that were identified as having been cleared for only one year (i.e. short duration of use) to partially isolate the effect of age on the spectral signature of secondary vegetation. As briefly-used pastures begin the regeneration process from two years after abandonment up to sixteen years following abandonment, they show a clear general trend of decreasing NIR and SWIR reflectance (Figure 6). The decrease in SWIR with increasing age has been observed in other studies (Nelson et al. 2000, Steiniger, 1996, Lucas et al. 2002). The decrease in NIR with increasing age observed here is at odds with other study results. We note a peak in NIR reflectance before three years old, while some other studies have observed later peak in NIR (around seven years; Nelson et al 2000). Mausel et al. (1993) note a NIR peak during the "intermediate secondary succession", which is characterized by some larger trees (8-12 m). We observe decreasing NIR and SWIR with stand age nearly equally at the beginning and end of the dry season. Age, however, is an insufficient metric by which to classify regenerating vegetation because regeneration rate is affected by edaphic conditions, climate, land use history, and topography. As an alternative to age, Arroyo-Mora et al. (2005) proposed well defined successional stages, related to phenology, vertical and horizontal structure for classifying regenerating vegetation.

We also looked at 17 stands of four-year-old *regenerating vegetation* with mixed histories of duration in pasture before abandonment, in an attempt to isolate the effect of duration of agricultural use on the spectral properties. We could not identify any relationship between the spectral properties of these stands and the duration of agricultural use (from one year as cleared area up to five years), either at the beginning of the dry season or at the end of the dry season.

The accuracy of the spectral signature comparison between the May imagery and August imagery is directly dependent on the quality of the atmospheric correction procedure. Using the 6S atmospheric correction software (Vermote et al. 1997), we performed a simple sensitivity analysis on the atmospheric correction by estimating the effect that a change in atmospheric thickness has on the reflectances in each band. The May image is very clear and, according to both the MODIS data and AERONET station data, has a very low atmospheric thickness. Therefore, a ±10% change in the estimated atmospheric thickness parameter in the 6S model has a small effect on the reflectances in all bands in the May imagery. The August image has some visible clouds and an overall thicker atmosphere. A ±10% change in the estimated atmospheric thickness results in a 10 to

30% relative change in the visible reflectance, and approximately 5% relative change in the SWIR2 band. The NIR and SWIR1 bands we focus on in this study are the least sensitive to small changes in atmospheric thickness, changing around 1%.

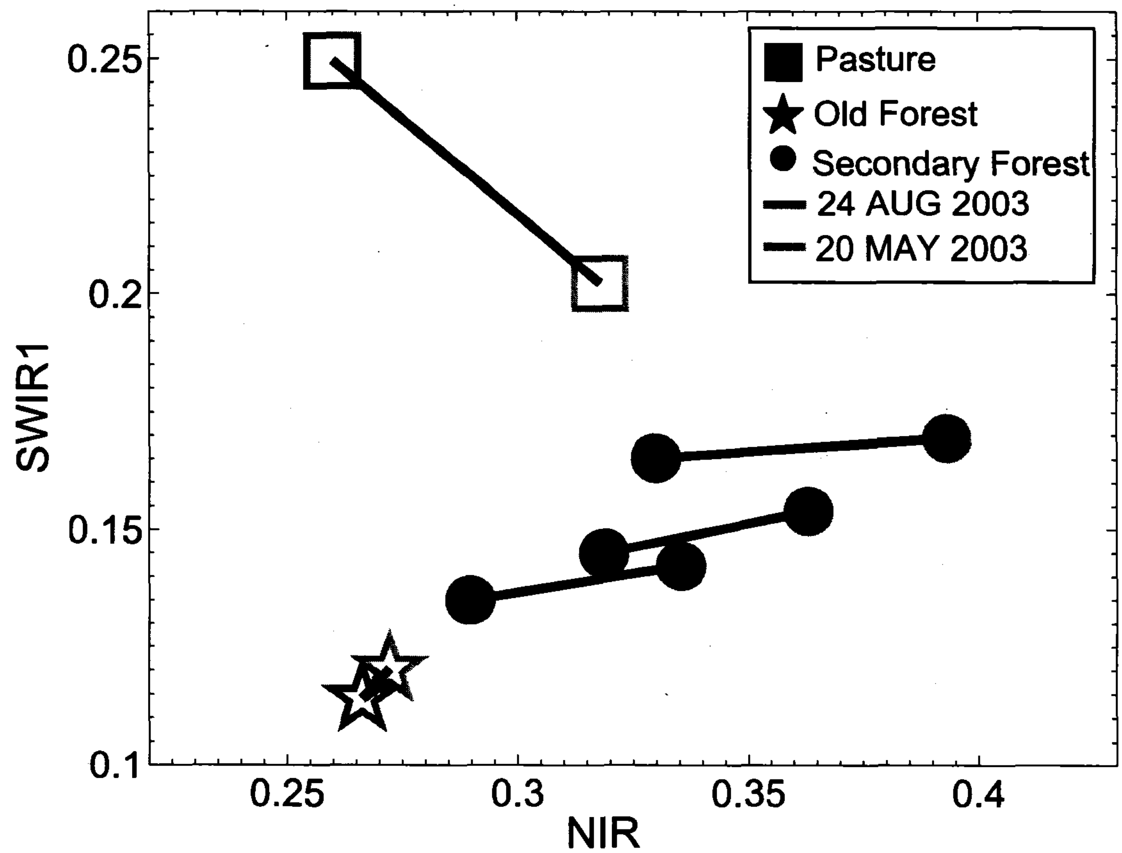

Figure 2.5. The SWIR1-NIR spectral space shows that cleared area (squares), regenerating vegetation (circles), and mature forest (stars) have distinguishable signatures in both the end of the wet season (green) and the dry season (red). The separation in two-dimensional spectral space between regenerating vegetation and primary forest is clearer in the early dry season, while the separation between cleared area and regenerating vegetation is clearer in the late dry season. As regenerating vegetation matures (light circles to dark circles, both green and red), NIR and SWIR reflectance decreases. This age-related dynamic, combined with the fact that regenerating vegetation show reduced NIR reflectance in the dry season, can complicate analysis using multiple images from different parts of the dry season. (Note the spectral similarity between moderately-aged secondary vegetation in the dry season and the oldest secondary vegetation in the wet season).

The fact that the spectral properties of *regenerating vegetation* change significantly over the course of the dry season complicates the process of relating single image optical reflectance data to vegetation structural properties and, in turn, affects thematic interpretation of the data, as has been noted by Roberts et al. (2002). The optimal parameters and architecture of a statistical model relating remote sensing reflectance to vegetation structure will change significantly from the beginning to the end of the dry season, making a generalizible model of vegetation structure unrealistic. Changes in the biochemical properties of the vegetation over the course of a season can affect the observed reflectances enough to obscure any relationship with vegetation structure. This general effect is demonstrated in our examination of different stages of regenerating vegetation (Figure 5). In particular, the medium age class at the end of the wet season is nearly spectrally indistinguishable from the older age class during dry season. Therefore, when relating tropical vegetation structure to remotely observed reflectances across multiple images (either in space or time), researchers should note that the date of image acquisition with respect to seasonality of precipitation can add an additional complication to the transferability of vegetation structural models beyond the complications already documented (e.g. constancies in biophysical environments and atmospheric correction; Foody et al., 2003; Lu, 2006).

(a)

(b)

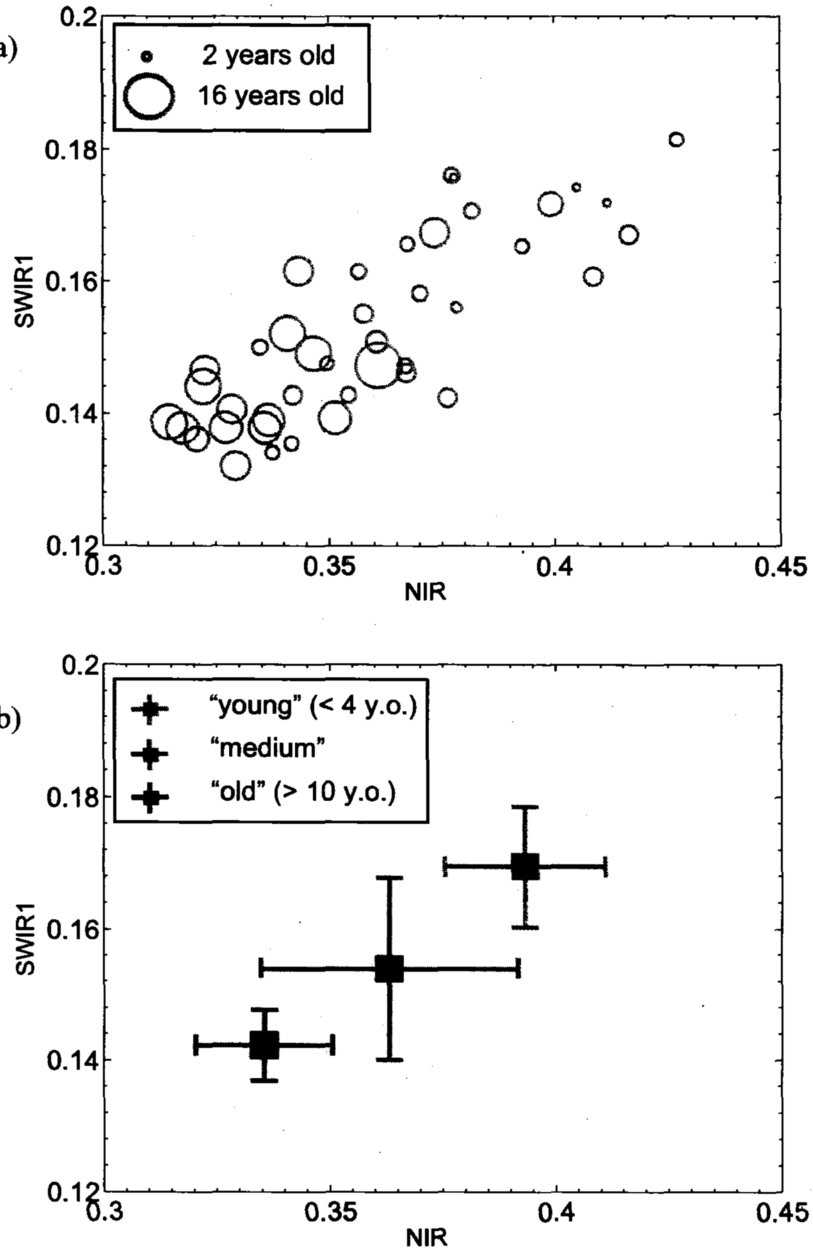

Figure 2.6. There is a general relationship between spectral reflectance and age of secondary vegetation in this area. The SWIR1-NIR spectral space, focused on regenerating vegetation at the end of the wet season, reveals a trend of decreasing NIR and SWIR reflectance as regenerating vegetation stands develop (a) (circles radius is proportional to age). Vegetation stands shown here were all in use as pasture for less than two years before they were abandoned. Aggregating into three age classes confirms this observation (b). The mean of each age class is statistically different from both other age classes. However, classifying individual regenerating vegetation stands into these age classes results in low accuracy.

2.4.2 Thematic analysis

Quite different conclusions will be inferred about the changing land surface if one examines a short year (AUG to MAY) as opposed to a complete year (AUG to AUG) (Table 4). Of the 74.6 km^2 of *mature forest* in the August 2002 image, 6.5 km^2 (or 9%) is cleared by May 2003, while an additional 3.2 km^2 is cleared by August 2003 (for a total of 13% of *mature forest* being cleared in the standard year). If examining a short year, one would miss one-third of all clearing of primary forest occurring in the complete year. If conducting repeated annual estimates, this missed clearing likely would be lumped together with the following year's totals, making rates that year appear significantly higher. The rate of clearing observed in this small study region is much higher than observed in other studies of Rondonia (e.g. Roberts et al. 2002, Skole and Tucker, 1993)

The August 2002 to May 2003 change analysis shows that 17.9 km^2 of August 2002 pasture (of 32% of the pasture) is abandoned to *regenerating vegetation* and 2.9 km^2 of August 2002 *regenerating vegetation* (or 12%) is recleared by May 2003. The August 2002 to August 2003 analysis shows a significantly different pattern. Only 12.3 km^2 of *cleared land* is abandoned to *regenerating vegetation*, while 4.2 km^2 of *regenerating vegetation* is recleared. These differences are due to seasonal changes in the vegetation structure and biochemical properties in addition to the timing of human activities, such as the clearing of forests. As noted above, in the May imagery when the grasses and small shrubs are the least water stressed, *cleared area* is more likely to be confused with *regenerating vegetation* than in an August image when some vegetation experiences more water stress.

	Pixels	Area (km 2)	Fraction Change
Forest AUG 2002	90657.6	73.64	--
Cleared AUG 2002	69048	56.08	--
Secondary AUG 2002	27531.4	22.36	--
Cleared Primary Forest MAY 2003	7985.4	6.49	0.088
Abandoned Pasture MAY 2003	21973	17.85	0.318
Recleared Secondary MAY 2003	3521	2.86	0.128
Cleared Primary Forest AUG 2003	11944.1	9.70	0.132
Abandoned Pasture AUG 2003	15183	12.33	0.220
Recleared Secondary AUG 2003	5935	4.82	0.216

Table 2.4. A summary of the thematic results show that quite different conclusions can be inferred about the changing land surface if one examines a short year (AUG to MAY) as opposed to a complete year (AUG to AUG)

The pixels that follow the classification sequence of *cleared* in August 2002, *regenerating vegetation* in May 2003, and *cleared* in August 2003 make up 8.6 km^2 or 20% of land classified as cleared in August 2002. There are two potential sources of confusion that arise from this particular land cover transition sequence. The first is a definitional issue. Defining *regenerating vegetation* is problematic, as others have noted (e.g. Feldspauch et al., 2005). How long does a period of inactivity have to last before an area is considered regenerating? If cows are removed from a plot of land for nine months, has the pasture been abandoned and should the plot now be considered *regenerating vegetation*? There is no agreed upon answer to this question. The other source of potential confusion is not definitional, but is related to the reflectance data. In the May 2003 image, these *cleared-regenerating-cleared* pixels have the same spectral signature as regenerating vegetation of two to four years old, indicating that this is not simply a matter of classification inaccuracies.

We compared the extended land cover history of the pixels with the peculiar land cover sequence *cleared* (AUG 02), *regenerating* (MAY 03), *cleared* (AUG 03) to the history of those that remained in the *cleared* class between 2002 and 2003. *Cleared* pixels that briefly appeared as *regenerating vegetation* in the MAY image had more often been originally cleared from forest more recently than those that remain *cleared* in all three images. Sixty-one percent of the *cleared* pixels that appear to be regenerating in MAY were originally converted from forest sometime *after* 1989, whereas 63% of the pixels that remain in the cleared class in 2002 and 2003 were originally converted from forest sometime *before* 1989. When tropical forest is converted to pasture, some of the original vegetation and seed stock typically survives the clearing and burning process (Nepstad et al., 1991). Repeated maintenance and reclearing of the pasture destroys the remaining original vegetation and seed stock. We hypothesize that the residual vegetation found in many newer pastures (i.e. recently converted from tropical forest) greens up in the wet season more than the grasses found in older, more established pastures that have been repeatedly cleared and maintained.

These results indicate that the timing of image acquisition can affect ones perspective when examining a dynamic tropical landscape. When examining an image from the early dry season in an effort to understand how the landscape is changing, one is more likely to get the impression that pasture land is being abandoned at an inflated rate and that the clearing of primary forest and regenerating vegetation is occurring more slowly than if one were to examine an image from the late dry season.

2.5 Conclusions and future work

The timing of image acquisition has a significant influence on the spectral appearance of the land surface and, therefore, on the conclusions one makes about the state and dynamics of the land cover. This is important to note in an area where the acquisition of clear moderate resolution images such as Landsat (30 m) is limited due to frequent cloud cover and an optically thick atmosphere. The spectral properties of cleared land and regenerating vegetation change significantly as the dry season progresses, while mature forest remains nearly spectrally constant.

Multiple images within a single year could add significant information useful for classification or for mapping biophysical properties. The availability of multiple Landsat or Aster images within a year, however, is rare. High temporal, coarse spatial resolution (~500m) data, such as MODIS can provide time series reflectance information useful in identifying seasonal changes related to phenology. It may be possible to combine this coarser resolution data with temporally limited Landsat imagery to improve classification accuracy or the mapping of biophysical properties.

This research identifies and quantifies a seasonal differences in tropical vegetation reflectance observations. With a better understanding of the seasonal dynamics of the tropical land surface, specifically regenerating vegetation, we can improve our ability to monitor changes in this ecologically important region.

CHAPTER 3

MULTI-RESOLUTION REMOTE OBSERVATIONS OF DEFORESTATION IN RONDONIA, BRAZIL[2]

3.1 Introduction

The direct alteration of terrestrial ecosystems by humans has played a significant role in the changing global carbon cycle (Schimel, 1995; Houghton et al., 2000). Principal driving forces behind these land cover changes, such as population dynamics and institutional economic and political factors, have been identified (Allen and Barnes, 1985; Hecht and Cockburn, 1989; Turner et al., 1994; Skole et al., 1994) and some integrative models exist (e.g., Frohn et al., 1996; Pfaff, 1999). However, prediction of large-scale socioeconomic systems is difficult and current land cover change research relies principally on monitoring via inventory and satellite imagery.

In tropical South America, political and economic pressures have combined to create sustained but variable impacts on the land cover (Fearnside, 1990; Houghton, 1991). The

---

[2] This chapter is based on and contains material from a paper published in 2002:
Hagen, S.C., B.H. Braswell, S. Frolking, W.A. Salas, and X. Xiao (2002). Determination of subpixel fractions of nonforested area in the Amazon using multiresolution satellite sensor data. *Journal of Geophysical Research*, 107, D20, 8049, doi:10.1029/2000JD000255. Reproduced by permission of American Geophysical Union.

dynamics of land cover change in this region can be described by a simple conceptual model with three (or more) possible land cover states and the corresponding sequence of transitions between them (Fearnside, 1996). A fraction of primary forest in a given region of interest can be cleared for pasture or cultivation. The cleared areas can then be maintained as agricultural land or abandoned. Secondary vegetation may also be subject to cyclical land-use patterns and are often returned to pasture or agriculture before reaching maturity (Fearnside, 1996; Salas, 2001). The resulting patches of forest regrowth on abandoned land (secondary vegetation) form a mosaic of vegetation types and structure. This situation is further complicated in some regions by partial clearing associated with logging, which is difficult to assess completely with any existing monitoring method, but is believed to be significant (Nepstad et al., 1999).

Satellite remote sensing has been used to document the transitions between tropical forest, agricultural land, and secondary vegetation (Skole and Tucker, 1993; Chomentowski et al., 1994; Stone et al., 1991). Many of these analyses are limited by uncertainties in the observations and the intrinsic trade-off between spatial and temporal resolution of the data.

A significant amount of research has focused on using coarse resolution remote sensing data, such as the Advanced Very High Resolution Radiometer (AVHRR), for mapping deforestation because of its broad spatial coverage, frequent overpass time, and low cost. These studies classify whole pixels (at a minimum resolution of 1.1 km) as a single land cover class. For example, Tucker et al. (1985) used AVHRR Local Area Coverage (LAC) data to map land cover in Africa, and Woodwell et al. (1987) mapped deforestation in the Amazon Basin with AVHRR LAC data. Also, Nelson and Holben (1986) examined the utility of coarser spatial resolution AVHRR Global Area Coverage (GAC) data for identifying clearings in Rondônia and determined that, while the high temporal resolution of the instrument (almost daily) is desirable, the clearings were too small to be resolved at the 4 km AVHRR GAC resolution. From these studies, we see that coarse to moderate resolution remote sensing alone cannot resolve many of the important details of land cover dynamics in tropical forests because these details occur at scales smaller than the resolution of the instrument. On the other hand, it is desirable to exploit the high temporal frequency and broad spatial coverage of global (coarse resolution) remote sensing data sets. High temporal frequency is advantageous, not because land cover is likely to change significantly in the nominal 16-day gap between Landsat images, but because an instrument that gathers images daily is much more likely to capture cloud-free glimpses of regional land cover on a consistent basis. This is particularly true in the humid tropics, where cloud cover is persistent (Asner, 2001).

Many studies have used fine spatial resolution data (e.g. Landsat MSS and TM) to classify land cover in the tropics for localized areas the size of a TM scene or smaller (e.g. Li et al., 1994, Steininger, 2000). Additionally, times series of land cover change have been assembled for similarly small regions in the Amazon using multiple acquisitions of fine resolution data (Mausel et al., 1993; Lucas et al. 1993; Alves and Skole, 1996; Kimes et al., 1999). Nelson et al. (2000) constructed a 7-year annual time series for a single TM scene in Rondônia with no temporal gaps (longer than one year) in a study of secondary forest age. Skole and Tucker (1993) completed a broader spatial analysis by assembling a land cover classification for the entire Amazon Basin for 1978 and 1988 using Landsat imagery. The studies that use fine resolution remote sensing exclusively have been limited either in their spatial coverage, usually to a single Landsat TM scene, or in their temporal resolution (i.e. they contain gaps longer than one year). Covering the Brazilian Legal Amazon requires over 200 Landsat scenes. Given this high data volume, in combination with the persistence of clouds in the tropics and low overpass frequency (16 days) of Landsat, mapping large regions like the Amazon Basin on an annual basis with Landsat imagery alone is prohibitive (Tucker and Townshend, 2000).

Woodwell et al. (1987) suggested that a more efficient and economical approach than using AVHRR or Landsat data alone would be to integrate the two products by using calibration factors that take advantage of both the finer resolution of Landsat and the more complete spatial and temporal coverage of AVHRR. Many studies have combined fine and coarse spatial resolution data for multi-resolution analysis (e.g., Nelson, 1989; Holben and Shimabukuro, 1993; Foody and Cox, 1994; Puyou-Lascassies et al., 1994; Oleson et al., 1995; Kerdiles and Grondona, 1995; Mayaux and Lambin, 1995; Atkinson et al., 1997; Asner et al., 1997). For example, Foody et al. (1997) used Landsat TM data and an artificial neural network to unmix fractional land cover within AVHRR pixels. Iverson (1989, 1994) used Landsat TM data to create a regression model to estimate the fraction of forest cover within an AVHRR pixel instead of classifying whole AVHRR pixels as a single land cover. Others (e.g. Zhu and Evans, 1994; Ripple, 1994, Hlavka and

Spanner, 1995) have used Iverson's approach for regional assessments of land cover in a variety of locations. In this paper, we extend this approach from single-year calibrated unmixing analysis to a time series of annual land cover assessments. We explore the potential of using multi-resolution remote sensing data in a generalizable way to monitor year-to-year changes in nonforested area of tropical regions at coarse spatial scales appropriate for use with climate and terrestrial models.

3.2 Site description and methods

This study focuses on approximately 30,000 km^2 of land surrounding the city of Ariquemes in Rondônia, Brazil (Figure 3.1). Several other tropical land cover change studies focused on this area (e.g. Stone et al., 1991; Alves et al., 1999; Nelson et al., 2000). The native vegetation in the area is predominantly dense tropical forest, with smaller areas of savanna, grassland, and alluvial vegetation (Alves and Skole, 1996). Rondônia has been the site of some of the fastest rates of land clearing and population growth in the tropical world. Before 1960, the area was sparsely populated, but since the early 1970's, Rondônia has experienced a tremendous rate of immigration and land use change (Stone et al., 1991).

We used two spatially and temporally coincident data sets for this study: a fine resolution time series of land cover for one TM scene and AVHRR GAC reflectance observations for the same area. Data pre-processing included degrading the fine resolution land cover data to fractional cover at an 8 km resolution, which results in a single data-layer for each class. Then, using the geolocation information provided with the data and ground control points identifiable in both data sets (e.g. large clearings associated with highways and cities), we coregistered the data sets with image visualizing software. Because alignment of the data features is difficult at the 8 km scale, we evaluated the co-registration by shifting the data one 8 km pixel at a time in each direction and noting the correlation between reflectance (AVHRR) and land cover fraction (TM). The test indicated no significant improvement in co-registration would result from a whole-pixel shift, so we conclude that the co-registration is accurate to within one 8 km pixel.

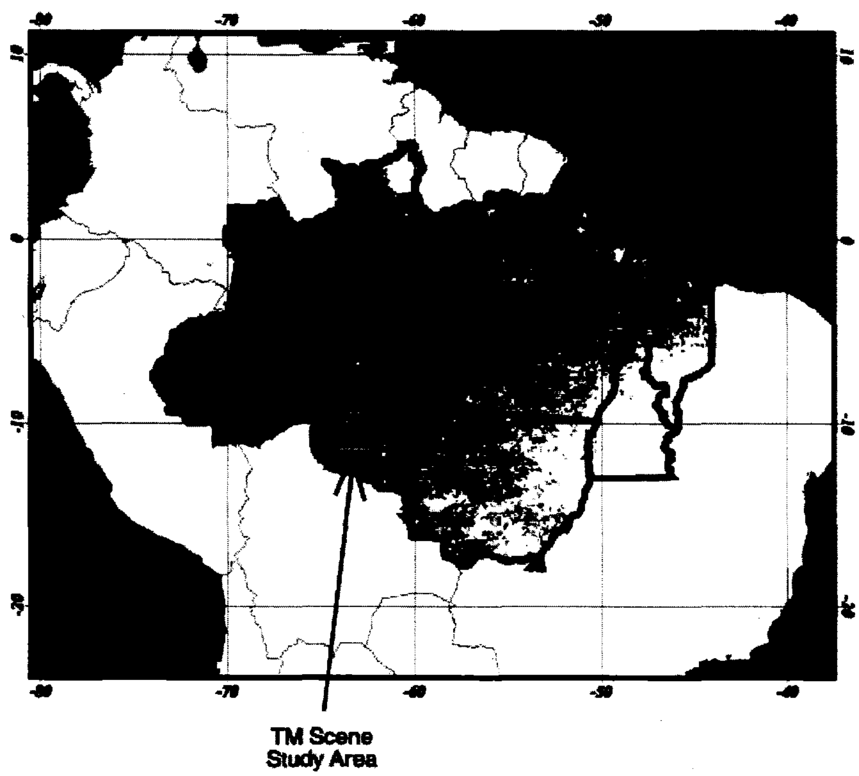

Figure 3.1. The region of study (white rectangle) is located in Rondônia, Brazil, in the southwestern portion of the Legal Amazon (comprised of the states in the dark outline). The color of 8-km pixels in the Legal Amazon represent the magnitude of the first principle component of channels 1, 2, and 3 in the 13-year averaged AVHRR data. This view, which combines all the available AVHRR reflectance data for each pixel, reveals details of land cover such as the cleared area in Rondônia and along the Trans-Amazon Highway (orange-pink-red coloring) and suggests usefulness of AVHRR time series data in identifying nonforested areas.

The land cover data were derived from a sequence of 30 m resolution Landsat TM images (Salas, 2001). The data set consists of 10 classified scenes, one per year from 1989 through 1998, for the same area around the city of Ariquemes in Rondônia, Brazil (Nelson et al., 2000; Salas, 2001). Each 30 m pixel is classified as mature forest, cleared area, secondary forest, cerrado, water, or cloud (see Nelson et al. [2000] for details of the classification procedure). The resulting product is a time series of land cover for each 30 m pixel in the scene. The total area cleared for pasture and agriculture within the region of this TM scene roughly doubled between 1989 and 1998, while the majority of the scene remained forested (Figures 3.2 and 3.3).

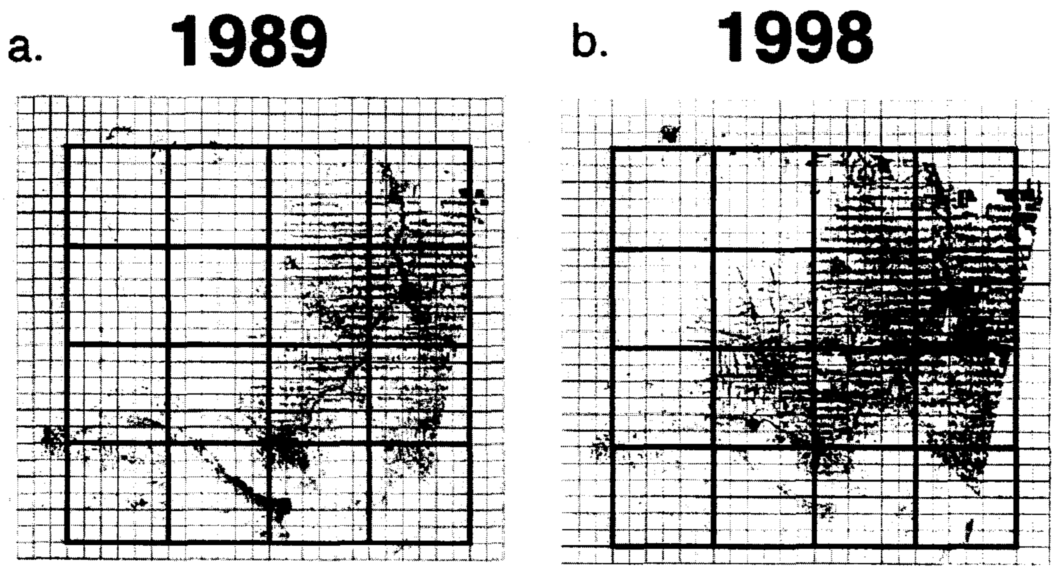

Figure 3.2. Land cover maps of the area around Ariquemes in Rondônia, Brazil for 1989 (a) and 1998 (b), derived from TM imagery [*Nelson et al.*, 2000]. Classes of land cover include forest (white), cleared area (red), secondary growth (green), water (blue), and cerrado (red). The grids overlaid on the land cover data indicate the resolution of the aggregations, 8 km (small grid) and 48 km (bold grid). These figures show an increase in cleared area at the expense of secondary growth and forest between 1989 and 1998.

Ten years (1989-1998) of AVHRR GAC data (10-day maximum NDVI value composite at 8 km resolution) were acquired from NASA's Pathfinder AVHRR Land (PAL) reprocessing effort [James and Kalluri, 1994]. In this study, we used Channel 1 (red, 0.58-0.68 μm), Channel 2 (near infrared, 0.725-1.1 μm), and Channel 3 (mid-infrared to thermal, 3.55 - 3.93 μm) data. We used Channel 1 and Channel 2 reflectance values to calculate the Normalized Difference Vegetation Index (NDVI = [(Ch2 - Ch1) / (Ch2 + Ch1)]). This index has been shown both in theory and in observations to be related to the amount of photosynthetic material in a canopy volume (Myneni et al., 1995; Asrar et al., 1984). Therefore, we assumed it is a good indicator of the amount of forest and nonforest area within a pixel because of their highly contrasting foliage density. We used Channel 3 data because it has also been shown to be sensitive to this contrast (Malingreau et al., 1996).

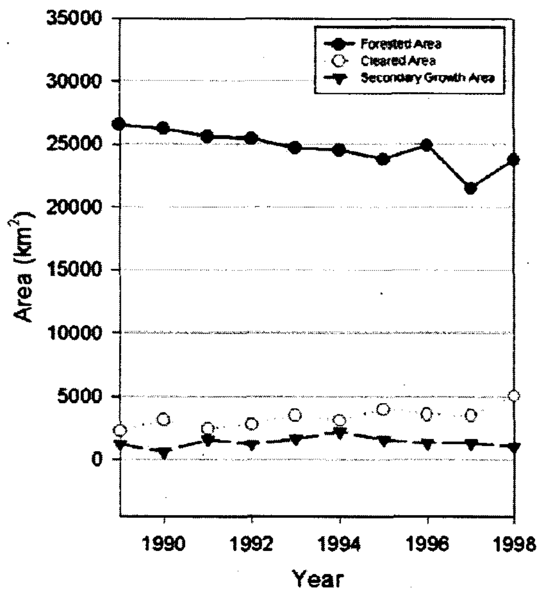

Figure 3.3. Land cover dynamics between 1989 and 1998 over the area covered by TM-derived land cover maps, showing a decrease in forested area over time. The sharp decline (1996-1997) then increase (1997-1998) in forested area is mostly due to significant cloud cover (~15%) in the 1997 TM scene rather than deforestation and near-instantaneous regrowth. The scene remains mostly forested throughout the time series.

To further reduce the effects of the atmosphere (e.g., spatial and temporal variations in water column vapor, clouds, aerosols) that tend to decrease the measured NDVI, we recomposited the AVHRR data to generate monthly data by extending the NDVI maximum-value compositing (Holben 1986; Asner et al. 2000). We selected the Channel 3 value from the 10-day composite associated with the maximum-value NDVI. These monthly values were subsequently averaged over the dry season (May to September) of each year (1989-1998). This resulted in annual NDVI and Channel 3 time series at 8 km for the area defined by the TM time series (smaller grid overlay in Figure 2).

We created a second, coarser resolution product for this analysis by aggregating the 8 km AVHRR data to 48 km. Our reasons for this were three-fold. First, each 8 km AVHRR GAC pixel is comprised of an irregular sub-sampling of 1.1 km LAC pixels, not an average of all of the 1.1 km pixels. Aggregating to 48 km likely produces a more representative average of the reflectance from the land cover, due to the larger sample size. Second, aggregating to 48 km reduces the effects of sub-8 km co-registration errors which would be apparent at the 8 km scale. Finally, at a 48 km resolution, pixels are commensurate with the spatial resolution of regional to global scale biogeochemical models (0.5° latitude/longitude near the equator) (e.g. Tian et al., 1998).

Using the spatially coregistered AVHRR and TM data, we determined the fractional cover of land cover types at the 8 km and 48 km scales based on the classified 30 m TM data. We combined the classes of cleared area and cerrado into a single nonforest class because these classes are spectrally indistinguishable at all AVHRR wavelengths. Secondary forest was defined in the Landsat classification as those areas abandoned and supporting forest after the original vegetation has been cleared (Nelson et al. 2000). Spectrally, regenerating forests exhibit reflectances somewhere between cleared land and mature forest, depending on the structure of the forest, which varies with age and regeneration stage (Uhl et al., 1988; Brown and Lugo, 1990).

After temporal recompositing and spatial aggregation, substantial interannual variability was apparent in the AVHRR data (Figure 3.4) in excess of variability that could reasonably be attributed to changes in vegetation cover alone. This spurious variability, linked to year-to-year clustering, is most likely due to changes in column water vapor, satellite drift, and aerosol optical depth, although sensor degradation and geolocation issues are also likely to play some role (Asner et al., 2000). We reasoned that a change in the relative location of a pixel within its annual cluster in NDVI/Channel 3 space was related to a change in the nonforest fraction in that cell, while year-to-year changes in the location of the clusters were due to non-vegetation effects. Therefore, to minimize this interannual noise and to preserve the relative location of a pixel within its annual cluster, we standardized the data by subtracting the mean values for "reference" pixels that remained dominated by forest (> 95% mature forest, about 1/5 of all 8 km pixels) over the 10-year time series and dividing this difference by the standard deviation of the reference pixels. We assumed there is no interannual variability in undisturbed forest pixels, averaged over the dry season. Some climate-driven effects related to moisture constraints on phenology may exist (Batista et al., 1997; Asner et al., 2000), but we assume that this variability would not be large enough to interfere with the discrimination between forest and nonforest. The standardization necessarily eliminated interannual drift

(Figure 3.4 and 3.5) and allowed us to focus on changes in nonforested area. After aggregating the original PAL 8 km AVHRR data to 48 km, we performed the same standardization procedure with the 48 km values, requiring that reference pixels always contain at least 90% mature forest (about 1/5 of the 48 km pixels).

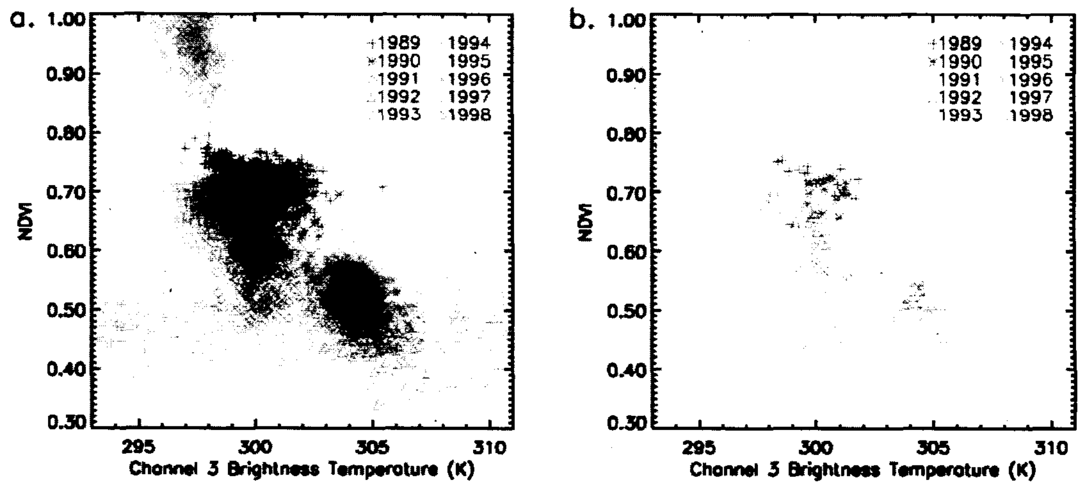

Figure 3.4. AVHRR data at (a) 8 km and (b) 48 km resolution in NDVI/Channel 3 space. The annual clustering of the data is due primarily to non-vegetation related artifacts.

Data from two of the original ten years were excluded from the analysis: 1995, because the AVHRR observations were incomplete due to satellite malfunction; and 1997, because of an excessive amount of cloud cover (~15%) in the classified TM scene (Nelson et al., 2000). With these years removed, the 8 km standardized data from the remaining eight years consisted of 3760 data points (470 grid cells x 8 years; Figure 3.5a). The 48 km data set consisted of 120 data points (15 pixels x 8 years; Figure 3.5b). The grid cell in the Southeast corner was left out of this analysis because the majority its area falls out of the TM scene most years (Figure 3.2).

We analyzed the sets of "data pairs" (i.e. the standardized values from AVHRR and the nonforested area from TM for each pixel) by fitting a linear model for the amount of nonforested area (A_{nf}) within a pixel as a function of the AVHRR data:

$$A'_{nf} = \beta_0 + \beta_1*(\text{NDVI}) + \beta_2*(\text{Channel } 3) = A_{nf} + \varepsilon \tag{3.1}$$

where the coefficients β_0, β_1, and $\beta_2$are estimated by regression, and ε is the residual error.

Estimates of nonforested area were then produced and examined at both the 8 km and 48 km resolution. The regression model in Equation (3.1) was fit using all the years of data grouped together, generating one set of coefficients (β). Additionally, lacking independent data for validation of the model, we performed a cross-validation. The cross-validation involved fitting a model iteratively using all the data points except one year's data, which was set aside for testing. The cross validation process generated eight sets of coefficients, one for each year.

As an exploration into the spectral characteristics of secondary forest, we added a free parameter, f, where $0 \leq f \leq 1$, indicating the fraction of secondary forest included in the nonforest class. Adjusting this fraction between zero (i.e. include all secondary forest in the forest class) and one (i.e. include all secondary forest in the nonforest class) could provide an information about the signature of secondary forest (i.e. its similarity to nonforest and forest). The effective nonforest area (A_{nf}) is given by:

$$A_{nf} = A_{cleared} + A_{cerredo} + f^* A_{sf} \quad (3.2)$$

where $A_{cleared}$ is the area classified as cleared (according to the 30 m classification), $A_{cerrado}$ is the area classified as cerrado, and A_{sf} is the area classified as secondary forest. We began our analysis by assuming that secondary forest does not contribute to the nonforest signal ($f = 0$) and examined the effects of this assumption later in our analysis. Finally, we considered in a stepwise fashion the necessity of using both NDVI and Channel 3 terms in Equation (3.1) and the relative value of using NDVI versus the red and near infrared reflectances in the regression.

3.3 Results and discussion

After standardization, the mean location of forest-dominated pixels (arbitrarily defined as < 25% nonforest with f=0) and nonforested pixels (≥25% nonforest with f=0) in Channel 3-NDVI phase space were significantly different ($p < 0.05$) in both the 8 km and 48 km analysis (Figure 3.5). This result indicates that standardization reduced the effects of many nonvegetation-related artifacts and that the AVHRR data contain information that will help resolve the amount of nonforested area within a pixel.

We included both NDVI and Channel 3 in the regression model, in part, because both variables, individually, are more significantly correlated with nonforested area (at the 48 km scale, Persons correlation coefficient R=0.84 and -0.57, respectively) than with each other (R=-0.46), suggesting that they may contain independent information. Additionally, several studies have suggested that both NDVI and Channel 3 are related to the disturbed area, though it is not clear whether they contain independent information (Woodwell, 1987; Malingreau et al., 1996; Di Maio Mantovani and Setzer, 1997). The analysis of variance for the regression model also indicated that both Channel 3 and NDVI significantly captured variation in nonforested areas. The results from these preliminary investigations are not strongly suggestive of independence between Channel 3 and NDVI, so it remains unclear whether Channel 3 is needed for unmixing fractions of nonforested area within large grid cells. We proceeded conservatively by employing a model containing both variables.

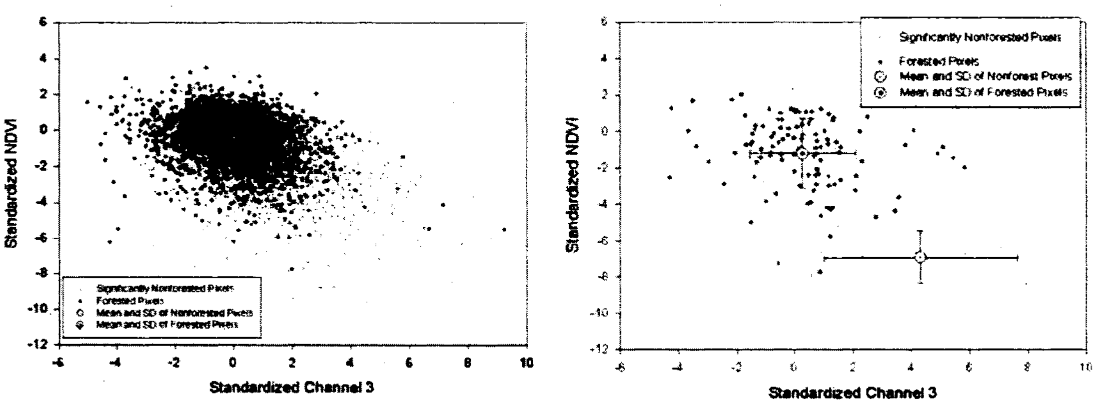

Figure 3.5. AVHRR standardized data at (a) 8 km and (b) 48 km resolution in NDVI/Channel 3 space. The annual clusters evident in non-standardized data (Figure 3.4) are not identifiable here. The data are split into two groups using the TM land cover data. Forested pixels (+) are those with more than 75% forested area. Significantly nonforested pixels (·) are those with at least 25% nonforested area. The figure also shows the means and standard deviations of the groups of pixels along the NDVI and Channel 3 axis.

The relationship between AVHRR NDVI and TM nonforested area was stronger at the 48 km resolution than at the 8 km resolution (R=0.84 vs. 0.56). The same results are seen in the relationship between Channel 3 and TM nonforested area for the two resolutions (R= -0.57 vs. -0.37). The results from the regression model, of the form given in Equation (3.1), that combines NDVI and Channel 3, reveal the same improvement of the 48 km resolution data over the 8 km data. The coefficient of determination (R^2) was 0.75 for the 48 km regression model and 0.35 for the 8 km model. The residual errors, ε, for the 48 km model were approximately normally distributed, while the 8 km model showed heteroscedasticity (visual inspection).

An analysis of how to account for secondary forest class gave no decisive answers. At both the 8 km and 48 km resolution, the coefficient of determination (R^2) of the model was relatively insensitive to the fraction of secondary forest included in the nonforest class (Figure 3.6). To simplify the analysis, f was fixed at a single value (f=0), thereby including all of the regenerating forest in the forest class and none in the nonforest class. We examined other potential models by including AVHRR Channel 1 and Channel 2 in place of NDVI. Studies have shown that near infrared reflectance (Channel 2) is strongly related to tropical forest regeneration stage (e.g. Lucas et al., 2000). In this study, these alternative models showed no improvement and were similarly unaffected by a change in f.

The results of the iterative cross-validation procedure also depended upon the scale considered (Figure 3.7). At the 8 km scale, the R^2 was 0.32 and the root mean squared error (RMSE) was 7.1 km^2 (11% of the grid cell area). At the 48 km scale the model produced an R^2 value of 0.64 and a RMSE of 146.6 km^2 (6% of the grid cell area). Using

NDVI only, the results were not significantly different than the model that includes Channel 3 (not shown). To establish the extent to which the model captured changes in land cover over time, we grouped the cross-validation results by year and summed to the TM scene level. This process produced a single time series with an annual time step for the TM observed values of nonforest and for the AVHRR cross-validated predictions derived from each resolution (Figure 3.8). We found the model derived using 48 km aggregated AVHRR data captures most of the interannual fluctuations in nonforested area (R=0.91) while the 8 km data is less successful (R=0.73).

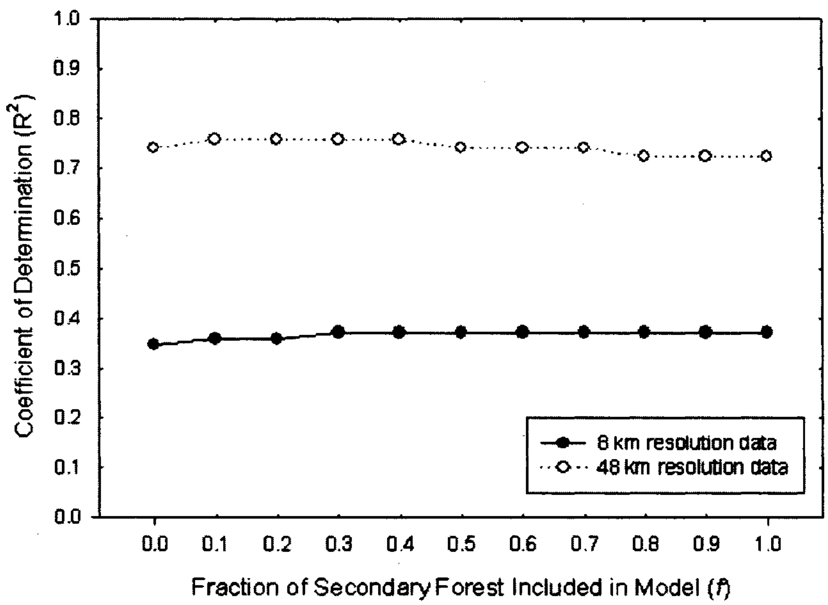

Figure 3.6. The coefficient of determination (R^2) of the model (Equation [3.1]) as a function of the free parameter *f*, or fraction of secondary forest included in the nonforest class (Equation [3.2]), at 8 km and 48 km resolutions. Correlations had little sensitivity to secondary forest fraction.

To evaluate whether this model could recreate interannual dynamics of land cover *at the pixel level,* we compared the time series predictions of the cross-validation model to the observed nonforest fraction at each pixel. The results of this comparison were very poor at the 8 km resolution (not shown) and leave little hope of reconstructing a time series at this scale. At the 48 km scale, however, the results were noticeably improved (Figure 3.9). The predicted time series for the pixels that did not change considerably over the ten years of this analysis (the four pixels having a net change in the nonforested area from 1989 to 1998 of less than 30 km^2 [2% of the pixel]) show no relationship to the TM observed time series. The six pixels that underwent a moderate change of between 30 km^2 and 350 km^2 (1% to 15% of the pixel) have a moderate relationship between time series of predicted and observed nonforest fraction (R=0.38 to 0.66). The five pixels that experienced the largest changes over the study period (>350 km^2) have the strongest relationship (R=0.81 to 0.97) between predicted and observed nonforest fraction. Therefore, fine resolution data about changes in land cover at a decadal time step (Skole and Tucker, 1993) could be used to pre-select pixels for an analysis of the type presented here. Pixels that change little in a ten-year time period could be omitted from the analysis.

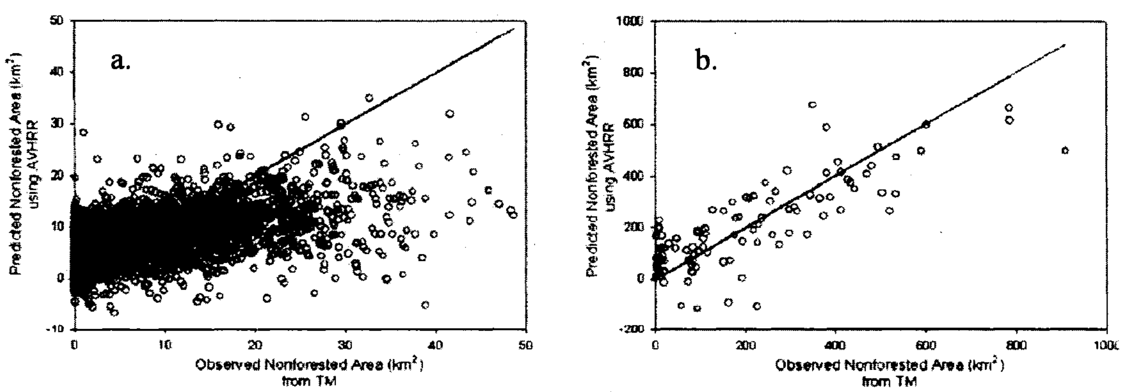

Figure 3.7. AVHRR predicted vs. TM observed nonforested area based on cross-validation data at (a) 8 km and (b) 48 km resolution. Both figures include the one-to-one line.

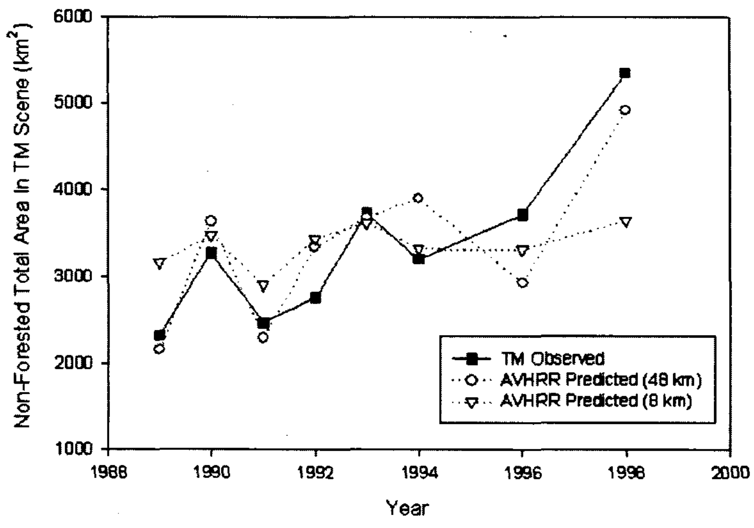

Figure 3.8. Time series of nonforested area summed over TM scene using the cross-validation data at the 8 km and 48 km resolution. The time series of AVHRR predicted area in the 48 km resolution model (dotted line, circles) more accurately follows the TM observed area (solid line, squares) than the AVHRR predicted area in the 8 km resolution model (dotted line, triangles).

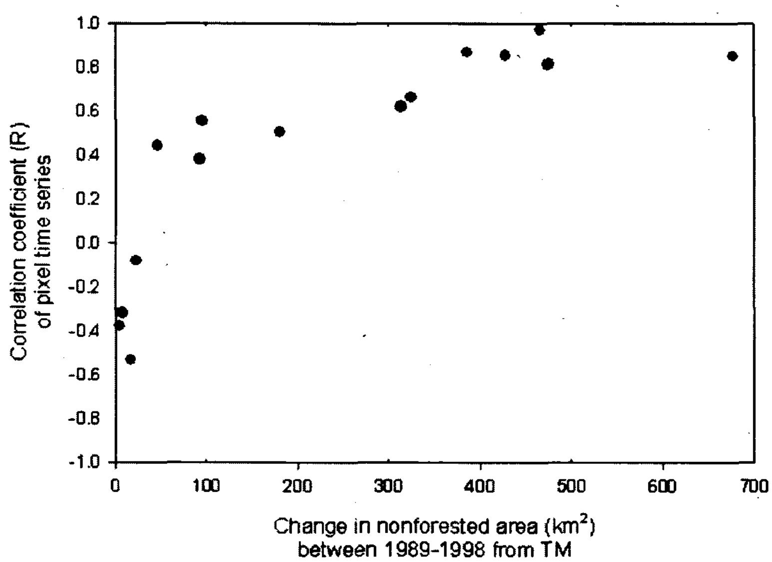

Figure 3.9. Temporal correlation (R) vs. change in nonforested area between 1989 and 1998 by pixel at the 48 km resolution. At the 8 km resolution (not shown), there was no relationship between temporal correlation and change in nonforested area. At the 48 km resolution, the level of correlation between the predicted and observed data at the pixel scale is related to the amount of land cover change over the 10-year time series. Pixels that change significantly over the time period are accurately predicted by the AVHRR model.

3.4 Conclusions

Given the rapid and significant changes in tropical ecosystems associated with human disturbance, it is desirable to use existing remote sensing data to produce historical reconstructions of disturbed areas over time. The fine resolution Landsat data acquired since the 1970s represent a valuable store of information. This massive amount of data has been effectively transformed into usable products (e.g. Chomentowski et al., 1994; Townshend et al., 1995) describing the state of ecosystems in the region. On their own, however, these fine resolution data are not adequate to ascertain the transitions of land cover at a time scale relevant for modeling global biogeochemistry, ecology or land-atmosphere interactions. Similarly, the global AVHRR data (1982-present) are the only terrestrial observations available at spatial and temporal intervals that are regular and compatible with the scales of regional and global modeling. Technical complications and the coarse resolution of the observations, however, make interpretation difficult.

Currently, terrestrial ecosystem models that consider distributions of land cover classes within relatively large grid cells (e.g. Moorcroft et al., 2001, Tian et al., 1998) are limited by a dearth of temporally and spatially rich land cover data. For this reason, a historical land use product derived from a statistical combination of TM and AVHRR may be valuable to the modeling community. The unmixing method detailed here could be useful in interpolating annual estimates between the decadal estimates that are based solely on fine resolution data (e.g. Skole and Tucker, 1993). This study demonstrates that annual estimates based on this unmixing approach are an improvement over a strictly linear interpolation between decadal products in this region of the tropics.

The analyses conducted in this paper demonstrate that reconstructions of changes in land cover distributions may be possible, but with limited accuracy at the 8 km spatial resolution of the AVHRR Pathfinder product. It is clear that the maximum-value compositing and standardization employed here were not sufficient to account for effects caused by water vapor, aerosols, GAC sampling, and geo-registration complications. It is therefore likely that GAC-based AVHRR observations of the Amazon Basin are too noisy to extract reliable biophysical information about the land cover at the 8 km resolution.

The retrievals at 48 km were much more successful. These noted improvements likely result from two features of the aggregation process. First, aggregating the 8 km data dilutes the effect of co-registration errors. Second, each aggregated 48 km pixel has a larger sample size than the 8 km PAL AVHRR GAC pixels. The 8 km reflectances are averages of an irregular sub-sampling of the original LAC 1.1 km reflectances, not a measure of the reflectance from the entire 8 km pixel. Aggregating up to 48 km increases the number of 1.1 km LAC pixels that comprise the average and, therefore, produces reflectance values that are more representative of the actual land cover. Thus, the power of a regression-based unmixing approach, such as the one presented in this paper, is most appropriately measured at spatial scales much larger than the single grid cell level (8 km in our case).

Our results suggest that fine resolution remote sensing data can be combined successfully with moderate resolution data to provide accurate estimates of land cover distributions at a combined spatial and temporal resolution that is a compromise between the two types of data. This general approach is not necessarily limited to the use of parametric statistics or the assumption of linear relationships between reflectances (or indices) and land cover fractions (Braswell et al., 2000). Despite its name, Advanced Very High Resolution Radiometer, AVHRR can no longer be considered advanced or very high resolution. With new moderate remote sensing data that are designed to observe the terrestrial biosphere (e.g. MODIS), and fine resolution data (e.g. ASTER) that are designed to be used with their moderate resolution counterparts, we expect improvements in regression-based unmixing approaches due to improved atmospheric correction calibration and improved knowledge of bidirectional reflectance distribution functions (BRDF), not to mention the finer spatial resolution of the global datasets.

CHAPTER 4

MAPPING SUB-PIXEL LAND COVER DISTRIBUTIONS USING MODIS AND MISR IN THE BRAZILIAN AMAZON[3]

4.1 Introduction

The Brazilian Amazon region consists of over 4,000,000 km^2 of tropical forest, representing one of the largest and most diverse contiguous ecosystems in the world. Over the past two decades, dramatic land cover changes in Amazonia have resulted in a wide variety of ecological and biogeochemical impacts, ranging in scale from local to global, and including changes in forest productivity and composition, nutrient dynamics, species diversity, stream chemistry and atmospheric carbon dioxide (Houghton et al., 2000; Potter et al., 2001). Furthermore, alterations in forest structure are thought to impact regional climate via biophysical feedbacks between the atmosphere and biosphere (Costa & Foley, 2000; Walker et al., 1995). Therefore, quantification of the magnitude, timing, and spatial extent of human modification of the landscape in this region is currently an important Earth science research topic.

---

[3] This chapter is based on and contains material from a paper published in 2003:
Braswell, B.H., S.C. Hagen, S. Frolking, and W.A. Salas (2003). A multivariable approach for mapping sub-pixel land cover distributions using MISR and MODIS: Applications in the Brazilian Amazon region. *Remote Sensing of Environment*, 87, 243-256.

While deforestation-related land cover changes are widespread, affecting nearly 600,000 km^2 in the Brazilian Amazon region alone, they occur at small spatial scales and exhibit highly dynamic interannual variability (INPE, 2000). The affected areas are thus a constantly evolving mosaic of cleared land and secondary vegetation fragments of varying size and age, woven into a background of relatively undisturbed forest. Because the underlying causes and resulting patterns of land use activity in Amazonian forests depend upon a variety of economic, social, and ecological factors that are extremely difficult to document, quantifying disturbance and recovery of Amazonian forests is typically addressed with satellite remote sensing techniques.

The objective of this paper is to present an approach for mapping land cover distributions using data from multiple-scale satellite observations, with specific application to estimating patterns of deforestation and recovery in Brazil. We present and evaluate a method for estimating sub-pixel land cover fractions that is unique in the following ways: (1) the scaling between Landsat ETM+ and Terra (MISR and MODIS) data is accomplished using an artificial neural network method that is designed to prevent overfitting; and (2) we combine multiangle and multispectral data from the two Terra sensors and compare the utility of various band-angle combinations. In the following section we will review some of the strategies that have been previously used, and briefly discuss the surrounding analytical and remote sensing issues that form the foundation of our approach.

4.2 Background

4.2.1 Resolving land cover change patterns

The availability of wide-swath, coarse spatial resolution data from polar-orbiting instruments (e.g., AVHRR, MODIS, and MISR) allows classification of large regions at kilometer scales and greater. A number of these products exist (e.g., Loveland et al., 2000, DeFries et al., 1998), and they are often intercalibrated with one another or linked to field data and censuses (e.g. Cardille et al., 2002; Frolking et al., 2002). These data sets have been useful in a wide variety of applications, particularly those involving global models of climate and ecosystems. The main drawback to this approach is that the scale of land use and land cover change in Amazonia is usually smaller than the ~1 km resolution of these instruments. Classifying coarse resolution pixels as a single type of land cover will result generally in poor accuracy and specifically in an overall underestimation of non-dominant classes (Nelson & Holben, 1986).

An alternative approach to regional land cover assessment in Amazonia involves the construction of spatially comprehensive maps at high-resolution, by classifying and mosaicking the hundreds of Landsat Thematic Mapper (TM) scenes that are necessary to cover the region (e.g. Skole & Tucker, 1993). The advantage of this approach is its potential accuracy, because of the high degree of detail provided by the 30m resolution TM pixels. Many land cover and land use patterns in tropical Brazil are larger than the 30 m resolution of this data, have relatively distinct spectral signatures, and thus can be resolved very well in this approach. The disadvantages of this strategy involve the great deal of money and effort to acquire and analyze the TM imagery. Also, for this area, the 16-day repeat overpass frequency of Landsat will fail in most years to collect completely cloud-free imagery over the entire Basin (Asner, 2001). These constraints make the production of high-resolution basin-wide products at an annual temporal resolution difficult.

A compromise solution, capitalizing on the advantages of the first two approaches, can be achieved by combining high resolution and coarse resolution data. This family of techniques attempts to preserve detailed land cover information available at small spatial scales, while extending the spatial and temporal coverage using coarse resolution data. Typically, a subset of possible high-resolution data (e.g., TM) within the region is obtained, classified, and coregistered with the coarser scale data (e.g. AVHRR). An empirical relationship between the two data sets is then derived for the sampled areas and applied to the larger region, resulting in maps of fractional coverage of the specified surface types. Research in this area has primarily involved using one of two classes of techniques: linear spectral unmixing or multivariate regression methods. We discuss these approaches in the remainder of this Section.

In linear spectral unmixing, spectral endmembers (reflectance profiles for pure classes) are identified or prescribed, and spectral endmember libraries are assembled that contain the reflectance properties of each end-member. The spectral library is then used to estimate the class composition of every pixel. This process is frequently referred to as unmixing. Unmixing has been applied to both fine and coarse resolution data, with the same principles, though the end-member sets often change at different scales. For example, Adams et al. (1995) used fine resolution data to unmix proportions of sub-canopy components such as photosynthetic vegetation, woody vegetation, soil, and shade within Landsat TM pixels (30 m). A number of studies using coarse resolution data have demonstrated the feasibility of unmixing sub-pixel land cover types from AVHRR pixels (1000 m) (Atkinson et al. 1997; Hlavka & Spanner, 1995; Kerdiles & Grondona, 1995; Cross et al., 1991). The main advantage of this method, besides its potential for efficient use of costly high-resolution data, is that it requires only the assumption that different land cover mixtures exhibit more or less unique spectral signatures in the large-scale data.

Several studies have demonstrated the applicability of a linear regression-based scaling approach to land cover fraction estimation in the US (e.g. Iverson et al, 1994; Zhu & Evans, 1994) and in Amazonia (e.g. Hagen et al., 2002). Non-linear regression, in the form of artificial neural networks (ANN), is also gaining popularity as tool in remote sensing land cover mapping. Several studies have shown ANNs to be at least as effective as other sub-pixel fractional estimation methods due to their ability to adapt to non-linear relationships between the data sets (e.g. Atkinson et al., 1997; Foody et al., 1997). Most of these applications of neural networks involve fixed parameters for learning rate and iterations. The optimal values for these parameters will vary depending of specific applications. More recently, MacKay (1994) has proposed a technique from Bayesian statistics for selecting optimal network parameters. The technique minimizes over-fitting by penalizing large network weights. The Bayesian modification to the artificial neural network also provides a framework for estimating uncertainty associated with each estimate. Uncertainty estimates are increasingly recognized as an important component of land cover analysis.

4.2.2 Data sets for regional land cover mapping

Two instruments aboard the NASA Terra satellite platform, MISR and MODIS, have the appropriate spatial and temporal coverage for large-scale land cover analyses. Furthermore, they have observational characteristics that likely provide complementary information about land surface characteristics: (1) near simultaneous multi-angular sampling of MISR, and (2) multiple shortwave-infrared bands of MODIS. In this section we discuss the relevance of these two aspects

Studies involving the use of multiangle remote sensing data in regional-scale terrestrial analyses are relatively scarce, though the potential for capitalizing on these data for land cover and biophysical retrieval has been demonstrated both in theory and in the field (e.g. Asner et al. 1998; Deering, 1989). The observed dependence of surface reflectance on sun-sensor geometry provides a discrete sampling of the bidirectional reflectance distribution function (BRDF). The BRDF is analogous to a spectral signature, and is known to be sensitive to land surface properties, including the three-dimensional structure of vegetation canopies (Grant, 2000). Several studies have used multi-angular observations for resolving structural properties of vegetation using POLDER data (e.g., Grant, 2000; Lovell & Graetz, 2002). Other researchers have created synthetic BRDFs by assembling multiangular observations from successive overpasses of single view angle instruments like AVHRR (e.g., Privette et al., 1996, Braswell et al., 1996). With the launch of the EOS Terra satellite, multi-angle data with regional coverage is now available from MISR, which images each location on Earth from nine angles, with a sixteen day ground track repeat cycle and nine day repeat global coverage.

The utility of shortwave-infrared (SWIR) (1.2 to 2.5 μm) bands for land cover characterization is now apparent based on many studies using ETM and SPOT-VGT. These mapping efforts, as well as successful application of SWIR-based indices like the Normalized Difference Water Index (NDWI; Gao et al., 1996), illustrate the unique sensitivity of SWIR reflectance to canopy structure and moisture content. In the tropics, a decrease in SWIR reflectance has been correlated with increasing canopy diversity and foliar structure changes that are associated with aging of secondary vegetation (Steinenger, 2000; Lucas et al., 2002). The MODIS instrument aboard Terra measures surface reflectance in three SWIR bands.

4.3 Methods

In this study, we produced a set of sub-pixel land cover fraction estimates at a moderate spatial scale (~1 km) in two heavily impacted regions of the Brazilian Amazon region. The estimates were predicted using reflectance data from MODIS and MISR, based on known land cover estimates derived from unsupervised classification of ETM+ with manual image editing. Thus, the coarse resolution observations, derived from the available bands and view angles, are treated as independent variables in a top-down statistical approach. We compared the relative utility of two estimation techniques, and explored the effects of data characteristics by analyzing the output of 11 cases (Table 4.1). In all cases we measured the accuracy using the observed land cover fractions from ETM+.

4.3.1 Study sites and data sets

We selected a pair of sites in Amazonia, separated by over 700 kilometers (Figure 4.1), which are the subject of a detailed analysis of land cover conversion and recovery (Nelson et al., 2000; Salas, 2001). One study area is in the Brazilian state of Para along the Trans-Amazon Highway. This region is characterized by a moderately undulating terrain, and intensive land use that extends away from the highway. The native vegetation in this area is moist evergreen tropical forest, except in some small patches along the Iriri River where the natural land cover is relatively sparse vegetation and flooded forest. The city of Ruropolis is near the center of this scene (Figure 4.2b). The other study area is in the state of Rondonia, near the city of Ariquemes (Figure 4.2a). The native vegetation in this region is also dense tropical forest. These two sites were chosen primarily because of their climatic and edaphic differences, which are assumed to affect vegetation structure and function. It is also possible that their unique land-use histories have led to differences in biophysical characteristics (Stone et al., 1991).

We used satellite data from three sensors in this analysis: Landsat ETM+, MODIS (MOD43), and MISR (MISR L1B and L2). We use the 30 m resolution Landsat ETM+ reflectance data to classify land cover into five broad types: (1) *mature forest*, (2) *cleared land* (for pasture, roads, or cultivation), (3) *secondary vegetation*, (4) *water*, and (5) *cloud/cloud shadow* (Figure 4.3). We conducted the unsupervised classification using the ISODATA technique (Jensen, 1996). The ETM+ reflectance data were initially grouped into 50 clusters, and subsequently assigned to one of the five main classes based on field data and knowledge of the region. Some manual editing of the classified scenes was also required. The Ruropolis scene was acquired on 30 July 2001. The two Ariquemes scenes were acquired about a year apart, 28 June 2000 and 02 August 2001. In the Ariquemes area, we are able to disaggregate the *secondary vegetation* in 2001 into two additional classes by overlaying the 2000 land cover data: (1) *secondary vegetation older than one year* and (2) *secondary vegetation younger than one year* (also referred to as "dirty pasture"). This disaggregation is not based on an existing biogeographical scheme, rather is intended to allow us to test the ability of the Terra data to resolve differences in secondary age using a single image.

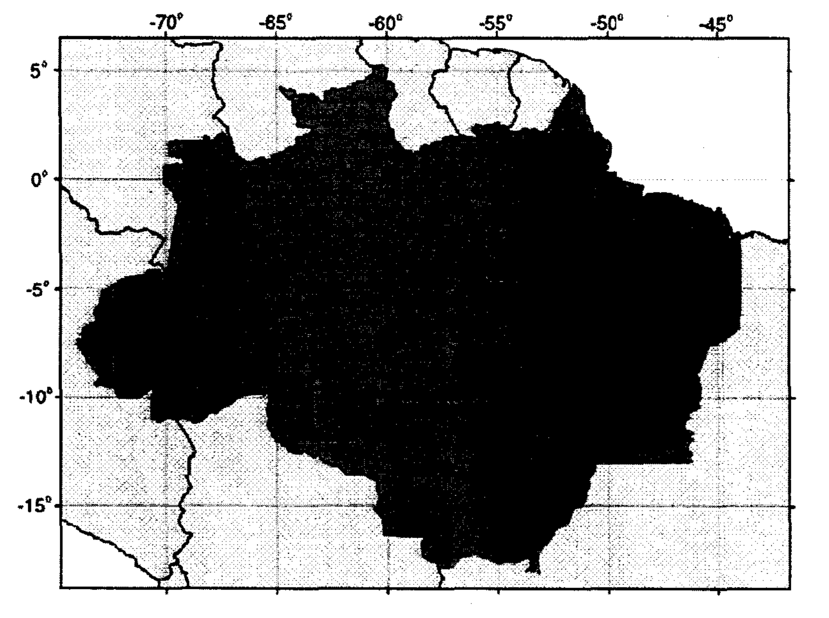

Figure 4.1. The Brazilian Amazon region, and two sub-regions used in this study (rectangles). Each sub-region is defined by separate Landsat ETM+ scenes and is approximately 10000 km^2 in size: (1) near the city of Ruropolis in the State of Para; and (2) near the city of Ariquemes in the state of Rondonia. Both areas are undergoing significant conversion of natural forest land for agricultural use, but have somewhat different climate, soils, and land use histories. The dark shaded area is the "Legal Amazon", the portion of Amazonia in Brazil. Dark lines are national boundaries, and light lines are Brazilian state boundaries.

We acquired 2001 MISR data (L1B2 Terrain Data for Ariquemes and Ruropolis; L2 Land Surface Data for Ruropolis) over the same areas and from the same orbital paths as the 2001 ETM+ acquisitions. The MISR instrument images the Earth in four spectral bands [blue (centered at 446 nm), green (558 nm), red (672 nm), and near infrared (867 nm)] and from nine angles (±70.5°, ±60.0°, ±45.6°, ±26.1°, and 0° from nadir). The MISR L1B2 data are top-of- atmosphere, terrain corrected reflectance. This data set is atmospherically corrected using parameters derived from 17.2 km blocks of data to create the MISR L2 data set. This use of discrete 16 x 16 blocks of pixels occasionally causes a quilted or patchy effect, which we minimize by interpolating the difference between corrected and uncorrected data to the 1.1 km pixel level. The MISR atmospheric correction routine is performed only if data are collected in all bands and cameras. Occasionally, data gaps in one camera or band prohibit atmospheric corrections and thus production of level two data. This is the case for the Ariquemes site.

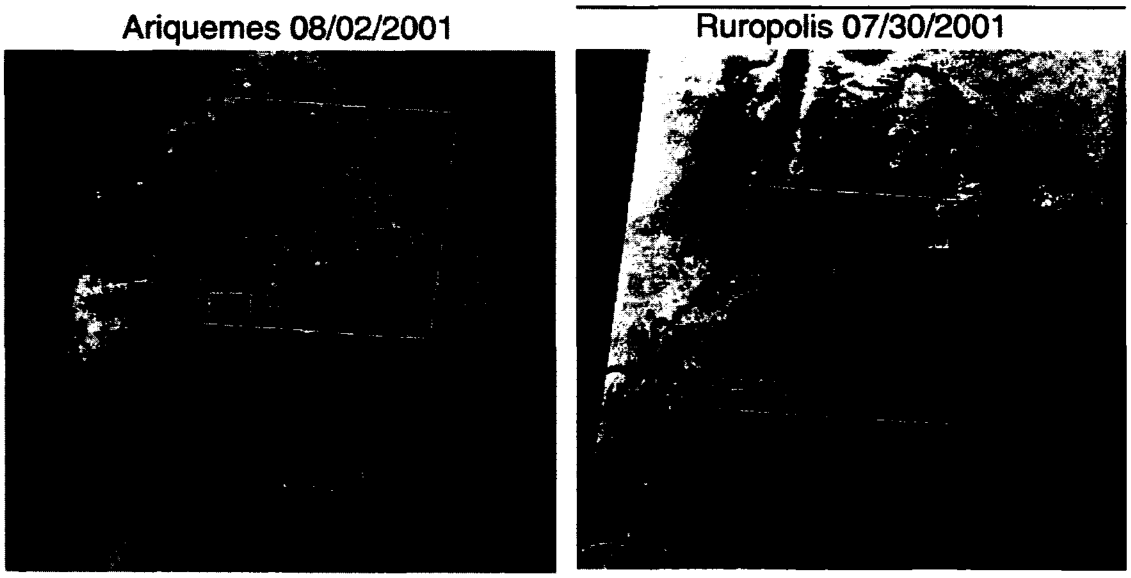

Figure 4.2. A view of the two study areas provided by a MISR false color composite (NIR, red, and green reflectance bands from the nadir camera). We used all nine angles and four spectral bands of this 1-km resolution data, combined with reflectances from MODIS, to infer subpixel patterns of land cover. The area covered by the ETM+ data is shown in yellow. All data used in this exercise are from July and August of 2001.

We wished to use the multiple reflectance values associated with the nine nadir and off-nadir cameras of MISR as statistical independent variables in a set of scaling analyses. Therefore, it is an important assumption that view angle be the only source of variability in data associated with the camera geometries. To help satisfy this assumption, we adjusted the surface reflectance values for cross-track effects using a simple radiative transfer model according to the method of Rojean et al. (1999). We also created an extended cloud mask using thresholded surface reflectance values together with the MISR Stereo Cloud product.

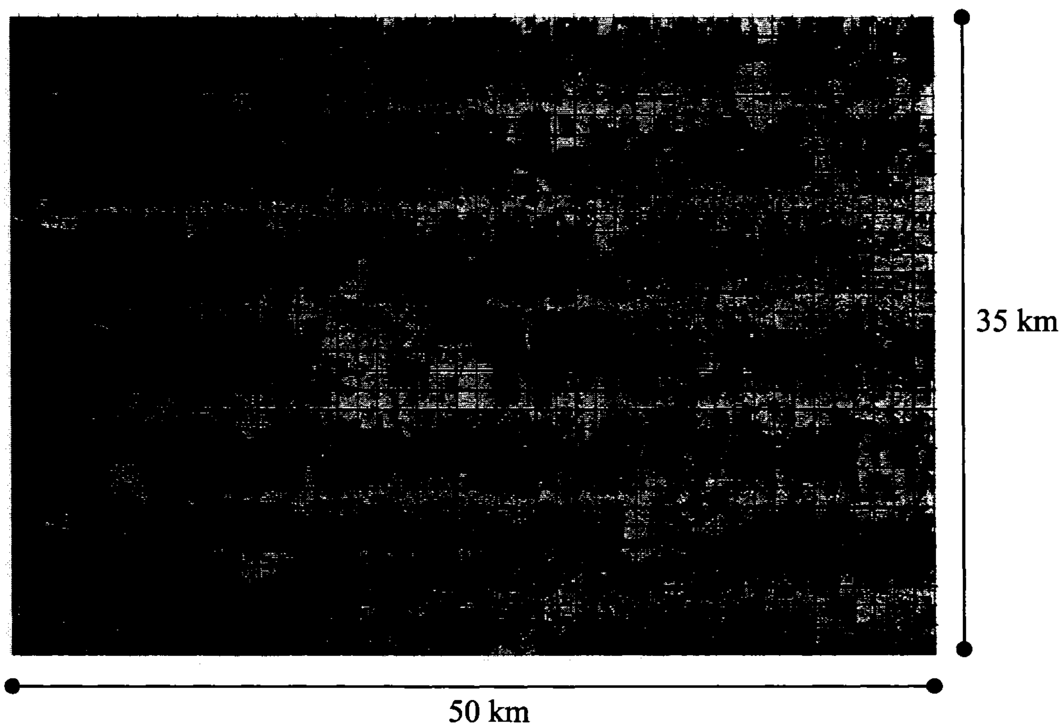

Figure 4.3. The 30 meter ETM+ data were classified and aggregated to 1.1 km to be used as training data for the MISR and MODIS reflectances. The black grid lines indicate the coarsened resolution. Within each 1.1 km cell, the fractional area of each class is calculated and assigned to a new data layer. For our reference case, three classes are used: forest (green), cleared land (tan), and secondary vegetation (red and blue). We also attempt to estimate fractional coverage of two secondary vegetation age classes: (red) less than one year since abandonment; and (blue) greater than or equal to one year since abandonment.

CASE	A	B	C	D	E	F	G	H	I	J	K
Estimation method	B-ANN	LU	B-ANN	B-ANN	B-ANN	B-ANN	B-ANN	B-ANN	B-ANN	B-ANN	B-ANN
Instrument	MISR	MISR	MISR	MISR & MODIS	MODIS	MODIS	MISR	MISR	MISR	MISR	MISR
Spectral bands	all	all	All	all & swir	Vis+nir+ swir	vis+nir	all	all	all	all	all
Angular bands	all	all	Nadir	all	nadir	nadir	all	all	all	all	all
Training site	Rurop.	Rurop.	Rurop.	Rurop.	Rurop.	Rurop.	Rurop.	Ariq.	Ariq.	Ariq.	Rurop.
Testing site	Rurop.	Rurop.	Rurop.	Rurop.	Rurop.	Rurop.	Rurop.	Ariq.	Ariq.	Rurop.	Ariq.
Atmospheric correction	Yes	Yes	Yes	Yes	Yes	Yes	No	No	No	No	No
Disaggregation	No	No	No	No	No	No	No	Yes	No	No	No
ANALYSIS											
1. Estimation method	X	X									
2. View angles	X		X								
3. Spectral bands	X			X	X	X					
4. Atmospheric correction	X						X				
5. Secondary disaggregation								X	X		
6. Spatial extrapolation							X		X	X	X
RESULTS											
Forest rmse	0.10	0.27	0.14	0.09	0.14	0.15	0.11	0.06	0.06	0.13	0.13
Cleared rmse	0.07	0.20	0.09	0.07	0.09	0.09	0.07	0.05	0.05	0.09	0.11
Secondary rmse	0.06	0.16	0.08	0.06	0.08	0.08	0.06		0.03	0.07	0.04
Young secondary rmse								0.03			
Old secondary rmse								0.04			
Forest r^2	0.78	0.44	0.59	0.80	0.57	0.55	0.73	0.91	0.91	0.62	0.67
Cleared r^2	0.72	0.43	0.56	0.74	0.57	0.54	0.76	0.93	0.93	0.58	0.66
Secondary r^2	0.63	0.33	0.46	0.61	0.35	0.35	0.64		0.52	0.47	0.28
Young secondary r^2								0.34			
Old secondary r^2								0.40			

LU: linear unmixing, B-ANN: Bayesian artificial neural network; mir: mid-infrared; vis: visible; nir: near-infrared; Rurop.: Ruropolis; Ariq.: Ariquemes; rmse: root mean square error; std. err.: standard error

Table 4.1. The results of our analysis, performing land cover fraction estimation at two sites and under various condition

MISR radiance data are acquired at a spatial resolution of 275 m, but due to limits on data transmission rates, the data for most bands are degraded onboard to a lower ("global mode") resolution of 1100 m. The higher resolution is preserved for the red band and nadir view reflectances. For those 12 data layers, we averaged the 275 m data to 1100 m, and retained the standard deviation for each of the 275 m pixels (16 observations per 1100 km) as textural data layers.

The MISR data are distributed in the Space Oblique Mercator (SOM) projection, and the geographic coordinates of each pixel center point is included in the data set. Using these values, we coregistered the ETM+ data, calculating the land cover fraction associated with each 1100 m grouping of ETM+ land cover. This is an approximation due to the non-rectangular nature of pixel point spread functions (Fisher, 1997), but we assume this is not a serious problem if the land cover mixtures are relatively spatially coherent (e.g., Braswell et al., 1996).

We used the nadir-corrected MODIS 16-day composite data set (MOD43) from NASA (Wanner et al., 1997). MODIS observes reflectance in seven spectral bands [blue (0.46 0.48μm), green (0.55 0.57 μm), red (0.62 0.67 μm), near infrared (0.84 0.88μm) and shortwave-infrared (1.23 1.25 μm, 1.63 1.65 μm, and 2.11 2.16 μm)] at a resolution of approximately 1000 m. MODIS data are collected in large 2330 km swaths, resulting in single view angles as large as 50 degrees off nadir. Reflectance artifacts associated with sun sensor geometry have been minimized in this data set by normalization of each observation to nadir view angles using the radiative transfer model of Li & Strahler

(1992). We reprojected the MODIS data to the 1.1 km resolution Space Oblique Mercator grid of MISR, using nearest-neighbor resampling. A common SOM grid was chosen for convenience, because of the availability of a reliable reprojection tool optimized for the MODIS data sets (USGS EROS Data Center, 2002).

We selected a spatial subset of pixels from each of the two study areas that was: (a) mostly water-free (< 10% water), (b) cloud-free in ETM+, MODIS, and MISR, and (c) of highest quality according to the MISR and MODIS ancillary data (e.g., Figure 4.4). We also required that all the data selected for training and testing of the procedure contain mixtures of vegetation classes. This effectively reduced data volume and increased the efficiency of our analyses by excluding a number of 100% *forested* 1.1 km pixels. Note that there were no 100% *secondary* pixels or 100% *cleared* pixels in either of these areas.

4.3.2 Analytical approach

We performed a multivariate analysis to investigate the relative accuracy of two sub-pixel land cover estimation approaches, using data from two instruments (Table 4.1). The 11 cases enabled investigation of six issues that are listed in the Analysis group of Table 1 and discussed in this Section. For most cases, an optimal subset of the independent variables was selected that best estimates each land cover fraction through application of a stepwise regression procedure (Chaterjee & Price, 1991). Two of the cases (Case C and Case D) required the bands to be pre-selected without the stepwise regression routine. We evaluated the accuracy associated with methodology and with independent variable using two elementary statistical measures: coefficient of correlation (R^2) and root mean squared error (RMSE).

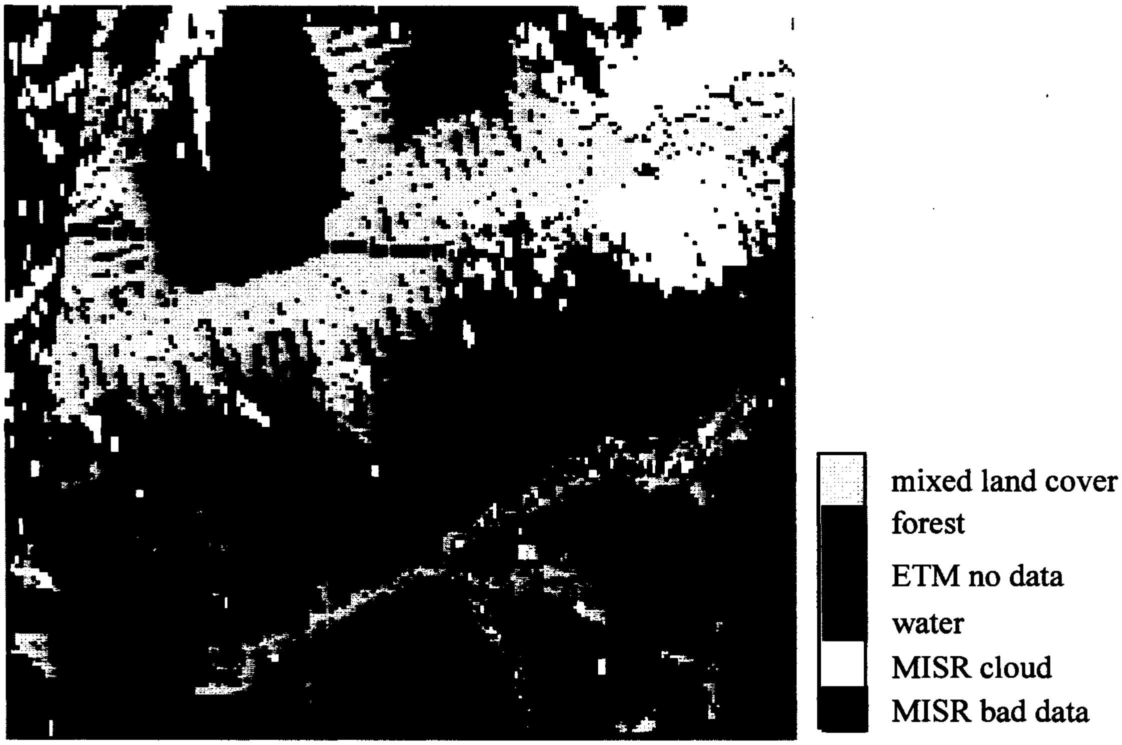

Figure 4.4. We superimposed a mask of all areas that contained (1) no mixed 1.1 km pixels, (2) clouds, (3) water, or (4) bad data, based on inspection of all data sets (compare with Figure 4.2b). Clearing and secondary areas always covered less than 100% of a MISR/MODIS pixel, so the areas in green are undisturbed forest areas. We assume that traditional pixel-based clustering algorithms are able to separate homogeneous forest areas from mixed areas prior to an unmixing analysis like those presented in this paper.

Our first case comparison involves sub-pixel estimation methods (*Analysis 1 in Table 4.1*). We compared two mathematical techniques for estimating sub-pixel land cover fraction: linear unmixing and artificial neural networks. In linear unmixing (LU), each land cover class is assumed to have a unique spectral signature, or endmember reflectance. Given data from N pixels and M bands, the observed reflectance is assumed to be a linear superposition of the reflectance from each of the C subpixel endmember classes.

$$\mathbf{R} = \mathbf{E} \cdot \mathbf{F}, \tag{4.1}$$

where $\mathbf{R}$ is an MxN matrix of measured reflectance, $\mathbf{E}$ is an MxC matrix of end-member reflectance and $\mathbf{F}$ is a CxN matrix of land cover fractions. Using a library of endmember reflectance ($\mathbf{E}$), one can solve for F by inverting Equation 4.1 for each pixel n, solving for the fractions $\mathbf{f}_n$ within that pixel:

$$\mathbf{r}_n = \mathbf{E} \cdot \mathbf{f}_n, \tag{4.2}$$

where $\mathbf{r}_n$ is an Mx1 array of measured reflectances for pixel n, and $\mathbf{E}$ is an MxC matrix of end-member reflectances. In solving for the land cover fractions within each pixel, there are M equations and C unknowns. Therefore, to find a unique solution, we will need at least as many bands as land cover types.

The matrix of end-member reflectances $\mathbf{E}$ is typically assembled using field observations of reflectance, or by identifying a sample of pure pixels in the scene for each cover type. Alternatively, when pure pixels are not available, endmember signatures can be estimated by inversion of Equation 4.1 with a set of training data (Oleson et al., 1995) (Section 4.3.3). For each band, mean endmember reflectance values $\mathbf{e}_m$ (1xC) are given by

$$\mathbf{r}_m = \mathbf{e}_m \cdot \mathbf{F}, \tag{4.3}$$

where $\mathbf{r}_m$ is a 1xN array of measurements from band m, and $\mathbf{F}$ is the CxN matrix of land cover fractions. In solving for the end-member reflectances, there are N equations and C unknowns. Using a data set of known land cover fractions (e.g., based on ETM+) in combination with observed reflectances in several bands (e.g., from MISR or MODIS), the unknown spectral signature for each land cover class can be estimated using this method. In this case, the problem is highly overdetermined because the number of bands is much smaller than the number of pixels.

Artificial neural network (ANN) approaches represent another set of tools for relating reflectance values to fractional land cover. In contrast to the inverse procedure of unmixing, the ANN is used to perform direct nonlinear regression using pairs of $\mathbf{r}_n$ and $\mathbf{f}_n$ values from observational and training data. The discussion of ANNs in this section follows the notation and logic of MacKay (1994) who pioneered the development of Bayesian ANNs in statistical analysis. An ANN can be thought of as consisting of a number of "layers", each having J "nodes". A node is a weighted sum of inputs followed by application of a prescribed function. The outputs of all nodes in a layer are collected into a new vector and fed into the next layer. Using a two-layer network, fractional cover estimation for each land cover class k is defined as

$$\hat{f}_k = g\left(\sum_{j=0}^{J}\left\{w_{kj}^{(2)}\tilde{g}\left(\sum_{i=0}^{M}\left\{w_{ji}^{(1)}r_i\right\}\right)\right\}\right), \tag{4.4}$$

where g is typically a linear function (e.g., $g(a)=a$), $\tilde{g}$ is a different function that is usually nonlinear (*e.g.*, tanh(a)), and M is the number of bands. The two matrices $\mathbf{w}^{(1)}$ and $\mathbf{w}^{(2)}$ represent the free parameters in the regression and include bias terms for j=0 and i=0. In this formulation we reference the elements of r_n and f_n and drop the subscript n for convenience.

The function in Equation 4.4 is referred to as a network because all inputs can influence all outputs, depending upon the values of the weights. Determining the network architecture (*e.g.*, choosing a value for J) and using the available data to estimate weights and biases are the basic problems of ANN theory. There is a very large amount of literature on this subject and we use one of the most elementary network types. For parameter estimation we use the standard backpropagation algorithm, which updates the weights and biases $\mathbf{w}$ for each pair of data vectors $\mathbf{r}$ and $\mathbf{f}$, given a prediction $\hat{\mathbf{f}}$, in order to minimize the error

$$E(\mathbf{w}) = \sum_{k=1}^{c} (\hat{f}_k(\mathbf{w}) - f_k)^2 \tag{4.5}$$

by estimating the derivative of E with respect to $\mathbf{w}$ (using Equation 4.1).

Foody et al. (1997) previously used an ANN to map proportions of different land cover classes in an area of the Brazilian Amazon region. Our approach differs in one major respect: we avoid issues related to model overfitting by including a regularization term in the cost function (MacKay, 1994; Bishop, 1995). This Bayesian modification of artificial neural networks (B-ANN) effectively limits model complexity to that which is evidenced in the data itself. In the Bayesian framework, model parameters are treated as probability distributions, and the posterior probability of the network weights given the set of observed outputs $D \equiv \mathbf{f}_n;\ (n = 1,\ldots,N)$ is:

$$p(\mathbf{w} \mid D) = \frac{p(D \mid \mathbf{w})p(\mathbf{w})}{p(D)} \tag{4.6}$$

where $p(D|\mathbf{w})$ is the probability of the observations given a choice of weights (the likelihood), $p(\mathbf{w})$ is a prior distribution of weight values, and the denominator is a normalization constant. Assuming Gaussian distributions for both the likelihood and the prior, the posterior distribution is given by

$$p(\mathbf{w} \mid D) = \frac{1}{Z_S}\exp(-\beta E_D - \alpha E_w) = \frac{1}{Z_S}\exp(-S(\mathbf{w})) \tag{4.7}$$

where Z_S is a constant and S can be written as:

$$S = \beta\sum_{n=1}^{N}\sum_{k=1}^{C}(\hat{f}_k^{(n)}(w) - f_k^{(n)})^2 + \alpha\sum_{i=1}^{W} w_i^2 \tag{4.8}$$

The parameters α and β represent the variance of the weights and the noise in the data, respectively. Thus, maximizing the posterior probability with respect to $\mathbf{w}$, or equivalently by minimizing the negative log of the probability S, yields a solution to the problem. This amounts to minimizing the modified error function of Equation 4.8 (compare with Equation 4.5).

4.3.3 Experimental design

We tested the accuracy of our land cover fraction estimates under various conditions, using different input data, and both modeling techniques. The objective of the 11 cases, shown in Table 4.1, was to evaluate the dependence of results to a number of factors relative to a base case. The base case (A) refers to the within-scene retrieval using the B-ANN regression method and all available MISR bands (wavelength and angle) in the Ruropolis area. The following sections describe the six questions addressed by the results of the various cases.

Estimation method. Land cover fractions from linear unmixing (Case B) were compared with results of the nonlinear regression for the base case (A), both in the Ruropolis area. The spectral-directional endmembers (Figure 4.5) for the linear unmixing were derived from the ETM-derived fractions and the MISR reflectances by inversion of Equation 4.3 using a constrained gradient-based optimization procedure.

View angles. We investigated the potential for multiple view angles to improve the estimation of land cover class fractions by comparing two estimates for the Ruropolis area: using all the available MISR data (Case A), and using only the four MISR nadir bands (visible-NIR) (Case C).

Spectral bands. We examined the importance of wavelength dependence relative to angular dependence, and in particular the usefulness of SWIR bands from MODIS for modeling land cover fractions. This exercise involved four configurations of the available data: MISR nadir bands, visible to near-infrared (Case A), MODIS visible and near infrared bands (Case D), MODIS visible, near infrared, and middle infrared bands (Case E), and the combination of MISR bands and MODIS middle infrared bands (Case F).

Atmospheric correction. Tropical atmospheres present numerous challenges to atmospheric correction. To examine the effect of unavailable or poor atmospheric correction on subpixel land cover estimation accuracy, we estimate fractional land cover using Ruropolis data with atmospheric correction (MISR L2) (Case A) and the same Ruropolis data set without atmospheric correction (MISR L1B) (Case G).

Secondary vegetation age class. We examined the potential for resolving a greater level of detail in our land cover classification. Using classified ETM data from the previous year (available for Ariquemes), we were able to disaggregate the *secondary vegetation* class into two sub-classes: greater than one year, and less than one year since abandonment. We then used the neural network regression to estimate land cover fractions in the Ariquemes area with one secondary class (Case H) and with two secondary classes (Case I).

Spatial extrapolation. For operational mapping of land cover across the entire Brazilian Amazon region, an appropriate number of training sites would be selected that samples the variability of the desired land cover types. For Ruropolis (Case G) and Ariquemes (Case I), we selected 50% of the valid data at random for training, and withheld the rest for testing. In order to evaluate our ability to extrapolate, we trained the model at each study site and tested the model at the other (Cases J and K). Since MISR data for Ariquemes were not atmospherically corrected (L1B), we also used uncorrected MISR data (L1B) for Ruropolis.

Whole pixel vs. sub-pixel classification. Finally, we examined the importance of small scale heterogeneity in this study by examining the Ruropolis ETM+ based fractional data, relative to our base case estimates, in two ways. First, we calculated the actual area in each class at the Landsat scene level (about 180x180 km) using the fractional land cover data. Then we assigned each 1.1 km pixel into a single class based on the dominant land cover class, and recalculated the total area in each land cover class for the entire scene. We also examined the estimation results from Case A, comparing the predicted area in each class using the sub-pixel estimation results to the actual area in each class.

4.4 Results and discussion

The results of the 11 cases reveal a large range in ability to estimate sub pixel land cover fractions (Table 4.1; note that the following section numbers correspond to the Analysis section numbers in Table 4.1). The sub-pixel fraction estimates for our base case (Case A; using the B-ANN, and trained and tested in Ruropolis) show good reproduction of spatial land cover distribution patterns. However, some overestimates of secondary vegetation, and corresponding underestimates of forest, are evident throughout the scene. A view of the area around the city of Ruropolis reveals the details (Figure 4.6). The model accurately predicts the heavy concentration of cleared area directly along the roads, as well as the large secondary vegetation patch south of the intersection of two main roads. Estimation error is distributed approximately randomly throughout the area of concentrated land use along the Trans-Amazon Highway.

Overall, the predicted spatial patterns of the *forest* and *cleared* classes are consistently better than results for the *secondary* class, as captured by explained variance (R^2). The *secondary vegetation* class encompasses the greatest variation in vegetation structure and in foliar properties associated with successional stage. This class also represents the least total land area in both scenes (Table 4.2).

4.4.1 Sub-pixel estimation method

Non-linear regression using Bayesian artificial neural networks (B-ANN) (Case A) was considerably more successful than linear unmixing (LU) (Case B) at estimating sub-pixel land cover fraction near Ruropolis (Table 4.1). For all three land cover types, the root mean squared error (RMSE) associated with the B-ANN results was less than half that for the LU-derived fractions. The correlation coefficients (R^2) for both techniques were significant, but the B-ANN allowed a better fit to the data, for all land cover classes in these two cases.

4.4.2 Multiple vs. single view angles

The results from the linear estimation of endmember signatures using Equation 4.3 showed that each vegetation class has a more or less unique spectral-bidirectional signature (Figure 4.5). These signatures show dependence on both wavelength and camera view angle, with the strongest angular variation occurring in the NIR bands. Lower error and better model fit diagnostics were obtained by using all possible MISR bands (Case A) as opposed to using only the nadir camera MISR bands (Case C). The B-ANN regression method was used in both cases.

4.4.3 Visible and NIR vs. Visible, NIR, and SWIR

We observed a slight improvement in estimation of sub-pixel fraction when incorporating the MODIS SWIR bands (Case F) into the possible set of variables, compared to the base case with visible and NIR reflectance and all angles from MISR (Case A). For the Ruropolis region, MISR performed slightly better than MODIS in a head-to-head comparison (Cases A and E). In another analysis, using the four visible and near infrared spectral bands from MODIS and the MISR nadir view (Cases C and D, respectively), we see little difference. Previous tropical vegetation remote sensing studies have shown that SWIR reflectance is sensitive to canopy water content and gap fraction, and is potentially useful for detecting changes associated with forest regeneration (e.g., Lucas et al., 2002). For the broadly defined classes in this study, this sensitivity apparently leads to large within-class variability in reflectance and lower than expected ability to resolve distributions of class mixtures.

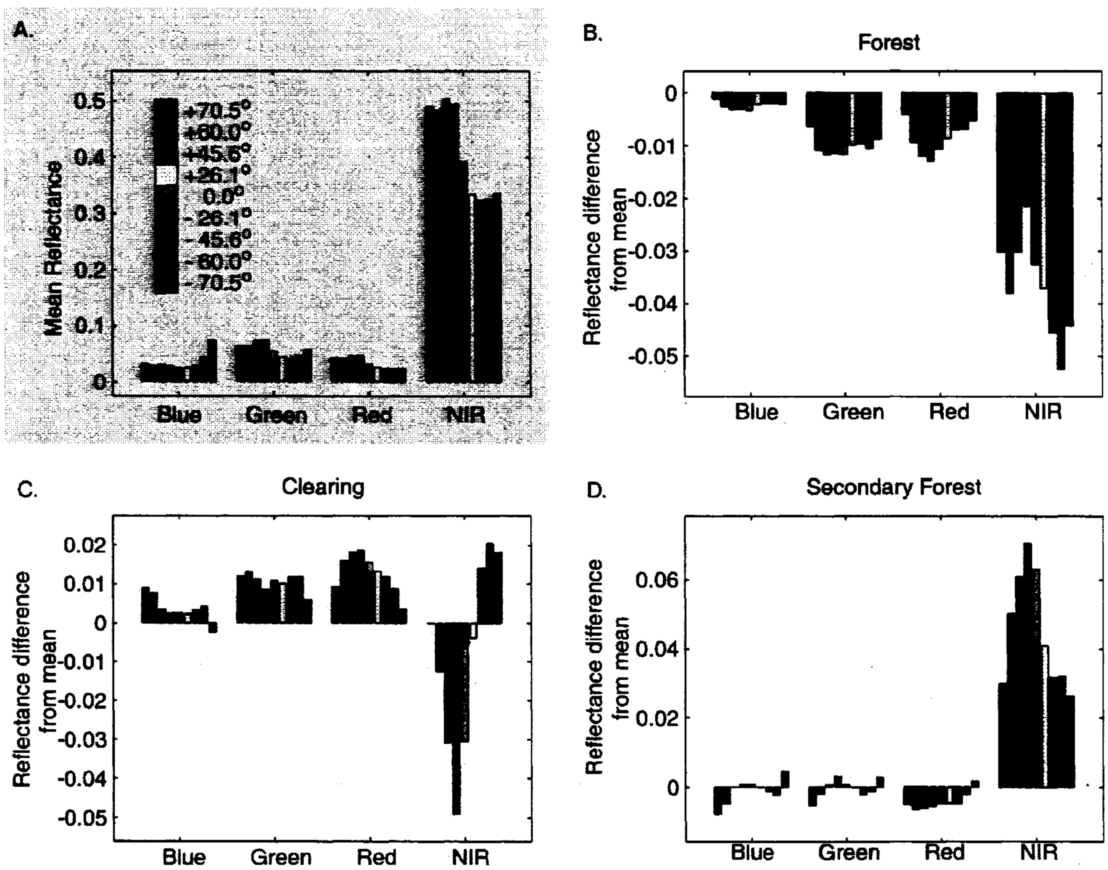

Figure 4.5. (a) Mean reflectance in all MISR bands and nominal view angles for the Ruropolis study area. (b-d) Angular-spectral endmembers for the three main land cover classes, estimated by assuming linear mixing across the entire Ruropolis study area. These values are estimated by inverting the mixture equation (Equation 4.3) for the endmember reflectance, one band at a time, using all the reflectance data R and all the fraction data F for the scene. The endmembers are presented as differences from the mean reflectance profile.

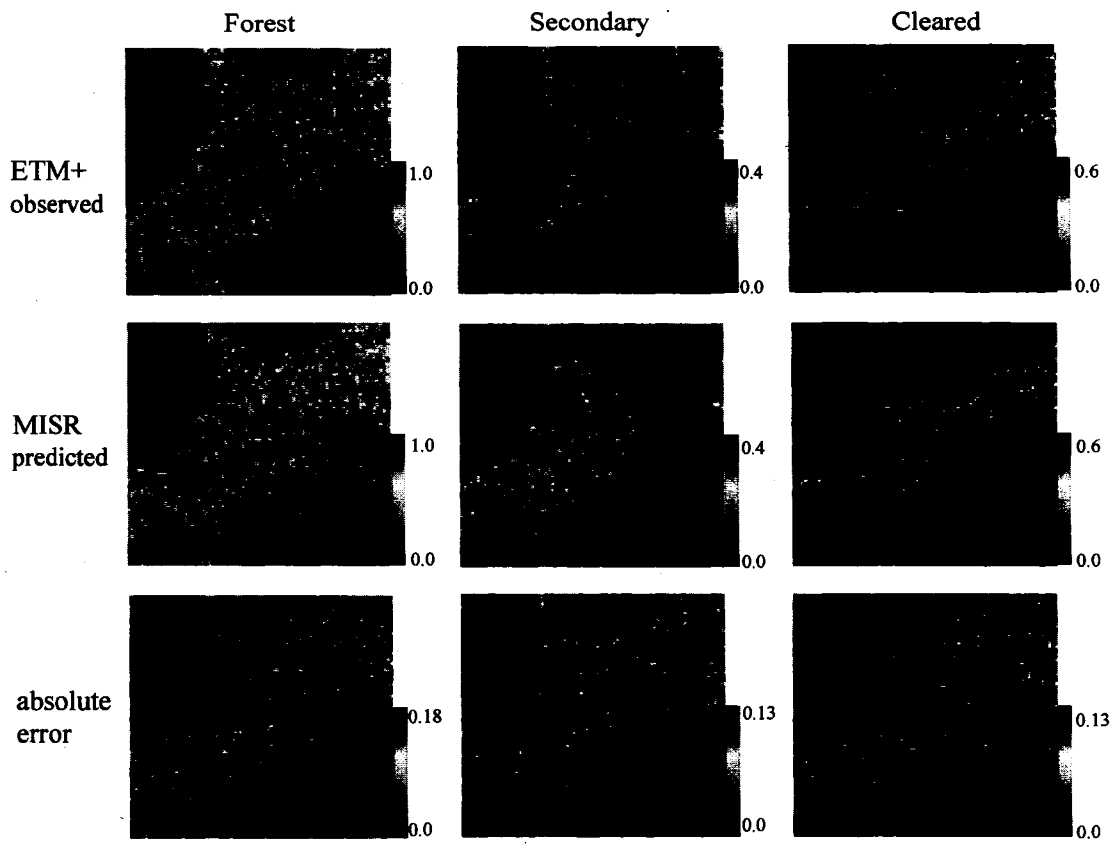

Figure 4.6. Observed and predicted values of forest, secondary, and cleared fractional areas for the reference case in Ruropolis (Case A, Table 4.1). Note the differences in scale associated with natural distributions of these classes within 1.1 km pixels. Grey areas are pixels with missing ETM+ or MISR data. This is close-up of an approximately 80 km square area around the city of Ruropolis (broader region shown in Figure 4.2b), revealing good representation of spatial patterns for the fractions, especially edge effects, and very little spatial structure in the residuals of the estimation (bottom three panels).

Ruropolis scene-level landcover area km^2

landcover	ETM+ observed		MISR predicted
	fractional pixel	whole pixel	fractional pixel
forest	24,561	25,206	24,157
cleared	1,029	870	1,038
secondary	799	318	1,041

Table 4.2. Observed and predicted regional estimates of total area in a given class for the Ruropolis scene, based on using the subpixel fractions and, for the observed data set, assigning the pixel to 100% of the dominant class.

4.4.4 Atmospheric correction

Despite obvious atmospheric effects in both data sets, our results using MISR were not sensitive to atmospheric correction. The estimation results from the Ruropolis data set with atmospheric correction (Case A) were not very different from the results using the same Ruropolis observations with no atmospheric correction applied (Case G). Based on the weighting of the bands in the regressions, we suggest that the availability of blue and green visible bands in the analysis allowed for an automatic adjustment for atmospheric optical depth, similar to that employed in the widely used enhanced vegetation index (EVI) (Huete et al., 1997).

4.4.5 Secondary vegetation age class discrimination

In Ariquemes, we were able to test the ability of the model to discriminate between two age classes of secondary vegetation (Cases H and I). The results from these two cases were similar for forest and pasture fractions, but with lower accuracy for the disaggregated secondary vegetation classes. The model only captured about one third of the variance (R^2 of 0.34 and 0.40) in the two secondary age classes. Despite the poorer model fit, RMSE values were relatively unaffected relative to the case of a single secondary class. This result is encouraging, given the potentially subtle radiometric differences associated with different aged stands, and the fact that several other land cover transitions could give rise to both sub-classes. For example, a one year old secondary pixel could have contained pasture or forest (rapidly cleared and abandoned) in the previous year.

4.4.6 Spatial extrapolation

The comparison of the results obtained from training and testing in Ruropolis (Case F) to the results from training in Ariquemes and testing in Ruropolis (Case I) show somewhat poorer results for the spatial extrapolation. The comparison of the results obtained from the training and testing in Ariquemes (Case H) to the results from the model trained in Ruropolis and tested in Ariquemes (Case J) also show reduced accuracy in estimating sub-pixel land cover fraction due to extrapolation. Despite the degraded results, this exercise demonstrates that the B-ANN approach combined with MISR data creates a model general enough to extrapolate results to new areas. These results give us an indication of some of the difficulties introduced by extrapolating a model that is trained in a location with different land cover distributions, vegetation structure, topographic conditions, atmospheric conditions, and angular effects, among other difference. Also, inconsistencies in manual editing of ETM+ classifications contributed to the error.

4.4.7 Whole pixel vs. sub-pixel classification

Our examination of small-scale heterogeneity effects on estimates of total land cover area illustrates the fact that whole pixel classification can result in a significant underestimation of non-dominant classes (e.g., *cleared* and *secondary*), and an overestimation of the dominant class (e.g., *forest*) (Table 4.2). The results also show that sub-pixel fractional estimates using MISR result in good agreement in total area for each type at the scene level. Totals of predicted forest and cleared areas are each accurate to within 2% of observed values, and total secondary area is 26% greater than observed area. This relatively large error is not surprising given the highly fragmented and broadly defined nature of this class, but it compares quite favorably to the 43% under-prediction that would result from using an ideal whole pixel classification (Table 4.2) based on known dominant fractions.

4.5 Conclusions

The results presented in previous sections suggest that nonlinear regression offers significant improvement relative to linear unmixing for estimation of sub-pixel land cover fractions in the heterogeneous disturbed areas of Brazilian Amazonia. This improvement is likely due to the fact that linear unmixing assumes the existence of pure sub-pixel classes with fixed reflectance signatures (endmembers). In this application, two of the land cover classes (*cleared land* and *secondary vegetation*) are comprised of areas with very different biophysical characteristics. Thus, the endmembers are relatively poorly resolved despite our ability to manually assign ETM+ pixels to these classes. The B-ANN approach estimates nonlinear relationships between each land cover fraction and reflectances, without making assumptions about the physics of sub-pixel mixing. With respect to the observed cross-validation accuracy, the neural network formulation we used included a Bayesian regularization term, and is therefore designed to generalize well.

Both moderate resolution Terra data sets (MODIS and MISR) provide similar information for resolution of land cover types in this study, though MISR does marginally better. Results using the merged data (MISR plus MODIS SWIR) suggest potential synergistic gains in accuracy, which warrants evaluation in future studies. Comparison of the full set of regression results suggests that discrimination of diverse land cover types is aided by both angular and spectral information, and that the critical independent variables may be different for different types. In general, we conclude that multivariate approaches that utilize a large number of bands and view angles allow for the selection of the critical independent variables for a given application.

It is important to evaluate potential extrapolation errors for a procedure that ultimately would be used for large-scale analysis. In this preliminary study, RMSE increased from the base case by 18% to 100% depending on location and land cover type. These results are encouraging, given that only two sites were used, and that they are over 700 kilometers apart. Future analyses will incorporate a denser sampling of ETM sites for training and testing. We were not able to explore the interaction between atmospheric correction effects and extrapolation error due to limitations in data availability for our study sites, but expect differences in atmospheric optical depth to be a primary source of extrapolation error. On the other hand, the selection of blue bands in the cross-validation regressions suggests that the statistical models exhibit some degree of self-correction.

Quantitative interpretation of satellite data at the pixel level is potentially confounded by errors in registration as well as from adjacency effects (Fisher, 1997, Townshend et al., 2000). Spatial averaging can minimize these problems (e.g., Hagen et al. 2002), trading off resolution for overall accuracy. Therefore, the fractional cover estimates in this study represent an extreme test of the data and methods. Evaluation of estimated total class areas for the entire scene (Table 4.2) supports this notion. The size of an ETM scene (~10,000 km^2) is comparable to, or smaller than most global climate model grid cells. In fact, many modeling applications that utilize land cover information could tolerate some degree of spatial degradation in exchange for improved estimates of energy, moisture, and carbon exchange.

Multiangle observations from MISR are relatively untested in terrestrial applications, and in this study they provided significant resolving power for estimation of sub-pixel vegetation fractions. There are theoretical and empirical reasons to expect the view angle dependence of land surface reflectance to be governed by variations in canopy structure, and though some satellite studies exist, the full potential of multiangle remote sensing for ecological studies using global scale satellite data is not known. In this study we have taken an additional step toward broad exploitation of multiple view angle remote sensing in terrestrial research.

CHAPTER 5

STATISTICAL UNCERTAINTY OF EDDY FLUX BASED ESTIMATES OF GROSS ECOSYSTEM CARBON EXCHANGE AT HOWLAND FOREST, MAINE[4]

5.1 Introduction

Efforts to accurately predict patterns of carbon dioxide exchange between terrestrial ecosystems and the atmosphere are currently limited by our ability to represent the relevant biogeochemical processes in unifying models, which typically parameterize fluxes as a function of environmental variables. Models of the global carbon cycle need to accurately capture the dynamics of terrestrial biosphere-atmosphere exchange at a range of time scales, because forcings and responses occur across a broad temporal spectrum, from seconds (e.g., light capture by leaves) to years (e.g., community dynamics). Field biometric studies have historically been used to validate model predictions at long time scales, and evaluation of the rapid ecophysiological mechanisms

---

[4] This chapter is based on and contains material from a paper published in 2006:
Hagen, S.C., B.H. Braswell, E. Linder, S. Frolking, A.D. Richardson, and D.Y. Hollinger (2006) Statistical uncertainty of eddy flux-based estimates of gross ecosystem carbon exchange at Howland Forest, Maine. *Journal of Geophysical Research-Atmospheres*, (111): D08S03, doi:10.1029/2005JD006154. Reproduced by permission of American Geophysical Union.

has been limited to important, but temporally sparse, leaf and soil chamber measurements.

In the past decade, at several hundred locations around the world, eddy flux tower measurement programs have been established to quantify ecosystem-atmosphere CO_2 exchange with high frequency, near-continuous, multi-year measurements. These net ecosystem exchange (NEE) measurements provide another data source for ecosystem model evaluation. One primary advantage of using eddy flux data for process studies and model evaluation is the continuity of the measurements, with time intervals typically 0.5-1 hour. Many time series are now between 5 and 15 years in duration (e.g., Harvard Forest, Wofsy et al., 1993; Walker Branch Watershed, Balddocchi & Vogel, 1996; Howland Forest, Hollinger et al., 2004). Another advantage is that the measurements are associated with a growing and coordinated effort (e.g., AmeriFlux) to establish networks of towers that span a range of ecosystem types and environmental conditions. Also, eddy flux sites tend to be foci for a suite of other measurements including meteorological variables, biometry, and other types of flux measurements. The primary disadvantage, with respect to understanding terrestrial biogeochemistry, is that measurements of eddy flux do not themselves directly quantify specific ecosystem processes but rather the net result of several processes. Of secondary concern are occasional instrument failures and other normal data collection gaps and errors.

Net ecosystem exchange observations record the typically small imbalances between the gross component fluxes of ecosystem respiration and photosynthesis (Wofsy et al., 1993), and while NEE data can be compared to model predictions, it is often more desirable to validate modeled component fluxes independently. The gross fluxes individually reflect distinct sets of processes whose mechanisms might influence one another but are largely separable. The net flux does not constrain the overall dynamics as well as the component fluxes because the net flux could be mistakenly modeled by gross fluxes having large compensating errors. Furthermore, some models, for example those driven by remote sensing observations, focus on uptake by photosynthesis, also known as gross ecosystem exchange (GEE), with little or no attempt to predict respiration (e.g. Prince & Goward, 1995, Xiao et al., 2004). Models such as these require independent GEE estimates for validation, and eddy flux observations of NEE can be useful in estimating these independent GEE data sets.

In principle, the eddy flux data, along with associated meteorological drivers (e.g. temperature, solar radiation, humidity) contain enough information that will allow separation of the net flux into its gross components (Goulden et al., 1996a), though there is currently no agreed upon approach for doing so, and the underlying uncertainties are not well quantified. The basis for this disaggregation is the fact that nighttime NEE reflects respiration processes only, and to the extent that respiration can be predicted during the day based on relationships with predictor variables at night, daytime GEE can be estimated essentially as the difference between NEE and modeled respiration. Thus, GEE estimates rely heavily on model predictions for large contiguous intervals (i.e. all daylight hours). Like any statistical inference, this process carries with it some prediction uncertainty that should be quantified in order to compare tower-based GEE with independent observations or model predictions.

An additional factor that must be considered in utilizing eddy flux data is the existence of missing data resulting from inevitable instrumental lapses. Also, periods of low atmospheric turbulence result in CO_2 flux measurements that are not representative of the actual ecosystem-atmosphere exchange, and these data typically are removed prior to analysis (Goulden et al., 1996b). Altogether, the resulting gaps can be extensive and non-randomly distributed in time. The implication for estimating GEE is that an additional model to fill daytime NEE gaps must be defined and parameterized, which adds some amount of quantifiable prediction uncertainty.

One possible framework for constructing a time series of ecosystem uptake (GEE), given the data and a choice of models, is

$$G = \left\{ \begin{array}{ll} 0 & \text{Night} \\ \hat{R} - F & \text{Day, No Gap} \\ \hat{R} - \hat{F} & \text{Day, Gap} \end{array} \right\}, \qquad (5.1)$$

where G is GEE, F is the observed net flux (NEE), and $\hat{R}$ and $\hat{F}$ are the modeled respiration and daytime NEE, respectively. Several previous studies have focused separately on issues related to "gap filling" (e.g. Falge *et al.*, 2001), i.e. defining and evaluating the model $\hat{F}$, as well as the general problems of disaggregating NEE into component fluxes, which has focused principally on choosing an appropriate regression model for $\hat{R}$ (e.g. Goulden et al., 1996a). More recently, however, data assimilation techniques have been used to both fill gaps in flux records and disaggregate NEE into component fluxes (Jarvis et al., 2004, Gove and Hollinger, 2006).

To most appropriately use eddy flux derived GEE for comparison with process models, satellite data, or other field observations, the statistical uncertainties associated with the inference of daytime respiration and NEE during gaps should be quantified so that error bars can be applied at any given choice of time scale. Commonly used statistical approaches for providing error bounds using analytical formulas, such as the formula used to estimate the prediction interval for least squares regression predictions, are not applicable to these data because the underlying assumptions of these approaches do not hold (Hollinger and Richardson, 2005). For example, eddy flux CO_2 data and the predictions obtained from regressions using these data have (1) non-constant variance, (2) non-independence of residuals, (3) non-Gaussian noise, and (4) potential sampling bias due to the non-random distribution of data gaps. Hollinger and Richardson (2005) conclude that the first three properties listed above result from a combination of the stochastic nature of turbulence, occasional large instrument errors, and the non-uniform occurrences of environmental driving conditions (e.g. over 24 hours, there are far more instances of zero solar radiation than higher values).

Monte Carlo based statistical techniques such as resampling with replacement ("bootstrapping") (Robert & Casella, 1999) provide a computational solution to the problem of estimating statistical uncertainty in nonlinear model predictions and data with complicating features such as severe heteroscedasticity. Previous studies have utilized *ad hoc* approaches inspired by bootstrapping to estimate uncertainties of net CO_2 exchange. Often, the technique is used to estimate uncertainty in a sum of flux estimates over time. The most common application includes the random simulation and filling of additional data gaps (Falge et al., 2001, Griffis et al., 2003). Another Monte-Carlo technique applied to net flux data involves modeling and repeatedly resampling residuals to estimate uncertainty (Saleska et al., 2003). Uncertainty due to gaps has also been estimated by creating seasonal populations of daily carbon balance that are randomly sampled for comparison with actual fluxes (Goulden et al., 1996b). Quantification of the measurement uncertainty in flux observations has recently been addressed (this includes defining a suitable probability density function and some measure of the variance) (e.g. Hollinger and Richardson, 2005). Following model parameter optimization using maximum likelihood techniques, random noise with the same statistical characteristics as the measurement uncertainty of the original data can be added back to the model output (Press et al., 1993). By using repeated simulation, as in a Monte Carlo approach, uncertainty limits can be estimated for model parameters, gap-filled values, or annual sums (e.g. Richardson and Hollinger, 2005).

In this paper, we present an example of statistical uncertainty estimation and error analysis for a GEE time series, based on eddy flux data from the Howland Forest in Howland, Maine, USA. Our analysis differs from previous work in several ways. First, we are focusing on gross ecosystem exchange, a component flux that reflects a distinct set of ecosystem processes, as opposed to ecosystem respiration or net flux. Second, we account for uncertainty due to model parameterization as well as the uncertainty associated with the random nature of the flux observations (earlier studies have focused on one or the other). We recognize that uncertainty in ecosystem flux arises from sources other than the statistical modeling, including different choices of friction velocity thresholds for filtering, variability in tower footprint, and changes in the system (i.e. insect infestations, large tree blow downs, etc.). In this analysis, we estimate patterns of uncertainty that are related only to statistical inference. Third, our method does not require the generation of additional gaps; and, therefore allows us to estimate statistical uncertainty at any time scale, from half-hour to multi-year. Lastly, we perform a sensitivity analysis of the uncertainty of half-hourly to annual GEE estimates using different modeling approaches and different statistical assumptions, in an attempt to understand the effect of model choice on the estimates. We examine and quantify the 90% prediction intervals for one site, but our discussion of the general implications of our results for the role of data and models in understanding ecosystem processes is not site specific.

5.2 Data

Howland Forest is an AmeriFlux research site located at 45.20°N and 68.74°W, about 35 miles north of Bangor, ME. The site is dominated by red spruce and eastern hemlock. The vegetation, soils, and climate of this site have been thoroughly described elsewhere (Hollinger et al., 1999). The main eddy-flux research tower has been operational since 1995.

We examined seven years of CO_2 flux data (NEE) measured half-hourly from 1996 through 2002 (Figure 5.1a). We screened out flux data with low friction velocity ($u^* \leq 0.25$ m s^{-1}; Hollinger et al., 2004). The friction velocity screening, primarily, and the occasional instrument failure, secondarily, combine to reduce the amount of available data. There are also other periods when data don't meet quality standards and are rejected. The resulting time series of NEE data contain available observations for 49% of all half-hour intervals (Figure 5.1b). To compute GEE for each of the 61,362 daytime half-hours in 1996-2002, we need to model all 61,362 (100%) respiration values and 24,295 (40%) missing daytime NEE values. The NEE time series is missing 39,382 (64%) nighttime observations. While the nighttime measurements are not used directly in the GEE estimates because we assume no photosynthesis occurs in the dark, the valid nighttime NEE observations are used fit the respiration model.

Half-hourly meteorological data (including air temperature, soil temperature, solar PPFD, and vapor pressure deficit) from the Howland tower were used as driving variables for the GEE modeling.

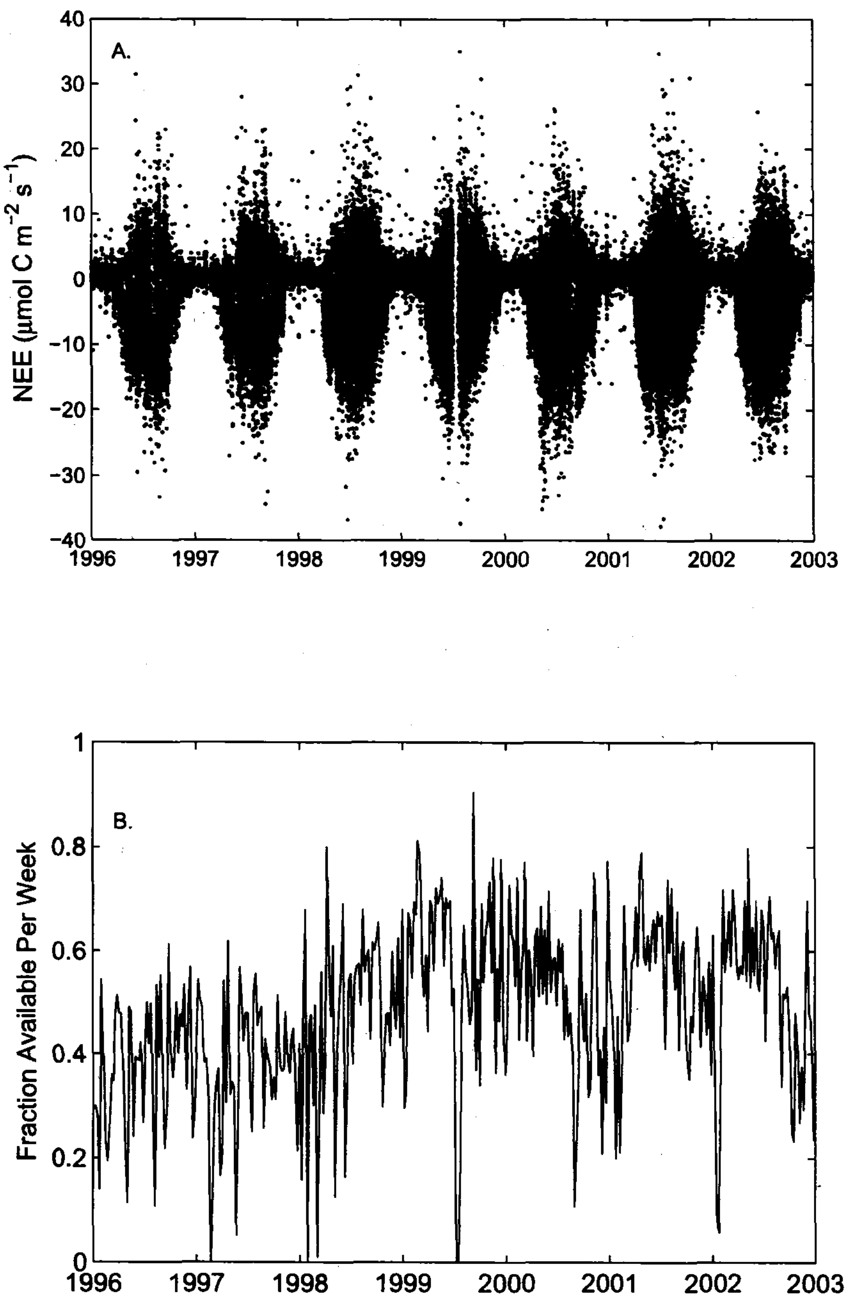

Figure 5.1. (a) Time series of valid observations of NEE at Howland Forest, Maine, and **(b)** the fraction available data per week. In this study we used half-hourly data for intervals in which u* > 0.25. Overall, the remaining observations amounted to 49% of the total time intervals.

5.3 Methods

To estimate GEE and the associated uncertainty range given an observed NEE time series, the following components are needed: (1) a statistical regression model, (2) an expression for the likelihood of the data given a model (which implicitly provides a cost function), and (3) a strategy for calculating distributions that represent the probability that a missing flux observation would have taken a certain value. From these distributions, attributes such as the mean and variance (i.e. uncertainty) of the GEE estimates can be derived for any desired time scale.

Our goal is to present a general analysis framework to bracket GEE estimates, rather than to present a comprehensive exploration of all possible model formulations that could be used in this context. Therefore, we chose two previously employed models for respiration and daytime NEE, one physiologically based (Hollinger et al. 2004), and the other a fully-empirical, nonlinear regression model (e.g. Papale & Valentini 2003). Our priority is to evaluate the magnitude and uncertainties associated with each approach, but not to compare the relative usefulness of the two approaches, primarily because they utilize different amounts of information from independent variables. We also evaluate two assumptions about the underlying error distribution of the modeled flux (i.e. the likelihood of the data given the model). One is a Gaussian error distribution, giving rise to least-squares estimates; the other is a two-sided exponential error distribution, giving rise to minimization of absolute differences.

We disaggregated the valid half-hourly CO_2 flux measurements into nighttime (PAR < 5 μmol m^{-2} s^{-1}) and daytime (PAR $\geq$ 5 μmol m^{-2} s^{-1}) periods. To model daytime respiration, we fit both a typical physiological ecosystem respiration model and an artificial neural network to the observed nighttime flux data. These models, which relate ecosystem respiration to observed biophysical variables (e.g., nighttime soil temperature), are then used to estimate daytime ecosystem respiration based on daytime observations of the same variables. To fill gaps in daytime NEE data, we again fit the same two types of models to the observed daytime flux data, based on environmental drivers (e.g., daytime air temperature and PAR), and then used the model to estimate daytime NEE based on the available data. We then estimated GEE using Equation 5.1, and calculated the uncertainty associated with the modeling using a bootstrapping approach, which produces empirical distribution functions for the modeled missing data.

We examined the influence of three factors on GEE estimates, resulting in eight sets of model results, parameters, and posterior distributions. We used two different models (physiological and neural network), assumed two different error models (Gaussian and two-sided exponential), and applied the method to the two flux data sets (respiration and daytime NEE) (Equation 5.1). In the following sections we discuss the details of these cases, and of the bootstrap algorithm.

5.3.1 Physiologically-based (PB) model

5.3.1.1 Respiration component

For respiration modeling, we used available nighttime respiration data to train a simple physiological model of respiration—a three-parameter exponential function of soil temperature at 5 cm depth, T_{soil} (Lloyd & Taylor, 1994; Hollinger *et al.*, 2004), with one set of parameters, regardless of season:

$$\hat{R} = Ae^{\frac{-E_0}{(T_{soil}-T_0)}} \tag{5.2}$$

where A is a scaling factor, E_0 is the soil temperature-adjusted activation energy (in degrees Kelvin), and T_0 is a reference soil temperature between 0° K and T_{soil}. Because A and E_0 are highly correlated parameters (Richardson and Hollinger, 2005), we fixed the value of E_0 at 113.4 K (Hollinger et al., 2004) and optimized the two remaining independent parameters, using a constrained minimization algorithm.

5.3.1.2 Daytime Net Ecosystem Exchange component

The physiological model we used to fill gaps in daytime NEE combines the respiration component above with a rectangular hyperbolic equation that relates photosynthesis to PAR, regulated by an optimum air temperature. This Michaelis-Menten type functional relationship requires fitting three additional parameters, for a total of five independent parameters:

$$\hat{F} = \begin{cases} Ae^{\frac{-E_0}{(T_{soil}-T_0)}} - \frac{P_m I_{PAR}}{I_{PAR}+K_m}\left(\frac{T_{air}^2}{a^2} - \frac{2T_{air}}{a}\right) & T_{air} > 0 \; and \; T_{soil} > 0 \\ Ae^{\frac{-E_0}{(T_{soil}-T_0)}} & T_{air} \leq 0 \; or \; T_{soil} \leq 0 \end{cases} \tag{5.3}$$

where I_{PAR} is the incident horizontal photosynthetically active radiation and T_{air} is the air temperature. The parameters are P_m, the maximum rate of photosynthesis, a, the normalized parabolic air temperature response with an intercept of zero, and K_m, the photosynthetic half-saturation constant. We used the previously optimized nighttime values for A and T_0 (Section 5.3.1.1). When T_{air} or T_{soil} is less than 0°C we assume that $GEE = 0$ and $\hat{F} = \hat{R}$.

The PB model was chosen for its simple representation of the system (i.e. five parameters) and its relatively wide use in the forest ecosystem community. For additional simplicity, the parameters are assumed constant across the years. Other analyses with Howland data suggest that fitted parameters of similar models change seasonally and between years (e.g. Hollinger et al., 2004; Gove and Hollinger, 2006).

5.3.2 Artificial Neural Network (ANN) model

The physiological models used here represent a family of functions whose characteristic shapes are constrained by prior knowledge of, or assumptions about, the relationships between a set of independent variables and the response (e.g. the soil temperature control of respiration). In contrast, the ANN approach focuses solely on characterizing the relationship between the valid NEE measurements and the climate measurements, making no assumptions about physiological processes, so the functional dependence of daytime NEE and respiration on biophysical predictor variables is not prescribed. Other studies have used this modeling approach for the purpose of gap filling flux data (e.g., Papale & Valentini, 2003).

We apply essentially the same ANN architecture separately to valid nighttime NEE data for modeling ecosystem respiration, and to valid daytime NEE data to model NEE where it is unavailable. The respiration model is driven by soil temperature, air temperature, surface soil moisture, and a seasonal indicator in the form of sine and cosine functions of the day of the year. The daytime NEE model adds photosynthetically active radiation (PAR), vapor pressure deficit (VPD), and sine and cosine functions of the hour of the day as additional input drivers.

An artificial neural network model is a multi-stage nonlinear regression function where the intermediate values are called hidden nodes. For example, with two stages $y=f(g(x))$, or more specifically:

$$y_k = f\left(\sum_{j=0}^{M} w_{kj}^{(2)} g\left(\sum_{i=0}^{D} w_{ji}^{(1)} x_i\right)\right), \tag{5.4}$$

where x represents the collection of independent variables in the regression (in our case the biophysical drivers). The outer function $f(\cdot)$ is usually linear and the inner function $g(\cdot)$ is a nonlinear, typically sigmoidal function, such as the hyperbolic tangent. The free parameters in this regression are "weights" w_{ji} *and* w_{kj}, which represent the strength of the connection between the ith input and the jth intermediate value (represented by the M evaluations of g) and also between the jth intermediate value and the kth output value y (in our case NEE or respiration). This ANN has D inputs and M hidden nodes.

This regression approach is referred to as a network because all inputs can influence all outputs, depending upon the values of the weights. For estimating the parameters, we use the standard backpropagation algorithm (Bishop, 1995), which updates the weights for each pair of $\{y_k, x_i\}$ data vectors in order to minimize the error. We also incorporate a Bayesian modification of artificial neural networks (MacKay, 1994) that limits the complexity of the model to that which is supported by the data, avoiding the common neural network problem of overfitting. In our study, we independently verified that the models do not overfit (as part of the K-fold validation exercise below) and, therefore, that the results are not dependent on the choice of the number of hidden nodes M.

5.3.3 Error distribution

There is evidence that errors associated with eddy flux observation are better represented by a two-sided exponential distribution than a Gaussian distribution, i.e. they are leptokurtic with outliers (Figure 5.2) (Hollinger and Richardson, 2005; Richardson and Hollinger, 2005). We performed a multi-part analysis with the two types of regression models, considering in each case both an underlying Gaussian and an underlying two-sided exponential distribution. We evaluated the assumptions of underlying error distribution by posterior analysis of the model residuals.

We alter our assumption of how the error is distributed by specifying the form of the cost function that is minimized in the optimization routine. When assuming a Gaussian error distribution, we minimized the usual least-squares error function. In the case of the two-sided exponential distribution assumption, we minimized the weighted absolute value of the residuals. We used weights based on the recommendation of Richardson and Hollinger (2005) that the intrinsic observational uncertainty is well represented by an exponential function of soil temperature. More specifically, as can be seen in the data, the uncertainty in flux observations scales with the magnitude of the flux (i.e. absolute error is larger when the absolute flux is larger), and to obtain an independent estimate of that uncertainty, we express the uncertainty as a function of soil temperature

5.3.4 Uncertainty analysis

Ecosystem carbon flux is an aggregate property of a system containing many physical, chemical, and biological interactions. For example, nighttime NEE generally increases exponentially with increasing soil temperature, and a simple physiological model captures the basic relationship (Figure 5.3a). However, substantial noise (i.e. model residuals) remains after this simple relationship has been accounted for (Figure 5.3b). This residual noise is due to both measurement uncertainty and model uncertainty (i.e. noisy data and an imperfect model), with model uncertainty potentially due to both parameterization and choice of functional form. In addition, the variance of these residuals can be heteroscedastic (i.e. not constant with respect to one or more of the independent variables); in this case, the residual variance varies with soil temperature (Fig 5.2b).

Many approaches to uncertainty estimation (e.g. least squares regression) assume that the data have constant variance and Gaussian noise, and that the regression model has independent identically distributed residuals. Eddy flux observations and associated models generally do not conform to these assumptions, but computational solutions exist. The bootstrapping approach (resampling with replacement) to uncertainty assessment is one of several techniques more appropriate than conventional analytic methods for data with heteroscedastic and non-normally distributed errors. This method assumes that the observed data represent only one possible realization out of many, and reconstructs a large number of alternate realizations based on random resampling of residuals.

Bootstrapping brackets the range of unobserved values conditioned on the assumption of the model and its associated likelihood function (Efron & Tibshirani, 1993).

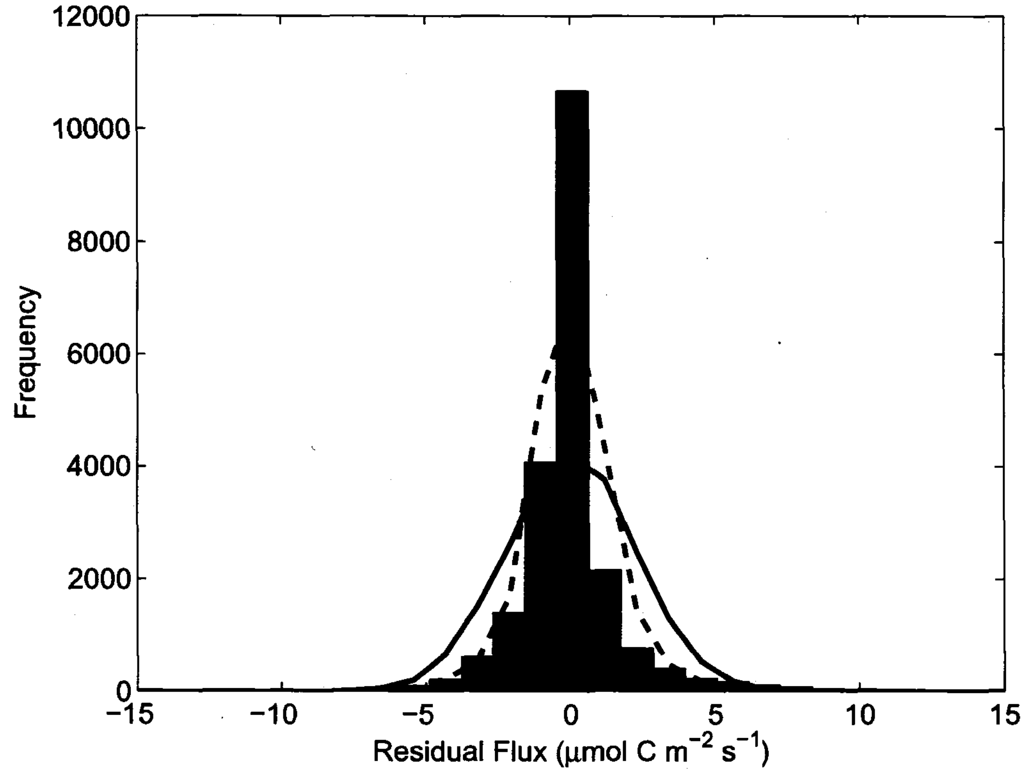

Figure 5.2. The residuals of a model fit to nighttime NEE, or ecosystem respiration, (shaded bars) are distributed with a kurtotic peak around zero. This distribution resembles a two-sided exponential distribution (dashed line) more than a normal distribution (solid line).

Previous studies have used Monte Carlo analyses for estimating modeling uncertainty in NEE and GEE, but most provide a measure of variability centered on the mean response of a model prediction at a point in time, and do not consider the additional uncertainty due to the random deviations from the mean response of any individual eddy flux observation (*e.g.* Griffis et al., 2003; Richardson & Hollinger, 2005). Other studies have accounted for the random processes associated with NEE, but have not considered the uncertainty in the mean response (e.g. Saleska et al., 2003). Uncertainty about the mean response is known as the *confidence interval*, while this same uncertainty plus the additional uncertainty due to inherent variations in the data is called the *prediction interval.*

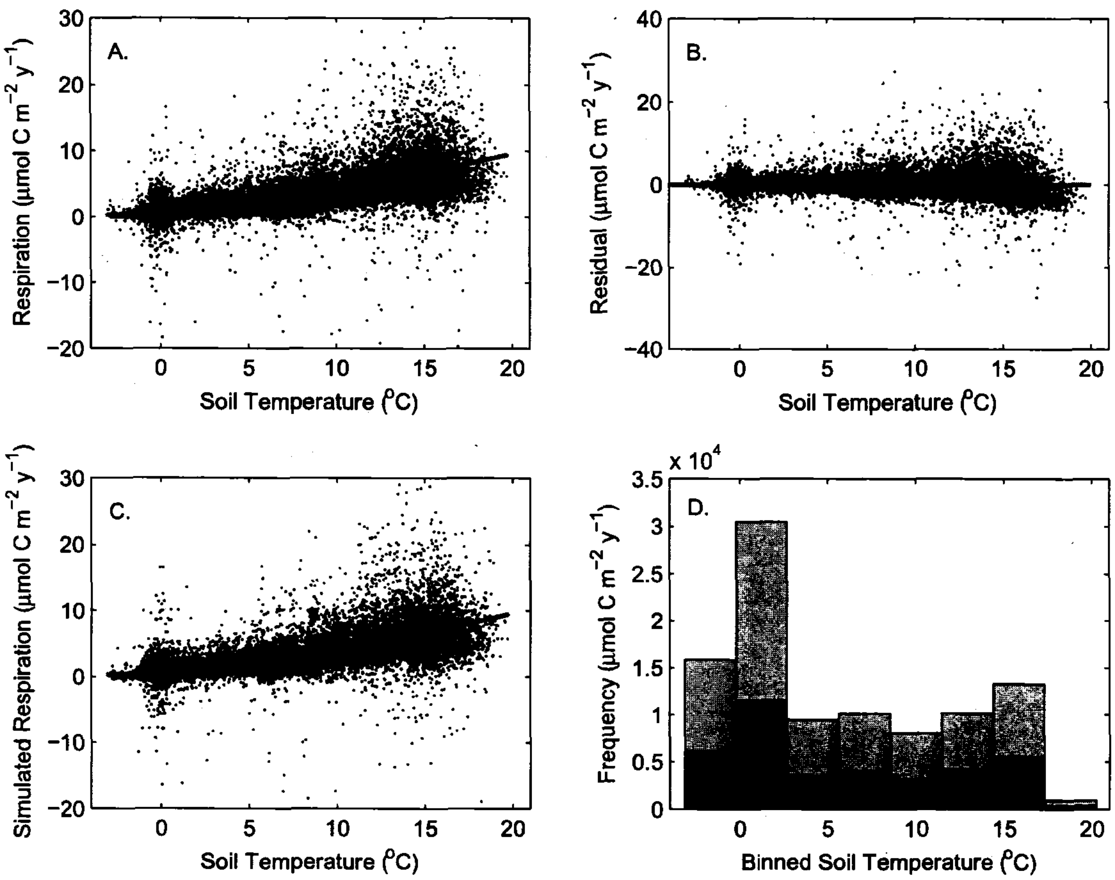

Figure 5.3. (a) Nighttime flux (respiration) was fit using an Arrhenius function (Lloyd & Taylor, 1994) of soil temperature (gray line; see Equation 5.2 in text). **(b)** The variance of the residuals from this model is heteroscedastic, with variance increasing at higher temperatures. **(c)** One example of the 1000 artificial data sets, constructed by randomly adding residuals (bootstrapping) to the simple fitted function in panel (a). **(d)** A histogram of soil temperature for the entire time period. Each bar is split into fraction of half-hours having a valid respiration observation (dark gray) and fraction needing modeled respiration (light gray). Bin locations and sizes from this histogram (d) were used to construct the artificial data sets (c).

In this study, we present uncertainty as a 90% *prediction interval*, which brackets uncertainty about an estimate based on new data (i.e. gap filling), which is an appropriate statistical measure of our knowledge (or lack of knowledge) about predicted values. Below, we outline our implementation of the non-parametric resampling approach (bootstrapping), which is based on the statistical theory of Efron & Tibshirani (1993) and recent algorithms described by others (e.g. Robert & Casella, 1999).

The bootstrap is a simulation based calculation of the properties of an arbitrary estimator, typically the bias or the standard error, and can also be used to calculate confidence and prediction intervals. Since in the bootstrap algorithm the data are resampled, there is no underlying assumption about the statistical distribution. In regression models, where the statistical assumptions pertain to the model errors, the residuals are resampled and added back to the fitted values to create bootstrap replicates of the data. The regression model is then refit to each replicate, and the resulting empirical distribution of the recalculated estimators provides the desired properties. In our case we evaluate the statistical properties (90% prediction intervals) of the estimators for the response where the original data were missing. This procedure makes no assumptions of the statistical distribution of the residuals. To account for heteroscedasticity as a function of a covariate variable we propose a simple residual binning (Step 3 below). The text below outlines the bootstrap algorithm:

Step 1. The regression model (either PB or ANN) is fit to the valid observations (e.g. Figure 5.3a).

Step 2. The residuals from this fit are calculated (e.g. Figure 5.3b), and the variance of the residuals is examined for a significant dependence on the driving variables (e.g. soil temperature).

Step 3. If there is significant heteroscedasticity, the main driver of the non-constant variance is identified. The range of this driving variable is divided into several intervals, and the residuals are binned based on the value of the driving variable at the time of measurement (e.g. Figure 5.3d). In the analysis, both daytime NEE and respiration residuals, for both the PB and ANN models, were divided into eight bins based on soil temperature.

Step 4. An artificial data set (e.g. Figure 5.3c) is created by adding the "model fit" predicted values (the line in Figure 3a) to random residuals drawn with replacement from the correct bin (Figure 5.3b).

Step 5. A revised PB or ANN model is fit to the bootstrapped data set (e.g. Figure 5.3c).

Step 6. This bootstrap model is used to predict flux values for the gap points (e.g. Figure 5.3d).

Step 7. A residual (from Step 2) is added to the predicted value (from Step 6) in the same manner as described in Step 4, to simulate the effect of random noise on any predicted or gap filled point. This step ensures that we capture the statistical prediction error, not just the uncertainty due to model parameterization.

Step 8. Repeat Steps 4-7 above N times (we used N=1000).

Step 9. Predicted values and prediction intervals are calculated using the empirical distributions of the results (e.g. Figure 5.4a). Every gap point in the time series will have N estimated values from N realizations of the resampled and re-fit time series.

Calculation of the quantiles of these values yields many metrics, including the median and 90% prediction limits.

<u>*Step 10.*</u> *N* complete component flux time series are generated by using the measured value at every point in the time series where there is an observation and by using a bootstrap-predicted value for those time steps with no measurement. Expected values and prediction limits for sums of fluxes are estimated from these *N* synthetic time series (Figure 5.4b).

5.3.5 Validation

We used two measures of performance to evaluate both the PB and the ANN models both for filling unavailable daytime flux and for estimating daytime respiration. First, we conducted a standard K-fold cross validation of the nighttime respiration models and daytime NEE models (Hastie et al. 2001), which allowed us to quantify out-of-sample model error. We split all the valid data into *K* randomly distributed groups. Initially, group 1 is set aside for testing, while the models are parameterized based on groups 2 through *K*. The fitted models are then used to predict the group 1 observations. Next, group 2 is set aside for testing, while groups 1 and 3 through *K* are used for training. This pattern proceeds until all *K* groups have been withheld for testing. We then computed the root mean squared error (RMSE), the weighted absolute value of the error (WAD), the correlation coefficient (R^2), and mean bias as measures of model performance.

A second evaluation of model performance allows us to investigate the accumulation of uncertainty as model predictions are aggregated (by summing) into longer temporal intervals. There are few long periods without missing observations (Figure 5.1b), but we identified in the 7-year Howland NEE time series 13 days having zero gaps and 73 days having only one gap. We compared the observed 48 half-hour total NEE to the 1000 model predicted NEE values for these 86 complete and near-complete days. While the models used in this analysis were generated without the data from the 86 days of interest, the uncertainty estimates were taken from the bootstrapping analysis described in Section 5.3.5.

5.4 Results and discussion

5.4.1 Half-hourly time step

5.4.1.1 Parameter optimization

The physiological parameter values that minimize the cost functions applied to the observed data are similar to the parameter values fit by Hollinger et al. (2004) in their analysis (Table 5.1), though they used a different subset of the data (1996 only). The artificial neural network used four hidden nodes (M = 4; Equation 5.4) for both the respiration model and the daytime NEE model. The optimized neural network parameters (i.e. weights) are not physiologically meaningful and therefore their values cannot be compared with other studies.

Respiration	Gaussian	Exponential
A	149.1	149.9
E_0	113.4	113.4
T_0	251.8	252.8
DayNEE		
P_m	22.3	18.8
K_m	344.8	300.1
a	22.4	24.4

Table 5.1. Optimal parameter values for the physiological models. E_0 is fixed in this exercise.

The residuals generated from the respiration model fit resembled a two-sided exponential error distribution more than a Gaussian distribution (Figure 5.2), which is in agreement with the observation that flux measurement uncertainty follows a Laplace rather than a Gaussian distribution (Hollinger & Richardson, 2005). This was also true for residuals from other models' fits (not shown). By changing the assumption of how the error is distributed, one changes the optimal parameters. There are many combinations of parameter values that fit the data nearly equally well. The flatness of the cost function near the optimum has been described thoroughly elsewhere (Radtke et al., 2002; Hollinger et al., 2004; Hollinger and Richardson, 2005).

5.4.1.2 Model validation

The K-fold cross validation results show that both modeling approaches (ANN and PB) reproduce observed daytime NEE and nighttime respiration reasonably well at the half-hourly time scale, with all correlation values (R^2) greater than or equal to 0.49 (Table

5.2). For respiration, the ANN and PB models fit the data approximately equally well, probably because both models are based primarily on soil temperature (with the addition of the time variables in the ANN approach). However, there is a larger discrepancy between the ANN and PB model fits to the daytime NEE observations.

The ANN modeling approach has a lower mean error than the PB approach in every case, expressed either as root mean squared error (RMSE) or weighted absolute deviation (WAD). This is expected because ANN provides more flexible choices for the functional dependence than the physiological model and a larger set of input variables. The daytime NEE models are less accurate (*i.e.* they have higher RMSE or WAD) than the respiration models, likely because daytime NEE observations have higher variance than nighttime respiration observations.

Gaussian Error			
	R^2	Bias	RMSE
Respiration		(μmols m^{-2} s^{-1})	
Artificial Neural Net	0.53 ± 0.01	0.00 ± 0.02	2.21 ± 0.04
Physiological	0.51 ± 0.01	-0.03 ± 0.02	2.28 ± 0.03
DayNEE			
Artificial Neural Net	0.75 ± 0.01	-0.00 ± 0.01	3.12 ± 0.04
Physiological	0.50 ± 0.01	-0.01 ± 0.03	4.56 ± 0.04
Two-sided Exponential Error			
	R^2	Bias	WAD
Respiration		(μmols m^{-2} s^{-1})	
Artificial Neural Net	0.52 ± 0.01	0.27 ± 0.02	0.67 ± 0.01
Physiological	0.50 ± 0.01	0.28 ± 0.01	0.71 ± 0.01
DayNEE			
Artificial Neural Net	0.70 ± 0.01	0.16 ± 0.03	1.31 ± 0.02
Physiological	0.49 ± 0.00	-1.04 ± 0.03	2.86 ± 0.02

Table 5.2. K-fold validation results for all of the modeling filling approaches

Changing the assumption of error distribution has a small effect on the cross-validation results of the respiration model, increasing the error (e.g. $RMSE_{gauss}$-$RMSE_{exp}$ or WAD_{exp}-WAD_{gauss}) by at most 5%. This change has a slightly larger effect on the daytime NEE models, increasing the error by up to 10%. The magnitude of change in this K-fold error statistic is an indication of the model's sensitivity to assumptions about the error distribution and the daytime NEE models are more sensitive to this assumption.

The cross-validation results indicate that all models assuming a Gaussian error distribution have no statistically significant model bias (Table 5.2). The models using weighted observations and a two-sided exponential distribution in the cost function, however, all show a significant bias. This bias is an expected by-product of the model assumptions, particularly the weighting of observations. The weighting scheme assumes that the observations taken during high soil temperatures are less reliable and, therefore, the influence of residuals taken at high soil temperatures is reduced. These assumptions reflect a belief about how best to accommodate heteroscedastic data and occasional large instrumentation errors (Richardson and Hollinger, 2005).

5.4.1.3 GEE estimates

Each modeling approach (PB/ANN and Gaussian/Exponential) produces one time series of daytime NEE and a second of daytime respiration, both at half-hour intervals. The daytime NEE time series contains observed fluxes where data are available, and modeled fluxes where they are not. The daytime respiration time series has only modeled fluxes.

By applying the bootstrapping algorithm, we generate one thousand time series, each representing a simulated potential time series that includes uncertainty in the model parameters as well as uncertainty due to the random nature of the flux observation. One thousand GEE time series are estimated by subtracting the 1000 daytime NEE time series from the 1000 respiration time series (Equation 5.1). Thus, each daytime half-hour has 1000 simulated GEE estimates that approximate the distribution of values that could have been observed given the data and the modeling assumptions. The simulated GEE estimates for any half-hour can be displayed as a histogram (Figure 5.4a). From this histogram, we can extract several statistics of interest, including the mean, median, upper 90% value, and lower 90% value.

At the half-hour time scale, the GEE estimates generated from the bootstrapping algorithm are often skewed (Figure 5.4a). This skewness reflects a skewness in the model residuals and, ultimately, in the flux observations themselves. The nighttime flux (i.e. respiration) record contains more unusually high flux measurements (i.e. positive; flux out of the canopy and into the atmosphere) than unusually low (i.e. negative) flux measurements, while the daytime flux record is skewed in the opposite direction. To estimate GEE, we subtract daytime NEE flux from respiration, which magnifies the skewness in the GEE estimates.

At the half-hour scale, the GEE estimates generated from the four approaches are never significantly different at the 90% prediction limit level. While the median bootstrapped estimates predicted from any approach at any half-hour are different, the statistical uncertainty reflected by the 90% prediction limits is large relative to this difference. The ANN models generally predict slightly higher GEE during half-hours with high I_{PAR} than the PB models. During low I_{PAR} levels, the PB models predict higher GEE than the ANN models.

5.4.2 Daily time step: validation of complete-day NEE

Both model approaches validate reasonably well using the 86 complete-day data points (all $R^2 > 0.48$), though the ANN has a higher correlation and a lower RMSE and mean bias (Table 5.3, Figure 5.5). In the context of this analysis, changing the assumption of normally distributed residuals to an assumption of two-sided exponentially distributed residuals does not improve the accuracy of the predictions. The 90% prediction limits around each daily prediction in this small sample are apparently underestimates of the actual uncertainty, as only about 70% of the prediction limits touch the 1:1 line.

5.4.3 Annual time step: GEE estimates and 90% prediction limits

Annual GEE estimates for each modeling approach are generated by aggregating each of the 1000 individual GEE time series to the annual scale. At this scale, annual GEE estimates are approximately normally distributed (Figure 5.4b). They are no longer significantly skewed or kurtotic, so that the mean estimates and the median estimates are effectively equal.

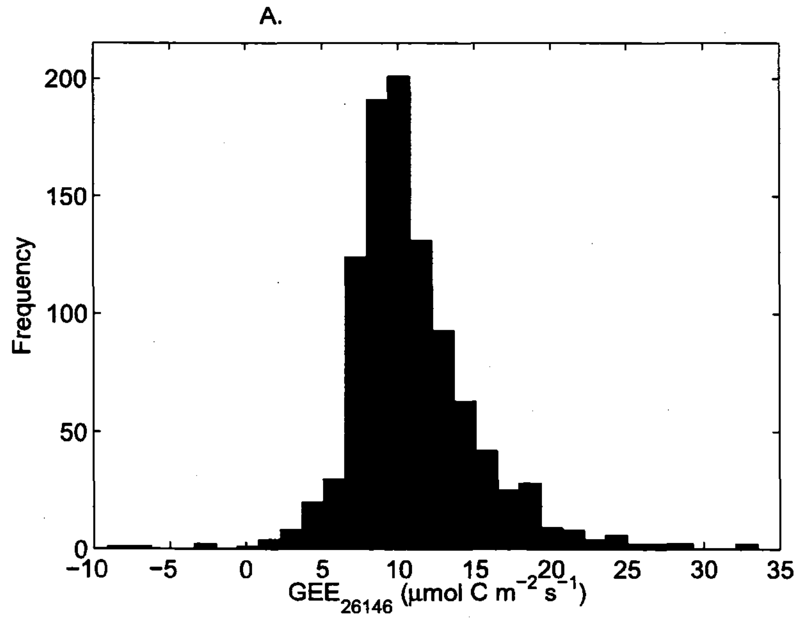

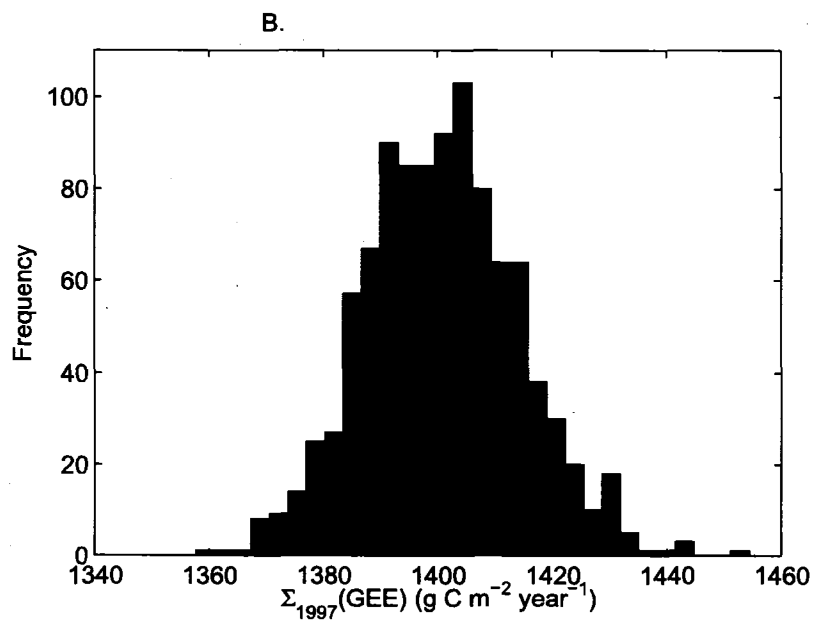

Figure 5.4. (a) The bootstrapping algorithm produces empirical probability distributions for each daytime half-hour. Most half-hourly distributions of simulated GEE are leptokurtic and skewed, like the example displayed here (4:30-5:00PM on June 28, 1997). **(b)** Aggregating (by summing) the half-hour GEE simulations to the annual scale, for each bootstrapped data set produces an annual empirical distribution. These predictions are generally approximately normally distributed.

	R^2	RMSE ($g\ C\ m^{-2}\ day^{-1}$)	Daily Mean Bias ($g\ C\ m^{-2}\ day^{-1}$)
Gaussian Error			
Artificial Neural Net	0.75	0.74	-0.23
Physiological	0.53	1.15	-0.50
Two-sided Exponential Error			
Artificial Neural Net	0.72	0.74	-0.05
Physiological	0.48	1.16	-0.52

Table 5.3. Complete day validation results for the NEE gap filling approaches, based on 86 days with fewer than 2 missing half-hour intervals.

The annual GEE sums estimated in this analysis (Figure 5.6) are generally consistent with previous estimates for the Howland site using the same data (Hollinger et al. 2004), and with those based on mechanistic model predictions (e.g. PnET model; Aber et al., 1992). This similarity includes the overall absolute values of the magnitude of the flux as well as the rank order of annual values. However, focusing especially on interannual patterns, there is a consistent offset between the modeling approaches.

The bootstrapped estimates of the annual 90% prediction intervals average 40 g C m^{-2} $year^{-1}$ for the ANN approach and 30 g C m^{-2} $year^{-1}$ for the PB approach. The year-to-year variability in GEE is smaller than the magnitude of uncertainty at the annual time scales in at least three of the six pairs of adjacent years (i.e. three of six pairs in the PB and four of six pairs in the ANN). Changing the cost function to reflect the assumption of exponentially distributed error slightly reduces our estimates of statistical uncertainty (Figure 5.6). All methods agree in predicting higher GEE at Howland over the 1998-2001 period than before or after this time.

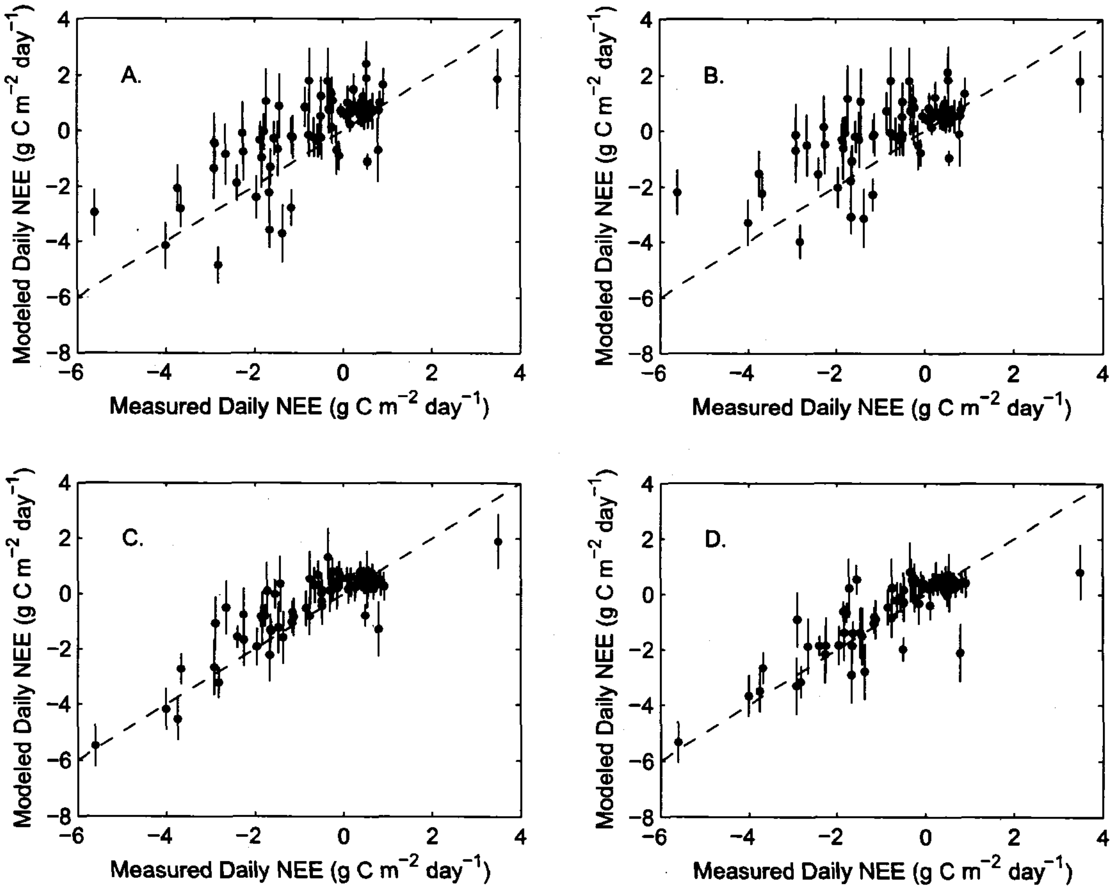

Figure 5.5. Modeled versus measured daily NEE for 86 complete or nearly complete days in the Howland Forest time series, using four model and error distribution combinations: **(a)** PB Gaussian; **(b)** PB exponential; **(c)** ANN Gaussian; **(d)** ANN exponential. Error bars represent 90% bootstrap intervals.

5.4.4 Statistical uncertainty in GEE estimates across time

The 90% annual prediction intervals from the different methods are generally offset from one another and in many cases do not overlap. This may be due to the fact that our analysis accounts only for uncertainties associated with statistical modeling, and is consistent with the likely influence of other external factors. The offset of prediction intervals within a year also shows that uncertainty related to model selection contributes

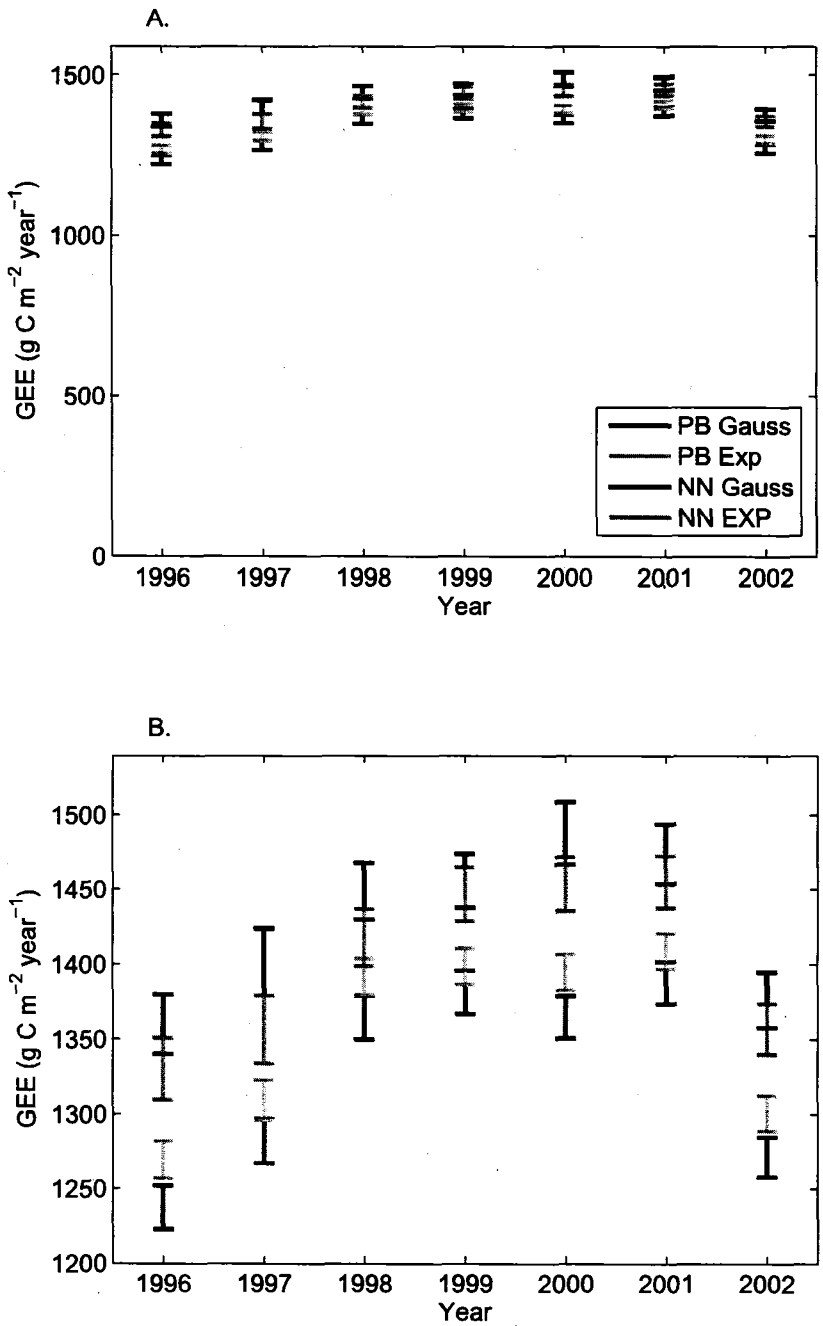

Figure 5.6. Time series of annual GEE. The panels show the same data at different scales. **(a)** The difference in estimates of annual total GEE from the four modeling approaches is small relative to the magnitude of GEE, as is the statistical uncertainty. **(b)** The annual GEE estimates do exhibit dependence on the method chosen for gap filling daytime NEE and respiration modeling. The statistical uncertainty due to model fitting and the random variability of the observations is comparable to the uncertainty due to model selection. Interannual variability in GEE is partially masked by statistical uncertainty and nearly completely masked by model selection uncertainty, but the overall patterns are almost identical (i.e. the rank correlation is very high).

considerably to the overall range of possible GEE estimates. This overall range is difficult to quantify comprehensively because the total number of models that can be used is not finite. However, the two models used here represent two extremes, both in terms of the number of variables and the way in which the variables are used.

Though the nonlinear regressions are quantitatively more accurate than the physiologically based regression, there is no objective basis for choosing one approach over the other. A process-oriented model (e.g. Equations 5.2 and 5.3) may contain useful prior functional constraints about ecosystem carbon fluxes. Alternatively, a regression model that synthesizes the data record most accurately (e.g. Equation 5.4) may be the best choice if we desire estimates that mimic the behavior of the data rather than provide insights about the processes or capacity for extrapolation.

5.5 Conclusions

Tower-based estimates of GEE represent a potentially important source of ecosystem information that is derived by a combination of data and models. As such, they require more analytical processing than most data sets that are considered "observations", but they also are likely to be used as data to a greater extent than most quantities that are considered "model outputs". The objective of this analysis was to provide a framework for estimation of uncertainty in tower-based GEE time series. Specifically, we are interested in quantifying the prediction intervals associated with regression models that are needed to (1) extrapolate respiration into the day, and (2) fill missing NEE values in the day. These prediction intervals correspond to the range of values we would likely observe, given the valid data and the model assumptions. We have used a computational technique that is intended to bracket the range of likely observations, but it is not guaranteed to bracket the unknown "true" values of GEE flux. We did not explore a large number of different regression models, but instead illustrated the issue by using two different modeling approaches. Valid arguments could be made for the use of either approach, and we do not recommend one over the other.

The statistical uncertainty in annual GEE estimates at Howland Forest associated with each model type, is about 30-40 g C m^{-2} $year^{-1}$ (90% prediction limit). Our results indicate that the uncertainty due to model assumptions is greater than the statistical uncertainty associated with any particular model. The combined uncertainty due to modeling in the GEE estimates is nearly the same magnitude as the interannual variability. These estimates are similar in magnitude to the uncertainty in NEE arising from systematic errors associated with choice of nocturnal u* threshold (Hollinger et al. 2004).

While our analysis indicates a relatively small amount of uncertainty in the absolute value of GEE at the annual scale, this relative uncertainty is much larger at shorter time scales and is a dominant feature when considering half-hourly to daily fluxes (Figure 5.7). Furthermore, the interannual variability of the GEE flux, which is a key focus point for research into process controls linking environment and ecosystems, is often masked by the uncertainty from one year to the next. The implications of this result are potentially significant, and should be investigated independently at other sites and with other methods. On the other hand, the consistent patterns of the variability between model types indicate that some insight can still be gained about larger trends without considering explicitly the absolute magnitude of the GEE flux (Figure 5.6b).

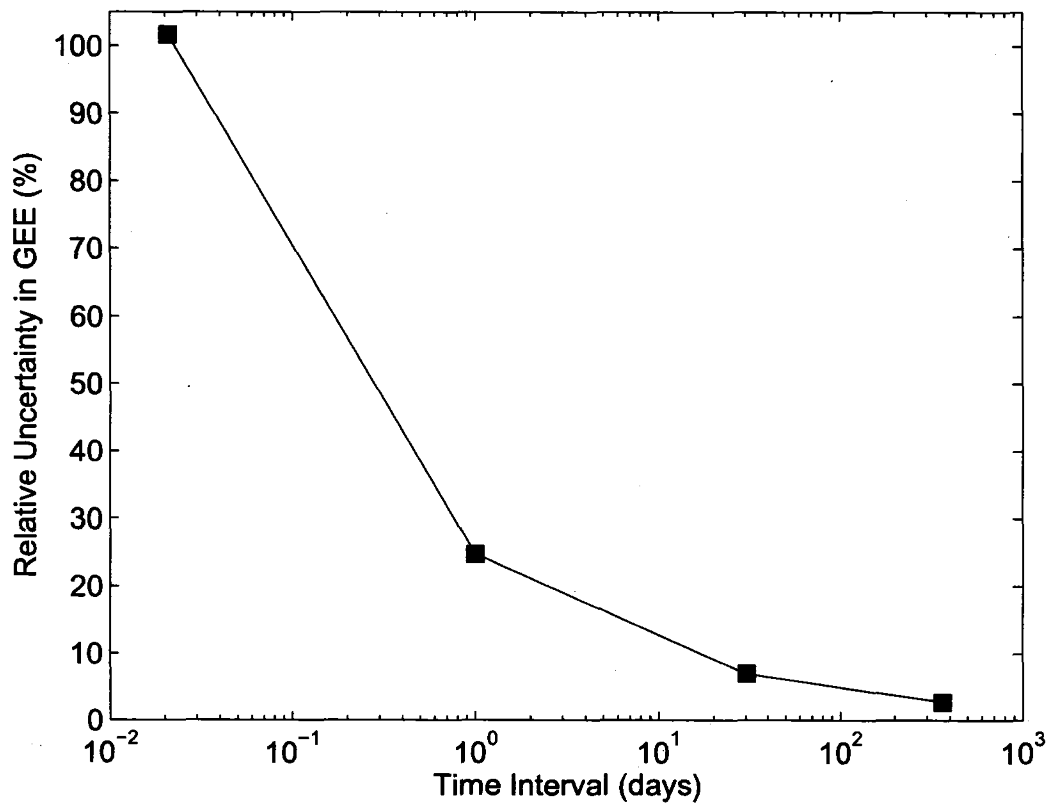

Figure 5.7. The relative uncertainty, expressed as the magnitude of the mean 90% prediction interval divided by the mean prediction value, of the ANN-modeled Gaussian GEE as a function of time step on a log scale. This relative uncertainty, as with the other approaches (not shown) drops dramatically as GEE is aggregated over time (half-hourly, daily, monthly, annually). This result is attributable to the fact that the statistical uncertainty adds approximately in quadrature and reflects the law of large numbers in estimating mean quantities (i.e., standard errors shrink with increasing sample size).

The complexity of this data set and the nature of the GEE calculation make error estimation sensitive to statistical assumptions. The impact of our choice of underlying error distribution assumption was significant, but less so than the differences associated with the selection of a model. While future work is needed to further integrate sources of uncertainty, evaluate alternate modeling techniques, and generalize results across multiple sites, this paper represents an initial step in the characterization of uncertainty in gross ecosystem fluxes from the bottom-up (e.g. in-situ observations) and is useful in conjunction with top-down estimates (e.g. satellite observations, model inversions).

CHAPTER 6

CONCLUSIONS

The process of translating raw mechanical observations into ecologically relevant attributes is likely to become the focus of more intense research in the coming years and decades, as more sophisticated means of Earth observation are designed and implemented. The design of new observing instrumentation is not likely to render optical reflectance satellite systems obsolete, however. Optical reflectance data provide critical information related to the land surface. There is still a need for improving the translation of optical reflectances obtained from satellites into information about land cover at a regional scale.

Today, limitations in the satellite overpass frequency combined with frequent cloud-cover and a thick atmosphere, make annual mapping of the Amazonian land surface with Landsat-type data alone infeasible. If annual land surface information is desired at the regional to continental scale, coarser resolution reflectance data, such as MODIS, must be used. Techniques for extracting sub-pixel information from MODIS data have improved and the practice of quantifying and reporting uncertainty in these data is more common. Examples of these improved techniques are featured in the research presented here.

We have made strides in the process of deriving useful information about the Brazilian Amazonian land surface from coarse resolution optical reflectance data. By combining information from Landsat-scale data with coarser resolution data, such as MODIS, it is now possible to derive a spatially and temporally complete map of land cover. Coarser resolution maps derived from MODIS-like data are improved with information from higher resolution Landsat data. Deriving changes in the land cover on a regional scale with coarse resolution data remains a challenge. Uncertainty in MODIS estimates of sub-pixels land cover fraction are often the same order of magnitude as annual changes in land cover fractions, making it difficult to identify changes in all but the most dynamic pixels. Until efforts to isolate the signal from the noise are more fruitful, alternative methods to estimating changes in land cover should be pursued.

By sub-sampling a large region with Landsat-type data over multiple consecutive years, one can follow land cover transitions of individual parcels of land with high certainty. This sub-sampling is cost effective and not likely to be limited by cloudiness or the atmosphere, as long as one is flexible as to which areas are sampled. Rates of land cover change in the sub-sampled areas can then be interpolated across the larger region. On potential means of interpolation would be to identify a relationship between the rate of change and a static feature that is measurable at the larger region. For example, if one identifies a relationship between persistence of secondary vegetation and the fraction of cleared area with in a region, then persistence can be estimated over a larger region using coarse resolution maps of fraction of cleared area. A second method for interpolation could be spatial statistics, such as kriging. This method assumes that rates of change are spatially dependent. The land cover transition rates can be used in conjunction with a coarse resolution map (i.e. MODIS-based) to identify the extent and dynamics of land cover at a regional scale.

Whether the translation to ecologically relevant information has as its source remote sensing-based or ground-based observations, accurate estimates of uncertainty remain vital. Increasingly complex modeling and estimation techniques require flexible and robust uncertainty estimation methods. The Monte Carlo bootstrapping approach and other non-parametric approaches provide the flexibility to estimate prediction intervals while making minimal assumptions. While more research is needed to incorporate additional potential sources of uncertainty and improve efficiency in the bootstrapping algorithm, this document presents a viable approach to estimating uncertainty that is applicable across a wide array of ecological applications.

LIST OF REFERENCES

Aber, J.D. and C.A. Federer (1992). A generalized, lumped-parameter model of photosynthesis, evapotranspiration and net primary production in temperate and boreal forest ecosystems.*Oecologia*, 92, 463-474.

Adams, J., Sabol, D., Kapos, V., Filho, R., Roberts, D., Smith, M., & Gillespie, A. (1995). Classification of multispectral images based on fractions of endmembers: application to land-cover change in the Brazilian Amazon. *Remote Sensing of Environment*, 52, 137-154.

Aide, T.M. (1993). Patterns of leaf development and herbivory in a tropical understory community. *Ecology*, 74 (2), 455-466.

Allen, J.C. and D.F. Barnes (1985). The causes of deforestation in developing countries. *Annals of the Association of American Geographers*, 75, 163-184.

Alves D.S., and D.L. Skole (1996). Characterizing land cover dynamics using multi-temporal imagery. *International Journal of Remote Sensing*, 17 (4), 835-839.

Alves, D.S., J.L.G. Pereira, L. De Sousa, J.V. Soares, and F. Yamaguchi (1999). Characterizing landscape changes in central Rondônia using Landsat TM imagery. *International Journal of Remote Sensing*, 20 (14), 2877-2882.

Alves, D.S., M.I.S. Escada, J.L.G. Pereira, and C. Albuquerque Linhares (2003). Land use intensification and abandonment in Rondonia, Brazilian Amazonia. *International Journal of Remote Sensing*, 24 (4), 899-903.

Arroyo-Mora, J.P., G.A. Sanchez-Azofeifa, M.E.R. Kalacska, and B. Rivard (2005). Secondary forest detection in a neotropical dry forest landscape using Landsat ETM+ and IKONOS imagery. *Biotropica*, 37 (4), 497-507.

Asner, G.P. C.A. Wessman, and J.L. Privette (1997). Unmixing the directional reflectances of AVHRR sub-pixel landcovers. *IEEE Transactions on Geosciences and Remote Sensing*, 35 (4), 868-878.

Asner, G., Braswell, B., Schimel, D., & Wessmen, C. (1998). Ecological research needs from multiangle remote sensing data. *Remote Sensing of Environment*, 63, 155-165.

Asner, G.P., A.R. Townsend, and B.H. Braswell (2000). Satellite observations of El Nino effects on Amazon phenology and productivity. *Geophysical Research Letters*, 27, 981-

984.

Asner, G. (2001). Cloud cover in Landsat observations of the Brazilian Amazon. *International Journal of Remote Sensing*, 22 (18), 3855-3862.

Asrar G., M. Fuchs, E.T. Kanemasu and J.H. Hatfield (1984). Estimating absorbed photosynthetic radiation and leaf area index from spectral reflectance in wheat. *Agronomy J.*, 76, 300-306.

Atkinson, P.M., M.E.J. Cutler, and H. Lewis (1997). Mapping sub-pixel proportional land cover with AVHRR imagery. *International Journal of Remote Sensing*, 18 (4), 917-935.

Baldocchi, D.D. and Christoph A. Vogel (1996). Energy and Carbon Dioxide Flux Densities Above and Below a Temperate Broad-leaved Forest and a Boreal Pine Forest. *Tree Physiology*, 16, 5-16.

Batista, G.E., Y.E. Shimabukuro, and W.T. Lawrence (1997). The long-term monitoring of vegetation cover in the Amazonian region of northern Brazil using NOAA-AVHRR data. *International Journal of Remote Sensing*, 18, 3195-3210.

Bishop, C.M. (1995). *Neural Networks for Pattern Recognition*. Oxford University Press: Oxford.

Bohlman, S.A., J.B. Adams, M.O. Smith, and D.L. Peterson (1998). Seasonal foliage changes in the eastern Amazon basin detected from Landsat Thematic Mapper satellite images. *Biotropica*, 30 (3), 376-391.

Braswell, B., Schimel, D., Privette, J., Moore, B., Emery, W., Sulzman, E., & Hudak, A. (1996). Extracting ecological and biophysical information from AVHRR optical data: An integrated algorithm based on inverse modeling. *Journal of Geophysical Research*, 101 (D18), 23,335-23,348.

Braswell, B.H, E. Linder, S. Hagen, X. Xiao, S. Frolking, B. Moore, and J. Liu (2000). A Bayesian unmixing algorithm for retrieving landcover distributions using global reflectance data. Presented at American Geophysical Union Fall Meeting, San Franciso, CA, USA, December 15-19.

Braswell, B.H., S.C. Hagen, S. Frolking, and W.A. Salas (2003). A multivariable approach for mapping sub-pixel land cover distributions using MISR and MODIS: Applications in the Brazilian Amazon region. *Remote Sensing of Environment*, 87, 243-256.

Braswell, B.H., B. Sacks, E. Linder, and D.S. Schimel (2005). Estimating ecosystem process parameters by assimilation of eddy flux observations of NEE. *Global Change Biology*, 11, 335-355.

Browder, J.O. (1994). Surviving in Rondonia: The dynamics of colonist farming strategies in Brazil's northwest frontier. *Studies in Comparative International Development*, 29 (3), 45-69.

Brown, S. and A.E. Lugo (1990). Tropical secondary forests. *Journal of Tropical Ecology*, 6, 1-32.

Cardille, J., Foley, J., & Costa, M. (2002). Characterizing patterns of agricultural land use in Amazonia by merging satellite classifications and census data. *Global Biogeochemical Cycles*, 16 (3), 18.

Chaterjee, S. & Price, B. (1991). *Regression Analysis By Example*. (pp. 235-242). New York: Wiley.

Chomentowski, W., W.A. Salas, and D. Skole (1994). Landsat Pathfinder Project Advances Deforestation Mapping. *GIS World*, 7, 34-38.

Costa, M.H. & Foley, J.A. (2000). Combined effects of deforestation and doubled atmospheric CO2 concentrations on the climate of Amazonia. *Journal of Climate*, 13 (1), 18-34.

Cross, A., Settle, J., Drake, N., & Paivinen, R. (1991). Subpixel measurement of tropical forest cover using AVHRR data. *International Journal of Remote Sensing*, 12 (5), 1119-1129.

Dale, V.H., R.V. O'Neill, F. Southworth, and M. Pedlowski (1994). Modeling effects of land management in the Brazilian Amazonia settlement of Rondonia. *Conservation Biology*, 8 (1), 196-206.

Deering, D. (1989). Field measurements of bidirectional reflectance. In G. Asrar (Ed.), *Theory and Applications of Optical Remote Sensing* (pp. 14-65). New York: Wiley.

DeFries, R., Hansen, M., Townshend, J.R.G. & Sohlberg, R. (1998). Global land cover classifications at 8 km spatial resolution: The use of training data derived from Landsat Imagery in decision tree classifiers. *International Journal of Remote Sensing*, 19 (16), 3141-3168.

Di Maio Mantovani, A.C. and A.W. Setzer (1997). Deforestation detection in the Amazon with an AVHRR-based system, *International Journal of Remote Sensing*, 18 (2), 273-286.

Efron, B., and R.J. Tibshirani (1993). *An Introduction to the Bootstrap*, Chapman & Hall, New York.

Falge, E., D. Baldocchi, R. Olson, P, Anthoni, M. Aubinet, C. Bernhofer, G. Burba, R. Ceulemans, R. Clement, H. Dolman, A. Granier, P.Gross, T. Grunwald, D. Hollinger, N.O. Jensen, G. Katul, P. Keronen, A. Kowalski, C.T. Lai, B.E. Law, T. Meyers, H. Moncrieff, E. Moors, J.W. Munger, K. Pilegaard, U. Rannik, C. Rebmann, A. Suyker, J. Tenhunen, K. Tu, S. Verma, T. Vesala, K. Wilson, and S. Wofsy (2001). Gap filling strategies for defensible annual sums of net ecosystem exchange. *Agricultural and Forest Meteorology*, 107, 43-69.

Fearnside, P.M (1990). The rate and extent of deforestation in Brazilian Amazonia. *Environmental Conservation*, 17 (3), 213-226.

Fearnside, P.M. (1996). Amazonian deforestation and global warming: carbon stocks in vegetation replacing Brazil's Amazon forest. *Forest Ecology and Management*, 80, 21-34.

Feldpausch, T.R., S.J. Riha, E.C.M. Fernandes, and E.V. Wandelli (2005). Development of forest structure and leaf area in secondary forests regenerating on abandoned pastures in central Amazonia. *Earth Interactions*, 9, Paper No. 6.

Ferraz, S.F., C.A. Vettorazzi, D.M. Theobald, and M.V.R. Ballester (2005). Landscape dynamics of Amazonian deforestation between 1984 and 2002 in central Rondonia, Brazil: assessment and future scenarios. *Forest Ecology and Management*, 204, 67-83.

Fisher, P. (1997). The pixel: a snare and a delusion. *International Journal of Remote Sensing*, 18 (3), 679-685.

Foody, G.M. and D.P. Cox (1994). Sub-pixel land cover composition estimation using a linear mixture model and fuzzy membership functions. *International Journal of Remote Sensing*, 15 (3), 619-631.

Foody, G., Lucas, R., Curran, P., & Honzak, M. (1997). Non-linear mixture modeling without end-members using an artificial neural network. *International Journal of Remote Sensing*, 18 (4), 937-953.

Foody, G.M., D.S. Boyd, and M.E.J. Culter (2003). Predictive relations of tropical forest biomass from Landsat TM data and their transferability between regions. *Remote Sensing of Environment*, 85, 463-474.

Frietas, S.R., M.C.S. Mello, and C.B.M. Cruz (2003). Relationships between forest structure and vegetation indices in Atlantic Rainforest. Forest Ecology and Management, 218, 353-362.

Frohn, R.C., K.C. McGwire, V.H. Dale, and J.E. Estes (1996). Using satellite remote sensing to evaluate a socio-economic and ecological model of deforestation in Rondônia, Brazil. *International Journal of Remote Sensing*, 17 (16), 3233-3255.

Frolking, S., Qiu, J., Boles, S., Xiao, X., Liu, J., Li, C., & Qin, X. (2002). Combining remote sensing and ground census data to develop new maps of the distribution of rice agriculture in China. *Global Biogeochemical Cycles* 16 (4), 38.

Gao, B. (1996). NDWI- A normalized difference water index for remote sensing of vegetation liquid water from space. *Remote Sensing of Environment*, 58, 257-266.

Goulden, M.L., J.W. Munger, S. Fan, B.C. Daube, and S.C. Wofsy (1996a). Exchange of carbon dioxide by a deciduous forest: Response to interannual climate variability. *Science*, 271, 1576-1578.

Goulden, M.L., J.W. Munger, S. Fan, B.C. Daube, and S.C. Wofsy (1996b). Measurements of carbon sequestration by long-term eddy covariance: methods and a critical evaluation of accuracy. *Global Change Biology*, 2, 169-182.

Gove, J.H., and D.Y. Hollinger (2006). Application of a dual unscented Kalman filter for simultaneous state and parameter estimation in problems of surface-atmosphere exchange. *Journal of Geophysical Research*, 111, D08S07, doi:10.1029/2005JD006021.

Grant, I. (2000). Investigation of the variability of the directional reflectance of Australian land cover types. *Remote Sensing Reviews,* 19, 243-258.

Griffis, T.J., T.A. Black, K. Morgenstern, A.G. Barr, Z. Nesic, G.B. Drewitt, D. Gaumont-Guay, and J.H. McCaughey (2003). Ecophysiological controls on the carbon balances of three southern boreal forests. *Agriculture and Forest Meteorology*, 17, 53-71.

Hagen, S.C, Braswell, B.H, Frolking, S., Salas, W.A, and Xiao, X. (2002). Determination of subpixel fractions of nonforested area in the Amazon using multiresolution satellite sensor data. *Journal of Geophysical Research*, 107, D20, 8049, doi:10.1029/1000JD000255.

Hagen, S.C., B.H. Braswell, E. Linder, S. Frolking, A.D. Richardson, and D.Y. Hollinger (2006) Statistical uncertainty of eddy flux-based estimates of gross ecosystem carbon exchange at Howland Forest, Maine. *Journal of Geophysical Research-Atmospheres*, (111): D08S03, doi:10.1029/2005JD006154.

Hastie, T., R. Tibshirani, and J. Friedman (2001). *The Elements of Statistical Learning: Data Mining, Inference, and Prediction.* Springer-Verlag, New York.

Haugaasen, T. and C.A. Peres (2005). Tree phenology in adjacent Amazonian flooded and unflooded forests. *Biotropica*, 37 (4), 620-630.

Hecht, S.B. and A. Cockburn (1989). *The Fate of the Forest*, Verso, London.

Hlavka, C. & Spanner, M. (1995). Unmixing AVHRR imagery to assess clearcuts and forest regrowth in Oregon. *IEEE Transactions on Geoscience and Remote Sensing*, 33 (3), 788-795.

Holben, B. (1986). Characteristics of maximum-value composite images from temporal AVHRR data. *International Journal of Remote Sensing*, 7 (11), 1417-1434.

Holben, B.N. and Y.E. Shimabukuro (1993). Linear mixing applied to coarse spatial resolution data from multispectral satellite sensors. *International Journal of Remote Sensing*, 14 (11), 2231-2240.

Hollinger, D. Y., S. M. Goltz, E. A. Davidson, J. T. Lee, K. Tu, H. T. Valentine (1999). Seasonal patterns and environmental control of carbon dioxide and water vapour exchange in an ecotonal boreal forest. *Global Change Biology*, 5, 891-902.

Hollinger, D. Y., J. Aber, B. Dail, E. A. Davidson, S.M. Goltz, H. Hughes, M. Y. Leclerc, J. T. Lee, A. D. Richardson, C. Rodrigues, N. A. Scott, D. Achuatavarier, and J. Walsh (2004). Spatial and temporal variability in forest-atmosphere CO_2 exchange. *Global Change Biology*, 10, 1689-1706.

Hollinger, D.Y., and A.D. Richardson (2005). Uncertainty in eddy covariance measurements and its application to physiological models, *Tree Physiology*, 25, 873-885.

Houghton, R.A., D.S. Lefkowitz, and D.L. Skole (1991). Changes in the landscape of Latin America between 1850 and 1985. *Forest Ecology and Management*, 38, 143-199.

Houghton, R.A., Skole, D.L., Nobre, C.A., Hackler, J.L., Lawrence, K.T., & Chomentowski, W.H. (2000). Annual fluxes of carbon from deforestation and regrowth in the Brazilian Amazon. *Nature*, 403, 301-304.

Houghton, R.A. (2003). Revised estimates of the annual net flux of carbon to the atmosphere from changes in land use and land management 1850-2000. *Tellus*, 55B, 378-390.

Huete, A. R., Liu, H. Q., Batchily, K., & van Leeuwen, W. (1997). A comparison of vegetation indices over a global set of TM images for EOS-MODIS. *Remote Sensing of Environment*, 59 (3), 440-451.

Insituto Nacional de Pesquisas Espaciais (INPE) (2000). *Monitoring of the Brazilian Amazonian Forest by Satellite: 1998-1999.* Minsterio Da Ciencia e Tecnologia.

Iverson, L.R, E.A. Cook, and R.L. Graham (1989) A technique for extrapolating and validating forest cover across large regions: Calibrating AVHRR with TM data. *International Journal of Remote Sensing*, 10 (11), 1805-1812.

Iverson, L, Cook, E., & Graham, R. (1994). Regional forest cover estimation via remote sensing: the calibration center concept. *Landscape Ecology*, 9 (3), 159-174.

James, M. and S.N.V. Kalluri (1994). The Pathfinder AVHRR land data set: An improved coarse resolution data set for global monitoring. *International Journal of Remote Sensing*, 15, 3347-3364.

Jarvis, A.J., V.J. Stauch, K. Schulz and P.C. Young (2004). The seasonal temperature dependency of photosynthesis and respiration in two deciduous forests. *Global Change Biology*, 10, 939-950.

Jensen, J. (1996). *Introductory Digital Image Processing: A remote sensing perspective.* New Jersey: Prentice Hall, 236-238.

Jipp, P.H., D.J. Nepstad, D.K. Cassel, and C.R. Carvalho (1998). Deep soil moisture storage and transpiration in forests and pastures of seasonally-dry Amazonia. *Climatic Change*, 39, 395-412.

Kalacska, M.E.R, G.A. Sanchez-Azofeifa, J.C. Calva-Alvarado, B. Rivard, and M. Quesada (2005). Effects of season and successional stage on leaf area index and spectral vegetation indices in three Mesoamerican tropical dry forests. *Biotropica*, 37 (4), 486-496.

Kerdiles, H. & Grondona, M. (1995). NOAA-AVHRR NDVI decomposition and subpixel classification using linear mixing in the Argentinean Pampa. *International Journal of Remote Sensing*, 16 (7), 1303-1325.

Kimes, D.S., R.F. Nelson, W.A. Salas, and D.L. Skole (1999). Mapping secondary tropical forest and forest age from SPOT HRV data. *International Journal of Remote Sensing*, 20 (18), 3625-3640.

Laurance, W.F., M.A. Cochrane, S. Bergen, P.M. Fearnside, P. DeLamonica, C. Barber, S. D'Angelo, and T. Fernandes (2001). The future of the Brazilian Amazon. *Science*, 291, 438-439.

Li, X. & Strahler, A. H. (1992). Geometric-optical bidirectional reflectance modeling of the discrete-crown vegetation canopy: Effect of crown shape and mutual shadowing. *IEEE Transactions on Geoscience and Remote Sensing*, 30(2), 276-292.

Li, Y., P. Mausel, Y. Wu, E. Moran, and E. Brondizio (1994). Discriminating between advanced secondary succession and mature moist forest near Altamira, Brazil, using Landsat TM data. *Proceedings of the American Society for Photogrammetry and Remote Sensing*, 350-364.

Lloyd, J., and J.A. Taylor (1994). On the temperature dependence of soil respiration. *Functional Ecology*, 8, 315-323.

Loveland, T.R., Reed B.C., Brown J.F., Ohlen D.O., Zhu Z., Yang L. & Merchant J.W. (2000). Development of a global land cover characteristics database and IGBP DISCover from 1 km AVHRR data, *International Journal of Remote Sensing*, 21 (6-7), 1303-1330.

Lovell, J. & Graetz, R. (2002). Analysis of POLDER-ADEOS data for the Australian continent: the relationship between BRDF and vegetation structure. *International Journal of Remote Sensing*, 23 (14), 2767-2796.

Lu, D. (2006). The potential and challenge of remote sensing-based biomass estimation. *International Journal of Remote Sensing*, 7 (10), 1297-1328.

Lucas, R.M., M. Honzak, G.M. Foody, P.J. Curran, and C. Corves (1993). Characterizing tropical secondary forests using multi-temporal Landsat sensor imagery. *International Journal of Remote Sensing*, 14, 3061-3067.

Lucas, R.M., P.J. Curran, M. Honzak, G.M. Foody, I do Amaral, and S. Amaral (1996). Disturbance and recovery of tropical forests: balancing the carbon account. In *Amazonian deforestation and climate*, edited by J.H.C. Gash, C.A. Nobre, J.M. Roberts, and R.L. Victoria; Chichester: John Wiley & Sons.

Lucas, R.M., M. Honzak, P.J. Curran, G.M. Foody, R. Milne, T. Brown, and S. Amaral (2000). Mapping the regional extent of tropical forest regeneration stages in the Brazilian Legal Amazon using NOAA AVHRR data. *International Journal of Remote Sensing*, 21 (15), 2855-2881.

Lucas, R., Xiao, X., Hagen, S., & Frolking, S. (2002). Evaluating TERRA-1 MODIS data for discrimination of tropical secondary forest regeneration stages in the Brazilian Legal Amazon. *Geophysical Research Letters*, 29 (8), 42.

MacKay, D. (1994). Bayesian methods for backpropagation network. In *Models of Neural Networks, Vol. III*, Chapter 6, edited by E. Domany, J. van Hemmen, & K. Schulten, Springer-Verlag, New York.

Malingreau, J.P., F. Archard, C. Estreguil, H.J. Stibig, and G. D'Souza (1996). NOAA-AVHRR based tropical forest mapping for southeast Asia, validated and calibrated with higher spatial resolution imagery. In *Advances in the Use of NOAA AVHRR Data for Land Applications*,edited by G. D'Souza, A.S. Belward, and J.P. Malingreau, pp. 279-309, Kluwer, Dordrecht.

Mausel, P., Y. Wu, Y. Li, E.F. Moran, and E.S. Brondizio (1993). Spectral identification of successional stages following deforestation in the Amazon. *Geocarto International*, 4, 61-71.

Mayaux, P. and E.F. Lambin (1995). Estimation of tropical forest area from coarse spatial resolution data: a two-step correction function for proportional errors due to spatial aggregation. *Remote Sensing of Environment*, 53, 1-15.

Mesquita, R.C.G., K. Ickes, G. Ganade, and G.B. Williamson (2001). Alternative successional pathways in the Amazon Basin. *Journal of Ecology*, 89, 528-537.

Moorcroft, P.R., G.C. Hurtt, and S.W. Pacala (2001). Scaling rules for vegetation dynamics: A new terrestrial biosphere model for global change studies. *Ecological Monographs*, 74, 557-586.

Moran, E.F., E. Brondizio, P. Mausel, and Y. Wu (1994). Integrating Amazonian vegetation, land-use, and satellite data. *BioScience*, 44 (5), 329-338.

Myneni, R.B., F.G. Hall, P.J. Sellers, and A.L. Marshak (1995). The meaning of spectral vegetaqtion indices. *IEEE Transractions on Geoscience And Remote Sensing*, 33, 481-486.

Nelson, R. & Holben, B. (1986). Identifying deforestation in Brazil using multiresolution satellite data. *International Journal of Remote Sensing*, 7 (3), 429-448.

Nelson, R. (1989). Regression and ratio estimators to integrate AVHRR and MSS data. *Remote Sensing of Environment*, 30, 201-216.

Nelson, R.F., D.S. Kimes, W.A. Salas, and M. Routhier (2000). Secondary Forest Age and Tropical Forest Biomass Estimation Using TM. *BioScience*, 50 (5), 419-431.

Nepstad, D.C., C. Uhl, and S. Eas (1991). Recuperation of a degraded Amazonian landscape- forest recovery and agricultural restoration. *Ambio*, 20 (6), 248-255.

Nepstad, D.C., C.R. de Carvalho, E.A. Davidson, P.H. Jipp, P.A. Lefebvre, G. H. Negreiros, E.D. Da Silva, T.A. Stone, S.E. Trumbore, and S. Vieira (1994). The role of deep roots in the hydrological and carbon cycles of Amazonian forests and pastures. *Nature*, 372, 666-669.

Nepstad, D.C., A. Verissimo, A. Alencar, C. Nobre, E. Lima, P. Lefebvre, P. Schlesinger, C. Potter, P. Moutinho, E. Mendoza, M. Cochrane, and V. Brooks (1999). Large-scale impoverishment of Amazonian forests by logging and fire. *Nature*, 398, 505-508.

Oleson, K., Sarlin, S., Garrison, J., Smith, S., Privette, J., & Emery, W. (1995). Unmixing multiple land-cover type reflectances from coarse spatial resolution satellite data. *Remote Sensing of Environment*, 54, 98-112.

Papale D. and R. Valentini (2003). A new assessment of European forests carbon exchanges by eddy fluxes and artificial neural network spatialization. *Global Change Biology*, 9, 525-535.

Pfaff, A.S.P (1999). What drives deforestation in the Brazilian, Amazon? Evidence from satellite and socioeconomic data. *Journal of Environmental Economics and Management*, 37, 26-43.

Potter, C., Davidson, E., Nepstad, D., & de Carvalho, C. R. (2001). Ecosystem modeling and dynamic effects of deforestation on trace gas fluxes in Amazon tropical forests. *Forest Ecology and Management*, 152, 97-117.

Press, W.H., S.A. Teukolsky, W.T. Vetterling and B.P. Flannery (1993). Numerical recipes. In *Fortran 77: The art of scientific computing*, p. 992, Cambridge University Press, New York.

Prince S.D. and S.N Goward (1995). Global primary production: A remote sensing approach. *Journal of Biogeography*, 22, 815-835.

Privette, J. L., Emery, W. J., & Schimel, D. S. (1996). Inversion of a vegetation reflectance model with NOAA AVHRR data, *Remote Sens. Environ.*, 58, 187-200.

Puyou-Lascassies, P., G. Flouzat, M. Gay, and C. Vignolles (1994). Validation of the use of multiple liniear regression as a tool for unmixing coarse spatial resolution images, *Remote Sensing of Environment*, 49, 155-166.

Radtke, P., T.E. Burk, and P.V. Bolstad (2002). Bayesian melding of a forest ecosystem model with correlated inputs. *Forest Science*, 48, 701-711.

Richardson, A.D., and D.Y. Hollinger (2005). Statistical modeling of ecosystem respiration using eddy covariance data: Maximum likelihood parameter estimation and Monte Carlo simulation of model and parameter uncertainty applied to three different models. *Agriculture and Forest Meteorology*, 131, 191-208.

Ripple, W.J. (1994). Determining coniferous forest cover and forest fragmentation with NOAA-9 Advanced Very High Resolution Radiometer data. *Photogrammetric Engineering and Remote Sensing*, 60 (5), 533-540.

Robert, C.P., and G. Casella (1999). *Monte Carlo Statistical Methods*, Springer-Verlag, New York.

Roberts, D.A., I. Numata, K. Holmes, G. Batista, T. Krug, A. Monteiro, B. Powell, and O.A. Chadwick (2002). Large area mapping of land-cover change in Rondonia using multitemporal spectral mixture analysis and decision tree classifiers. *Journal of Geophysical Research*, 107, No. D20, doi:10.1029/2001JD000374.

Rojean, J., Leroy, M., & Deschamps, P. (1999). A bidirectional reflectance model of the Earth's surface for the correction of remote sensing data. *Journal of Geophysical Research*, 97 (D18), 20,455-20,468.

Salas, W.A. (2001). *Optical and Radar Remote Sensing of Land Use and Land Cover Change in the Tropics: An Assessment of Deforestation and Secondary Vegetation*. Ph.D. Dissertation, University of New Hampshire.

Saleska, S.R., S.D. Miller, D.M. Matross, M.L. Goulden, S.C. Wofsy, H.R. da Rocha, P.B. de Camargo, P. Crill, B.C. Daube, H.C. de Freitas, L. Hutyra, M. Keller, V. Kirchoff, M. Menton, J.W. Munger, E.H. Pyle, A.H. Rice, and H. Silva (2003). Carbon in Amazon forests: Unexpected seasonal fluxes and disturbance-induced losses. *Science*, 302, 1554-1557.

Schimel, D.S. (1995). Terrestrial ecosystems and the carbon cycle. *Global Change Biology*, 1, 77-91.

Skole, D. and C. Tucker (1993). Tropical Deforestation and Habitat Fragmentation in the Amazon: Satellite Data from 1978 to 1988. *Science*, 260, 1905-1910.

Skole, D.L, W.H. Chomentowski, W.A. Salas, and A.D. Nobre (1994). Physical and human dimensions of deforestation in Amazonia. *BioScience*, 44 (5), 314-322.

Steininger, M.K. (1996). Tropical secondary forest regrowth in the Amazon: age, area, and change estimation with Thematic Mapper data. *International Journal of Remote Sensing*, 17 (1), 9-27.

Steininger, M.K. (2000). Satellite estimation of tropical secondary forest above-ground biomass: data from Brazil and Bolivia. *International Journal of Remote Sensing*, 21 (6 & 7), 1139-1157.

Stone, T., Brown, I., & Woodwell, G. (1991). Estimation, by remote sensing, of deforestation in central Rondonia, Brazil. *Forest Ecology and Management*, 38, 291-304.

Tian, H., J.M. Melillo, D.W. Kicklighter, A.D. McGuire, J.V.K. Helfrich, B. Moore, C.J. Vorosmarty (1998). Effect of interannual climate variablity on carbon storage in Amazonian ecosystems. *Nature*, 396, 664-667.

Townshend, J.R.G., V. Bell, A. Desch, C. Havlicek, C.O. Justice, W.E. Lawrence, D. Skole, W. Chomentowski, and W.A. Salas (1995). The NASA Landsat Pathfinder Humid Tropical Deforestation Project, Land Satellite Information in the Next Decade. *American Society of Photogrammetry and Remote Sensing*, pp. IV76-IV87, Tyson's Corner, Virginia.

Townshend, J., Huang, C., Kalluri, S., Defries, R., Liang, S., & Yang, K. (2000). Beware of per-pixel characterization of land cover. *International Journal of Remote Sensing*, 21 (4), 839-843.

Tucker, C.J., J.R.G. Townshend, and T.E. Goff (1985). African land cover characterization using satellite data. *Science*, 227, 369-375.

Tucker, C.J. and J.R.G. Townshend (2000). Strategies for monitoring tropical deforestation using satellite data. *International Journal of Remote Sensing*, 21 (6), 1461-1471.

Turner, B.L, W.B. Meyer, and D.L. Skole (1994). Global land-use/land-cover change: towards an integrated study. *Ambio*, 23 (1), 91-95.

Uhl, C. (1987). Factors controlling succession following slash-and-burn agriculture in Amazonia. *Journal of Ecology*, 75, 377-407.

Uhl, C., R. Bushbacher, and E.A.S. Serro (1988). Abandonded pasture in eastern Amazonia. I. Patterns of plant succession. *Journal of Ecology*, 76, 663-681.

USGS EROS Data Center (2002). *MODIS Reprojection Tool User's Manual*. Department of Mathematics and Computer Science, South Dakota School of Mines and Technology (http://edcdaac.usgs.gov/tools/modis/info/MRT_Users_Manual.pdf).

Vermote, E.F., D. Tanre, J.L. Deuze, M. Herman, and J. Morcrette (1997). Second Simulation of the Satellite Signal in the Solar Spectrum, 6S: An overview. *IEEE Transactions on Geoscience and Remote Sensing*, 35 (3), 675-686.

Walker, G.K., Sud, Y.C., & Atlas, R. (1995). Impact of the ongoing Amazonian deforestation on local precipitation- A GCM simulation study. *Bulletin of the American Meteorological Society*, 76 (3), 346-361.

Wanner, W., Strahler, A., Hu, B., Lewis, P., Muller, J.-P., Li, X., Barker-Schaaf, C., & Barnsley, M. (1997). Global retrieval of BRDF and albedo over land from EOS MODIS and MISR data: Theory and algorithm. *Journal of Geophysical Research*, 102(D14), 17143-17161.

Willmott, C. J., and S. R. Webber (2003). LBA Regional Climate Data, 0.5-Degree Grid, 1960-1990. Data set. Available on-line [http://www.daac.ornl.gov] from Oak Ridge National Laboratory Distributed Active Archive Center, Oak Ridge, Tennessee, U.S.A.

Wofsy, S. C., M. L. Goulden, J. W. Munger, S. M. Fan, P. S. Bakwin, B. C. Daube, S. L. Bassow, F. A. Bazzaz (1993). Net exchange of CO_2 in a midlatitude forest. *Science*, 260, 5112-1314.

Woodwell, G.M., R.A. Houghton, T.A. Stone, R.F. Nelson, and W. Kovalick (1987). Deforestation in the Tropics: New measurements in the Amazon Basin using Landsat and NOAA Advanced Very High Resolution Radiometer Imagery. *Journal of Geophysical Research*, 92 (D2), 2157-2163.

Xiao, X., D.Y. Hollinger, J. Aber, M. Goltz, E.A. Davidson, Q. Zhang, and B. Moore (2004). Satellite-based modeling of gross primary production in an evergreen needleleaf forest. *Remote Sensing of Environment*, 89, 519-534.

Xiao, X., S. Hagen, Q. Zhang, M. Keller, and B. Moore (2006). Detecting leaf phenology of seasonally moist tropical forests in South America with multi-temporal MODIS images. *Remote Sensing of Environment*, 103, 465-473.

Zhu, Z. & Evans, D. (1994). U.S. forest types and predicted percent forest cover from AVHRR data. *Photogrammetric Engineering & Remote Sensing*, 60 (5), 525-531.